

Nanomechanical Properties of Electrodeposited Li and Fabrication of 3D Architected Cathodes for Li-Based Batteries

Thesis by
Michael A. Citrin

In Partial Fulfillment of the Requirements for the
Degree of
Doctor of Philosophy

The logo for the California Institute of Technology (Caltech), featuring the word "Caltech" in a bold, orange, sans-serif font.

CALIFORNIA INSTITUTE OF TECHNOLOGY
Pasadena, California

2020
Defended September 19th, 2019

© 2020

Michael A. Citrin

ORCID: 0000-0001-8183-5437

All rights reserved except where otherwise noted

ACKNOWLEDGEMENTS

First and foremost, I would like to thank my advisor, Julia. I admire your never-ending enthusiasm and optimism that has helped make the Greer lab a fun and inspiring group to be in. I am grateful for the opportunities you have given me to present at conferences, engage in fruitful collaborations, and meet and interact with exciting people in the community. Thank you so much for all the support throughout grad school and for pushing me to become a better scientist and communicator.

I appreciate all the contributions from Joel and Prof. Dave Srolovitz and their helpful discussions and suggestions. I would also like to thank Simon for being so generous and enthusiastic to collaborate with. I wish to thank Matt for all the help in the KNI and for the advice on how to become a better microscopist and scientist. I would like to thank Shrawan Mageswaran for the assistance and flexibility with the cryo-FIB and Wenpei Gao, Andrey Malyyutin, Peter Tieu, and Mingjie Xiu for all the help running TEM experiments. I am very grateful for Christy, Jennifer, and Angie for all their support and advice, both practical and personal.

Thank you very much to Heng for your mentorship during grad school, for all your valuable guidance, and for working with me on the battery projects. I would also like to thank Xiaoxing, Dylan, and Chen for their advice and training, and for always being willing to help out and answer my questions. I'm extremely grateful for Max and Daryl for all their supportive discussions and advice and for making grad school much more enjoyable. I am very thankful for Ottman, Carlos, and Jane for their invaluable help, training, and discussions about mechanical experiments. I would also like to thank Neal, Ryan, Kai, and Viki, in addition to the rest of the Greer group members, for all the wonderful discussions about science and life.

I am thankful for everyone in my materials science year, especially for turning the grind of first year into a fun and valuable experience. I would like to thank the Fremont house — Kyle, Austin, Alistair, Dan, and Joe — for being such awesome roommates and making our house feel like such an enjoyable home to live in. Thank you to the many other friends I have made and people I have met during my time at Caltech whom I have benefited so much from.

I am very grateful to my family for giving so much support during my grad school experience on the other coast. Thank you to my parents — without your encouragement and the comfort you provided me, my success would not have been possible.

Last but not least, thank you to Shanee, who has provided me with unconditional support throughout grad school. I am deeply grateful for your willingness to listen and help out as much as you can. Thank you to everybody who made my time at Caltech such a pleasure and an unforgettable experience.

ABSTRACT

Advancements in the active materials of Li-based batteries provide a promising route to significantly improve electrochemical performance. Li metal has a 10x increase in gravimetric capacity compared to conventional graphite anodes and can be utilized with a solid electrolyte. However, current solid-state Li metal anode batteries cannot reliably cycle large amounts of Li due to chemical and mechanical degradation at the solid electrolyte / Li interface. One key factor in the failure of solid electrolytes is the dearth of mechanical data on Li at the relevant length scales and microstructures to solid-state batteries. The initial stages of Li formation at the solid electrolyte / Li interface also require further exploration to help improve the performance of solid-state Li batteries.

In the first part of the thesis, we will discuss the methods used to investigate Li electrodeposited *in-situ* in a scanning electron microscope (SEM) chamber from a thin film solid-state battery. We probed the formation of this Li and found preferential growth at the domain boundaries of the surface of the cell, corroborated by electrochemical simulations. Cryogenic electron microscopy was determined to be the optimal method for examining the microstructure of Li and was utilized to reveal the single crystalline microstructure of Li pillars. Uniaxial compression experiments were performed on single crystalline Li pillars that grew from these batteries. We found that Li pillars with diameters of 360-759 nm first deformed elastically, then yielded and flowed plastically, with an average yield stress of 16.0 ± 6.82 MPa, 24x stronger than bulk polycrystalline Li. The mechanical results are discussed in the framework of dislocation starvation and nucleation, in addition to thermally activated deformation processes.

Next generation battery systems may also utilize 3D electrodes to allow for both high energy (large mass loading) and power densities (small diffusion lengths). The last section of the thesis investigates the fabrication of 3D architected LiCoO_2 structures and their performance as Li-ion battery cathodes. Using a novel hydrogel photoresin with relevant salt contents, the structures were fabricated using digital light processing and calcination. The electrochemical performance of the architected cathodes was examined and the electrodes exhibited a relatively high areal capacity up to ~ 8 mAh/cm² and a capacity retention of 82% after 100 cycles.

PUBLISHED CONTENT AND CONTRIBUTIONS

1. Citrin, M. A., Yang, H., Nieh, S. K., Berry, J., Gao, W., Pan, X., Srolovitz, D. J., & Greer, J. R. From Ion-to-Atom-to-Dendrite: Formation and Nanomechanical Behavior of Electrodeposited Lithium. (*In preparation*).

M.A.C. participated in the conception of the project and the design of experiments, performed the mechanical experiments, analyzed the mechanical data and developed potential strengthening mechanisms, fabricated *in-situ* TEM and cryo-EM samples, analyzed TEM data, assisted with the development of the *in-situ* experimental set-up, assisted with Li formation experiments and analysis of formation data, and wrote the manuscript with input from other authors.

2. Yee, D. W.*, Citrin, M. A.*, Taylor, Z., Tovmasyan, V. & Greer, J. R. Additive Manufacturing of Complex Metal Oxides for 3D Li Ion Battery Cathodes. (*In preparation*).

M.A.C. participated in the conception of the project and the design of experiments, assisted with calcination and XRD, performed SEM and FIB analysis, performed morphological analysis, designed the testing cell stack and conductive adhesive, assembled the cells, performed the electrochemical characterization, and participated in the writing of the manuscript.

TABLE OF CONTENTS

Acknowledgements	iii
Abstract	v
Published Content and Contributions	vi
Table of Contents	vii
List of Illustrations	ix
List of Tables	xi
Chapter I: Introduction	1
1.1 Brief History of Li-ion Batteries	1
1.2 Li-ion Battery Operation	2
1.3 Li Metal Solid-State Batteries	3
1.4 Small-Scale Plasticity	4
1.5 Thesis Overview	6
Chapter II: Electrochemical and Mechanical Experiments Performed in the SEM	7
2.1 Solid-State Li Metal Batteries	7
2.2 Thin Film Solid-State Battery for <i>In-situ</i> SEM Experiments	9
2.3 <i>In-situ</i> Uniaxial Compression	13
Chapter III: Formation of Li in Li-free Solid-State Batteries	17
3.1 Introduction-Li-free Cells	17
3.2 Li Electrodeposition	18
3.3 Preferential Li Formation at Domain Boundaries	18
3.4 Li Morphologies	23
3.5 Conclusions	24
Chapter IV: Microstructure of Li Electrodeposited from a Solid Electrolyte	25
4.1 Challenges Performing TEM Analysis on Li	25
4.2 <i>In-situ</i> TEM	26
4.3 Cryo-EM	29
4.4 Microstructure of Electrodeposited Li via Cryo-EM	32
4.5 Summary and Conclusions	35
Chapter V: Mechanical Properties of Li Electrodeposited through a Solid Electrolyte	36
5.1 Young's Modulus and Strength	36
5.2 Mechanical Response in Context	40
5.3 Possible Strengthening Mechanisms	49
5.4 Implications for Solid-State Batteries	53
5.5 Conclusions	54
Chapter VI: 3D Architected Li-ion Cathodes	55
6.1 Three-Dimensional Batteries	55
6.2 Fabrication of 3D Architected LCO Electrodes	57

6.3 Materials Characterization of LCO Structures	64
6.4 Electrochemical Performance of 3D LCO Electrodes	67
6.5 Conclusions	75
Chapter VII: Thesis Summary and Outlook	77
References	80

LIST OF ILLUSTRATIONS

<i>Number</i>	<i>Page</i>
1.1 Li ion battery schematic	3
1.2 The size effect of strength	6
2.1 Thin film solid-state battery cross-section	10
2.2 Electrochemical impedance spectroscopy of thin films cells	11
2.3 SEM image distortion from Kapton tape	13
2.4 Schematic of <i>in-situ</i> electrical and nanomechanical instrumentation in an SEM	14
2.5 Schematic of the components of the nanoindenter head	14
2.6 Strain rate from constant loading rate	15
3.1 Li formation during charging in the SEM and Li morphologies	19
3.2 Images of Li formation during charging in an SEM	20
3.3 Li morphologies at different surface curvature	21
3.4 Electrochemical simulations of electrolyte potential, current density, and Li ⁺ concentration	22
4.1 Sample fabrication for <i>in-situ</i> charging in a TEM	28
4.2 Electrical response of <i>in-situ</i> charging in a TEM	29
4.3 Sample fabrication for <i>in-situ</i> charging in a TEM at a 90 ° orientation	30
4.4 Cryo-FIB sample transfer procedure to cryo-EM	31
4.5 Transfer method of Li into the cryo-EM	33
4.6 Cryo-EM of Li fibers grown through a solid electrolyte	34
4.7 Kinked Li fibers via cryo-EM	34
5.1 Uniaxial compression experiment and mechanical response	37
5.2 Constant load rate vs. constant displacement rate	38
5.3 Strain bursts	39
5.4 Mechanical response with strain excursions	42
5.5 Mechanical response of bent fiber	43
5.6 Effect of cross-sectional geometry	46
5.7 Parameter space for strength vs. size for Li of various form factors, dimensions, microstructures, and fabrication techniques	48
6.1 DLP fabrication process using photopolymer complex synthesis	58
6.2 Thermogravimetric analysis of the Li ⁺ and Co ²⁺ containing resin	59

6.3	Structural transformation after calcination	60
6.4	Morphology of LCO lattices	61
6.5	Failure of LCO lattices	63
6.6	X-ray diffraction and energy-dispersive x-ray spectroscopy of LCO structures	65
6.7	Cyclic voltammetry of LCO structures	67
6.8	Coin cell stack to test LCO lattices	69
6.9	Electrochemical performance of 3D LCO structures	70
6.10	Rate capability and performance of slurry vs. lattice	72
6.11	Areal capacity of LCO lattices	73
6.12	X-ray diffraction, energy-dispersive x-ray spectroscopy, and electro- chemical cycling of NCA structures	75

LIST OF TABLES

<i>Number</i>		<i>Page</i>
5.1	Mechanical data for all pillar samples	45
6.1	Atomic percentages of LCO structures taken from EDS spectra . . .	66

Chapter 1

INTRODUCTION

The lithium-ion battery (LIB) has permeated modern society and is the rechargeable energy storage of choice for a variety of applications. These uses span a wide range of energy magnitudes, from μWh for microelectronics, mWh to Wh for implantable devices, Wh for mobile devices, laptops, and drones, and kWh for electric vehicles (EVs), to MWh for grid storage. Driven by a large decrease in price per kWh , the production and utilization of LIBs has increased significantly this decade, and that trend is expected to continue in the upcoming decades [1]. LIBs provide key opportunities to combat the detrimental effects of climate change by replacing the internal combustion engine in EVs and by supporting renewable energy sources with on-grid energy storage. Current LIB materials cannot provide energy densities high enough to reach the Department of Energy's EV goals of 235 Wh kg^{-1} and 500 Wh L^{-1} at the pack level, with current packs providing $\sim 150 \text{ Wh kg}^{-1}$ and $\sim 250 \text{ Wh L}^{-1}$ [2]. This $\sim 50\%$ increase in gravimetric energy density, for instance, could improve the range of the Tesla Model 3 to over 500 miles, a range that would likely increase consumer demand [3]. Motivated by the need to increase the energy density of LIBs for these reasons, a large amount of research has been devoted to understanding and developing new battery chemistries that could provide higher energy densities than current LIB materials. The goal of this thesis is to investigate critical mechanisms, material properties, and battery architectures that may help lead to the successful implementation of high energy density Li-based batteries.

1.1 Brief History of Li-ion Batteries

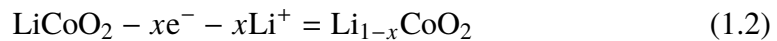
Before the invention of the LIB, common battery chemistries included primary (non-rechargeable) lead-acid and nickel-cadmium, in addition to secondary (rechargeable) nickel-metal hydride and alkaline, which all suffer from low energy density, specific capacity, and voltage [4, 5]. The first significant LIB discovery by Wittingham in 1978 was the intercalation of Li ions, where ions are reversibly inserted and removed from the crystal lattice of a material, using Li transition metal sulfide cathodes [6]. These early Li batteries used Li metal as the anode but were afflicted by low cell voltage and safety issues from the very reactive Li metal [4]. In 1980, the Goodenough lab discovered an improved Li intercalation cathode, LiCoO_2 (LCO),

which provided stable, reversible cycling at high voltage (> 4 V) [7] and is still the most common cathode material in LIBs [5]. On the anode side, developments into various forms of carbon allowed for more reversible, safer batteries [8, 9]. This led to the first commercial LIB, developed by Sony in 1991, that was composed of a graphite anode and LCO cathode [4].

1.2 Li-ion Battery Operation

Like all batteries, a LIB requires two electrodes, an anode and cathode, separated by an electrically insulating and ionically conductive electrolyte. Energy is derived when there is a difference in chemical potential between the two electrodes. At each electrode, a half reaction defines a reduction potential depending on how easy the material gains (reduction) or loses (oxidation) electrons, and the difference in these potentials determines the voltage of the cell. Graphite is the most common LIB anode with a voltage of ~ 0 to 0.5 V vs. Li / Li^+ [10]. Cathode materials have more variety, with common materials LCO, $\text{LiNi}_{0.8}\text{Co}_{0.15}\text{Al}_{0.05}\text{O}_2$ (NCA), $\text{LiNi}_{0.33}\text{Mn}_{0.33}\text{Co}_{0.33}\text{O}_2$ (NMC), and LiFePO_4 (LFP) typically providing voltages between 3 and 4.5 V vs. Li / Li^+ [11]. Because water decomposes at the operation voltages of LIB cells, the electrolytes are composed of organic solvents, commonly a mixture of ethylene carbonate and diethyl carbonate (EC:DEC), with a dissolved Li salt, such as LiPF_6 [12]; a polypropylene or polyethylene porous separator is wet with the electrolyte during cell assembly [13].

Figure 1.1 shows a schematic of the materials in and operation of a LIB. The half reactions during charge for a graphite anode and LCO cathode are shown in equations 1.1 and 1.2, respectively, with a nominal voltage ~ 3.7 V [14].



During charge, Li ions are driven by an external energy source from the LCO through the electrolyte and intercalate into the graphene sheets of the anode. On discharge, the reverse process occurs and electrons are driven through an external circuit to the cathode to provide power as Li ions intercalate between the transition metal oxide layers of the crystal lattice, which act a host for Li ions [14]. Electrodes are typically composed of powders of the active material, a conductive additive, and a binder, all cast as a slurry onto a metal current collector foil.

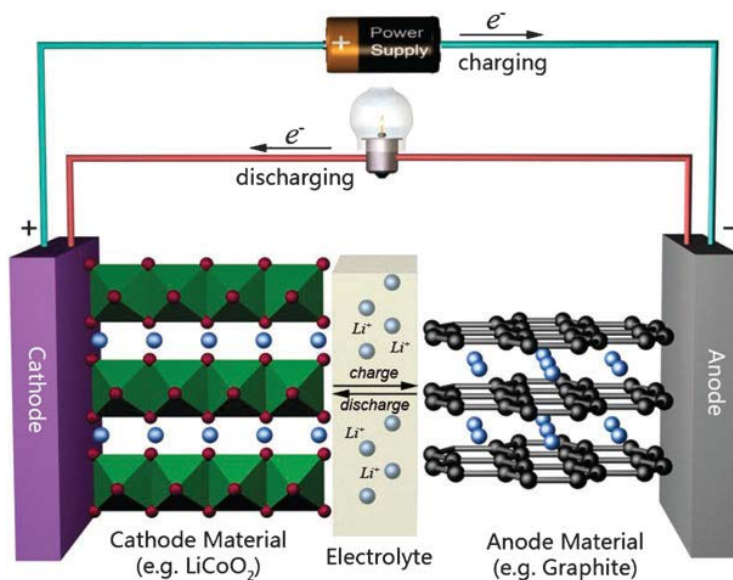


Figure 1.1: Schematic of the components of a Li-ion battery adapted from Reference [15].

1.3 Li Metal Solid-State Batteries

While the previous section discussed the modern LIB, the materials used in these batteries are currently approaching their energy density limits [14]. The usable capacity of graphite and typical transition metal oxide cathodes is $\sim 300\text{-}350$ mAh/g and $\sim 150\text{-}200$ mAh/g, respectively [16]. To improve energy density, researchers are continually developing new insights and discoveries to help implement high energy materials into LIBs. For example, disordered rocksalt [17] and Li-excess layered [18] cathode materials can reach capacities >250 mAh/g and voltages >4.2 V. Liquid electrolytes that are stable at high voltages >4.5 V, such as those that utilize ionic liquids [19] and sulfones [20], can potentially improve the energy density and safety of LIBs. Si anodes have been extensively studied for their low cost and high theoretical gravimetric (or specific) capacity of 4200 mAh/g [21], and have begun commercialization [22, 23].

However, the "holy grail" of LIB materials is Li metal itself. It has the largest specific capacity for an anode of 3860 mAh/g¹ and the lowest standard reduction potential of -3.040 V vs. the standard hydrogen electrode [24], allowing for potentially the largest gravimetric energy density of any monovalent ion-producing electrode.

¹The theoretical capacity of Li is lower than that of Si because they are calculated differently. For Si, it is calculated as the amount of charge of Li that lithiates an initial mass of Si to form $\text{Li}_{4.4}\text{Si}$. The capacity of Li is just based on the charge of Li; if it were calculated the same way as Si, its capacity would be infinite. Practically, the gravimetric capacity of Li is larger than that of Si.

Li was actually the original anode studied for LIBs before carbonaceous anodes were developed, and research interest in this material has greatly expanded recently [25]. The principle issue preventing the implementation of Li metal in rechargeable batteries is the formation of Li dendrites upon cycling; these branching, tree-like structures can lead to short circuiting (safety hazard and cell death) and to “dead Li”, which drastically reduces battery cycle life [24, 26, 27]. Dendrite formation arises from various factors, including the reactivity of Li with the electrolyte creating an inhomogenous solid electrolyte interphase (SEI) layer, mechanically weak separators, and unstable ion transport at the dendrite surface [28].

Many different approaches that aim to inhibit and suppress dendrite formation in liquid electrolytes have been put forth, including but not limited to: (1) electrolyte additives for enhanced SEI properties [29], (2) electrode engineering for uniform current distribution [30], (3) a self-healing electrostatic mechanism [31], and (4) pulse electrodeposition [32]. One of the most promising routes to suppress Li dendrite formation involves replacing the conventional liquid electrolyte-in-porous-separator with a solid polymer or ceramic electrolyte. A solid electrolyte (SE) can mechanically suppress dendrites by plastically flowing Li, flattening the electrode and preventing it from crossing the electrolyte [33, 34]. SEs also provide enhanced safety, as they replace the common flammable liquid organic electrolyte [35]. Current SEs struggle to perform their crucial and difficult role with a variety of issues; the electrical conductivity and microstructure of the electrolyte [36, 37], chemical reactions at the interface [38], fracture toughness of the SE [39], and mechanical properties of Li [33, 40] all contribute to the performance and failure of SEs. There is a great need to further understand the mechanisms and degradation at the Li / SE interface.

1.4 Small-Scale Plasticity

Li, a body-centered (bcc) metal, often forms with submicron dimensions in cracks or grain boundaries of SEs [37] and at the beginning of electroplating in liquid electrolytes [41]. The modulus of a metal is determined by its interatomic bond strength, and so is generally only dependent on the metal’s constitutive elements, porosity, and orientation. In contrast, post-yield deformation and mechanical properties of metals are a strong function of microstructure: crystal structure, grain size, dislocation density, porosity, impurity concentration, etc. The strength of metals is tied to the motion of dislocations, line defects that disrupt crystalline order and move under a shear stress, resulting in a microstructural sensitive property. For example,

the well-known Hall-Petch strengthening relates the yield strength of a metal, σ_y , to its grain size, D_{GB} , as:

$$\sigma_y = \sigma_0 + k_1 D_{GB}^{-1/2} \quad (1.3)$$

Where σ_y is the yield strength, σ_0 is approximately the yield stress of a coarse grained, well annealed crystal, and k_1 is a constant [42]. Smaller grains, and thus more grain boundaries, provide obstacles for dislocation motion, increasing strength.

At length scales $< \sim 10 \mu\text{m}$, sample size and microstructure of metals substantially influence their strengths. For example, metallic samples carved out of bulk single crystals become stronger with size reduction in a power law fashion [43], while those grown as individual micro-structures via directional solidification can attain close-to-theoretical strengths that do not vary with size [44]. Nanocrystalline metals become weaker with smaller sample size [45, 46] and the deformation of bi-crystalline metals depends on the relative orientation of the grain boundary plane and loading axis [47, 48]. Experiments on single crystalline metallic samples reveal a ubiquitous “smaller is stronger” power law dependence of strength on size. Figure 1.2(a) demonstrates the typical stress-strain curves for these samples (Figure 1.2(b,c)). The samples’ yield and/or flow stress scales with pillar diameter, D , as:

$$\frac{\tau_{Res}}{\mu} = A \left(\frac{D}{b} \right)^m \quad (1.4)$$

In this framework, τ_{Res} represents the shear stress that corresponds to the uniaxially applied normal stress resolved onto a particular crystallographic slip system ($\{111\}/\langle 110 \rangle$ for face-centered cubic (fcc) crystals), μ is the shear modulus on the same crystallographic planes, D is the pillar diameter, b is the magnitude of the Burgers vector, A is a scaling constant, and m is the power law exponent. m has been found to be universal, ~ -0.6 , for nearly all fcc metals (Figure 1.2(d)) [49–51] and varies from -0.32 to -0.93 for bcc metals [40, 52–54]. The slope is lower for some bcc metals mainly due to the higher Peierls stress in bcc crystals, the stress needed to move a dislocation on its glide plane [53]. This strengthening is often thought to arise from dislocation annihilation at the free surfaces of the small volume of material, leading to a state known as dislocation starvation, where dislocations need to be nucleated at ever higher stresses during deformation [43, 55]. Over an order of magnitude strengthening can emerge from the smaller-is-stronger size effect (Figure 1.2).

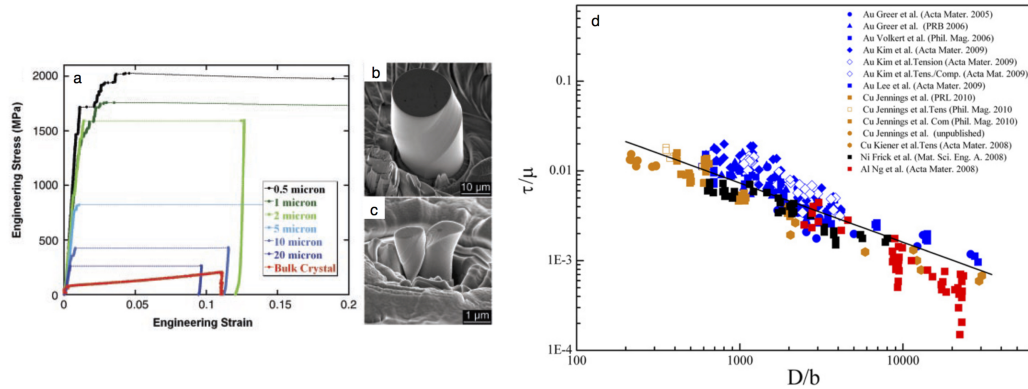


Figure 1.2: (a) Stress-strain curves for Ni_3Al - Ta micropillars of different diameters. Micropillars before (b) and after (c) deformation. (a-c) adapted from Reference [49]. (d) Scaling law for different fcc crystals, adapted from Reference [43].

1.5 Thesis Overview

The objective of this thesis is to explore fundamental mechanisms and material properties of Li electrodeposited in a solid-state battery. Chapter 2 will describe the experimental instrumentation and procedures used to charge thin film solid-state batteries and perform nanomechanical experiments *in-situ* in a scanning electron microscope (SEM) chamber. Chapter 3 will investigate the initial stages of the formation of Li when these batteries are charged. Chapter 4 will probe the microstructure of this Li and discuss the challenges to perform microstructural analysis on Li metal. Chapter 5 will examine the strength and stiffness of Li electrodeposited from the solid-state batteries and discuss the results in the framework of small-scale plasticity and their relevance to solid-state batteries. Chapter 6 will introduce a novel cathode 3D architecture that could utilize the advantages of solid-state Li batteries. Finally, the last chapter will provide a summary of the thesis and an outlook of the field looking forward.

*Chapter 2***ELECTROCHEMICAL AND MECHANICAL EXPERIMENTS
PERFORMED IN THE SEM**

Adapted from

1. Citrin, M. A., Yang, H., Nieh, S. K., Berry, J., Gao, W., Pan, X., Srolovitz, D. J., & Greer, J. R. From Ion-to-Atom-to-Dendrite: Formation and Nanomechanical Behavior of Electrodeposited Lithium. (*In preparation*).

This chapter introduces the need for characterization of the mechanical properties of Li metal at the dimensions and microstructures relevant to solid-state batteries, in addition to further understand the initial stages of Li growth. The *in-situ* experimental set-up to probe the formation and mechanical properties of Li in an SEM chamber is illustrated in the following sections. The techniques to charge the cell and perform mechanical experiments are also discussed in this chapter.

2.1 Solid-State Li Metal Batteries

One of the most promising methods to suppress dendrite formation involves replacing the conventional liquid electrolyte-in-porous-separator with a solid polymer or ceramic electrolyte. The theoretical framework for this approach was initially developed by Monroe and Newman [33], who incorporated elasticity into the Butler-Volmer equation and suggested that dendrite formation may be suppressed when the shear modulus of a polymer electrolyte is at least twice that of Li (3.4 GPa). Using a similar approach, Ferrese and Newman [34] showed that a polymer separator with a shear modulus of ~ 8 GPa (twice that of Li) results in a ~ 1 MPa stress in the anode after electrodeposition; this exceeds the reported yield stress of Li (0.655 MPa [56]) and flattens the electrode. Ahmad and Viswanathan [57] extended this approach to ceramic electrolytes by varying the Li atom/Li ion molar volume ratio in the electrolyte leading to Li dendrite suppression when the ceramic electrolyte shear modulus was less than ~ 0.7 that of Li. Existing solid electrolytes (SEs) do not meet these moduli requirements: polymer electrolytes typically have moduli below 150 MPa [58] and ceramic ones above 7 GPa [59].

Most SEs fail via catastrophic failure or short circuiting when cycled above a critical current density, regardless of their moduli [37, 38, 60]. For example, in garnet-type electrolytes (i.e. polycrystalline $\text{Li}_7\text{La}_3\text{Zr}_2\text{O}_{12}$ (LLZO): shear modulus ~ 60 GPa), Li penetrates the electrolyte grain boundaries in a web-like structure during cycling [61, 62]. Porz et al. [37] demonstrated that above a critical current density, metallic lithium forms at defects (e.g., polishing features and voids) even in single crystalline garnet electrolytes, which serve as stress concentrations/crack initiation sites during cycling; Li filaments formed in these cracks had diameters of around 300 nm and can short circuit the cell. Possible reasons for this severe discrepancy between theoretical predictions for dendrite suppression and the common observation of dendrite formation (under conditions where the theory suggests suppression) is the neglect of other important factors [37, 38, 63]; e.g., the electrical conduction within the electrolyte [36], electrolyte microstructure [37], interfacial reactions [38], plasticity within the Li [40, 64–71], and fracture toughness of the SE [39]. Electrolyte and cell failure are influenced by microstructure, cycling conditions, and processing defects; hence preventing failure requires a more sophisticated understanding of the Li / SE interaction than incorporated into the isotropic continuum-based Monroe and Newman criterion [33].

This brief overview highlights the importance of the combined effects of microstructure (e.g., single- vs. poly-crystal) and mechanical properties (yield strength, elastic anisotropy, and ductility) of Li at the nano- and micro-scales on the electro-chemo-mechanical processes that operate during Li cycling with SEs. Such understanding is critical for developing physically-based strategies for preventing dendrite formation and electrolyte failure. Unfortunately, the literature on mechanical properties of metallic Li is sparse (virtually non-existent for the electrodeposited metal and samples of small dimensions relevant to solid-state batteries [72]). Further, existing studies report widely varying results, e.g, yield stresses for bulk polycrystals (grain sizes either unknown or >1 mm) were reported to be 0.6-0.81 MPa under quasi-static tension [56, 66, 70] and 0.56-0.81 MPa in compression [66, 71], 105 MPa for compression of micron-size single crystals carved from re-melted foils using a Focused Ion Beam, FIB [40], and ~ 13 -30 MPa for sub-micron-thick thermally evaporated thin films based on nanoindentation studies [64, 73] (indentation hardness was converted to yield strength as 1/3 of the hardness via the Tabor relationship [74]). Tensile experiments on bulk polycrystalline Li (grain size = 150 μm) suggested room temperature deformation occurred via creep (flow stress <1 MPa at strain rates $< 10^{-2} \text{ s}^{-1}$) [69]. The range of reported macro-sized polycrystalline Li compressive

strengths (0.56-0.81 MPa) may be attributed to differences in microstructure, experimental strain rates, and test temperatures. Deformation characteristics of small-scale Li samples also exhibit considerable variability: nanoindentation of 750 μm -thick polycrystalline Li foils suggested viscoplastic / power law creep deformation and negligible elastic response [67, 68]. On the other hand, all of the compression experiments on single crystalline micro-pillars show elastic behavior up to strains of 2-3%, followed by yield and significant plastic flow without hardening for strains up to $\sim 20\%$ [40].

On the sub-micron to micron scales (typical length scales of electrodeposited Li) [15, 72], sample size and microstructure of metals substantially influence strengths, which may help explain why electrochemically-formed Li filaments can penetrate submicron electrolyte cracks [37, 61, 62]. These effects arise from dislocation interactions with free surfaces in micron- and sub-micron-size metals and thermally activated dislocation processes (e.g., climb and kink-pair formation) [52]. The combination of size-, rate-, and microstructure-dependent strength of small-scale metals, and the substantial reported differences in the mechanical properties of Li demand accurate measurement of the mechanical properties of lithium as a function of its microstructural characteristics (and their connection to formation and processing conditions), at length scales relevant to electrochemical deposition.

2.2 Thin Film Solid-State Battery for *In-situ* SEM Experiments

At Oak Ridge National Lab (ORNL), Bates et al. [75] reported the first successful demonstration of a SE with Li metal anodes in rechargeable thin film batteries using a vapor-deposited amorphous lithium phosphorus oxynitride (LiPON) SE. ORNL has pioneered LiPON batteries from the work of John Bates, Nancy Dudney, and coworkers. In subsequent work by groups at ORNL, [75–79], these batteries were cycled up to ten thousand times with little capacity fade but required an excess of Li of at least 500 nm to achieve extended cycling, reducing the energy density of the battery and adding to production costs. Currently, LiPON is the most mature solid electrolyte, being deployed commercially in small consumer and medical devices [77].

We used Li-free thin film solid-state batteries in their as-fabricated state (no Li metal) fabricated by Front Edge Technology [80]. "Li-free" in this context indicates that all of the Li was initially stored in the as-deposited cathode. Figure 2.1 shows a schematic and SEM images of the batteries in their as-fabricated state used in

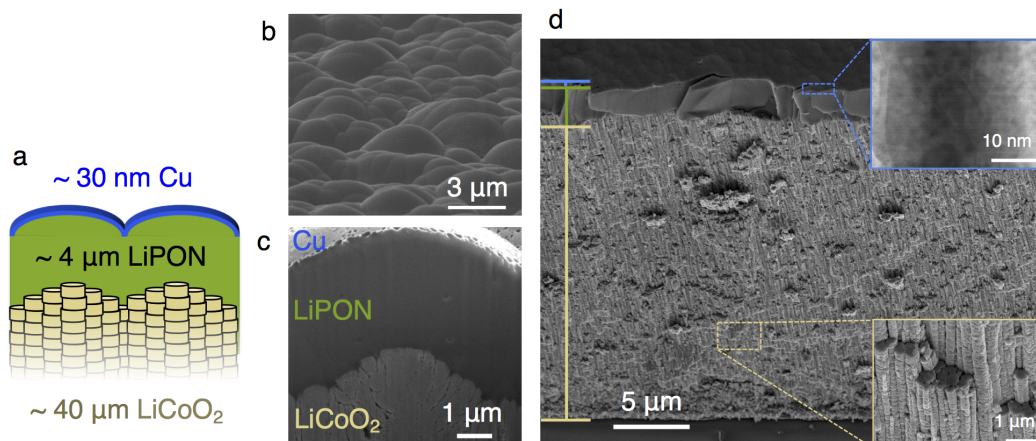


Figure 2.1: Morphology and cross-section of a thin film Li-free battery. (a) Schematic of the cell cross-section. (b) SEM image of the top surface taken at 10° from the surface normal shows the nodular morphology of the cell; bundle domains have diameters between 1-10 μm . (c) SEM cross-section of a single domain (note that the LCO, LiPON and Cu are all conformal). (d) SEM images of the cell cross-section with insets of a TEM image of section of the Cu layer and a higher resolution SEM image of a section of the columnar LCO morphology.

this study. They consist of a stack of a ~ 40 μm -thick LCO cathode, a 4 μm -thick LiPON solid electrolyte, and a 30 nm-thick Cu current collector — all deposited by magnetron sputtering [81, 82]. The LCO cathode has a columnar grain structure, with 100-500 nm diameter crystallites (Figure 2.1(a, b, d)), that bundle together into domains that coalesce into increasingly larger bundles/domains with some height differences. The morphology of the battery layers above the cathode follow the overall topography of these LCO bundles, which create a nodular top surface topography (Figure 2.1(c)), with peak-to-valley heights of ~ 3 μm . The Li-free cell design with no overlayer allows the direct observation of and access to Li as it forms when it grows out of the top of the cell into the vacuum of the SEM chamber. LiPON is a model electrolyte because it is well characterized and amorphous, avoiding any complexities arising from grain boundaries.

To connect to the cell, Cu tape or foil is attached to contacts on the cell substrate using Ag epoxy in an Ar-filled glovebox. The cell is then mounted onto an SEM stub on top of Kapton tape to prevent short circuiting from contacts on the back of the cell. Before experiments, electrochemical impedance spectroscopy (EIS) measurements are performed on the cells in the glovebox to test that they are well connected. EIS does not charge or discharge the cell, so it does not affect subsequent electrochemical experiments. During EIS, an oscillating voltage at various frequencies is applied to

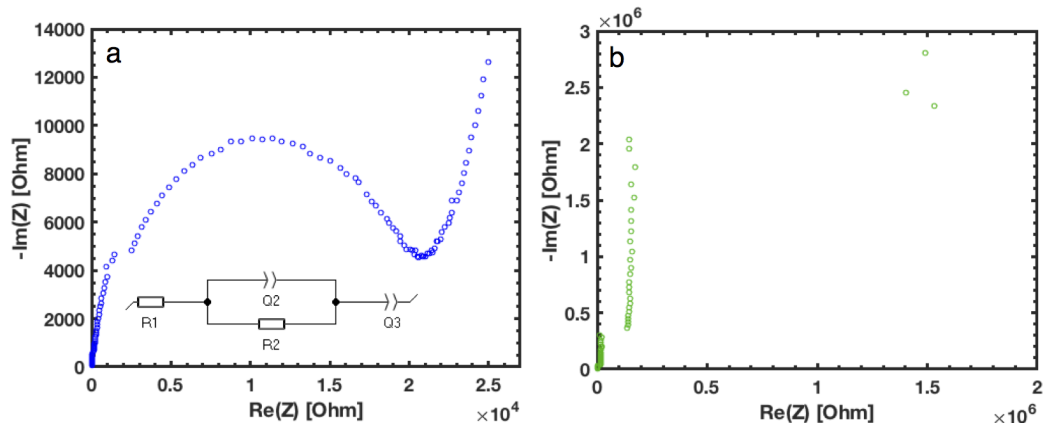


Figure 2.2: (a) Typical Nyquist plot for well-connected solid-state thin film cells before charging. R1, Q2, R2, and Q3 corresponds to electrical resistance, geometric capacitance, R_b , and double layer capacitance, respectively. The jump around $0.2 \times 10^4 \Omega$ on the $\text{Re}(Z)$ axis is due to a change in frequency channel in the potentiostat. (b) Typical Nyquist plot for poorly-connected cells. Note the scales of the axes, which are $\sim 100x$ greater than those in (a).

measure the complex impedance response of the cell. A common representation of EIS is the Nyquist plot (see Figure 2.2(a)), in which the real and negative imaginary parts of the impedance are plotted, and each point corresponds to a single frequency. The signature of a well-connected cell should be a semicircle with a straight line at lower frequencies (larger impedances). EIS was measured using a BioLogic SP-200 potentiostat between 3 MHz and 1 Hz with a perturbation of 10mV.

The semicircle seen in the Nyquist plot in Figure 2.2(a) for a cell used in this study is commonly attributed to the geometric capacitance between the electrodes in parallel with the overall resistance of the cell (bulk resistance, R_b) [72, 83]. The first x-axis intercept at the highest frequencies corresponds to the electrical resistance of the system (wires, contacts, Ag epoxy, etc.) and the straight line at low frequencies is attributed to double layer capacitance [83]. R_b is dominated by the resistance of LiPON, so R_b can be used directly to calculate the ionic conductivity of the LiPON layer using:

$$\sigma = \frac{L}{AR_b} \quad (2.1)$$

where σ is the ionic conductivity, L is the thickness of the LiPON layer, and A is the cross-sectional area of the electrolyte. An equivalent circuit (Figure 2.2(a)) is fit to the data, providing a LiPON conductivity of $2 \times 10^{-6} \text{ S/cm}$ using $L = 4 \mu\text{m}$ and $A =$

1 mm². This is consistent with conductivities reported in literature [76]. Constant phase elements (CPEs, represented by Q in the circuit diagram) are used instead of capacitors to fit the depressed (wider than tall) semicircles. A CPE represents an imperfect capacitor, with imperfections attributed to inhomogeneities and roughness in the electrodes [83, 84]. If the cell exhibits an impedance response as shown in Figure 2.2(a), then it is well-connected and can be used for *in-situ* charging in the SEM.

If the cell is poorly-connected, the EIS will reveal a Nyquist plot that approaches a vertical line, such as the plot shown in Figure 2.2(b). This Nyquist plot represents capacitive behavior with deviations arising from the change in frequency channels in the potentiostat. This capacitive behavior implies that the cell is disconnected somewhere, likely due to defects in the connections involving Ag epoxy or electrical contacts on the cell, and cannot be charged. The open circuit voltage (OCV) is the voltage of the cell under no applied current. The OCV for a well-connected cell typically ranges between about -50 and 50 mV with deviations < 1 mV/s. Generally in an electrochemical cell like a battery, the OCV will be defined by the voltage produced by the battery. However, because our cells start Li-free, the potential is determined by only one electrode and the OCV is ill-defined. After some Li is plated, the OCV reaches ~3.9 V. When the cell is not connected, the OCV will become larger (commonly $|V| > 1$ V) with large fluctuations around 100 mV/s or more. OCV is another simple tool in addition to EIS to determine which cells will work for the *in-situ* charging experiments.

The cell-mounting details are critical for the performance of the SEM experiments. Because the cell is mounted vertically in the SEM chamber with the side of the stub close to the electron beam column, any mm-sized Kapton tape will cause a large distortion in the electron image due to Kapton tape being an electrical insulator (Figure 2.3). Care was taken to minimize the amount of exposed Kapton tape, especially on the edge of the cell, while preventing short circuits. A conductive carbon pen was used when necessary to cover exposed areas of Kapton tape. The electrical clips were also coated in Kapton tape to prevent short circuiting.

The cells were attached to an SEM stub (Figure 2.4(c)) and placed into a custom *in-situ* SEM instrument (Quanta 200 SEM, FEI) that has a nanoindenter arm (InSEM, Nanomechanics, Inc.) and an electrical port mounted on the testing chamber (Figure 2.4(a)). The electrical port is connected to a potentiostat (BioLogic SP-200) outside the instrument and to electrical contacts on the sample within chamber

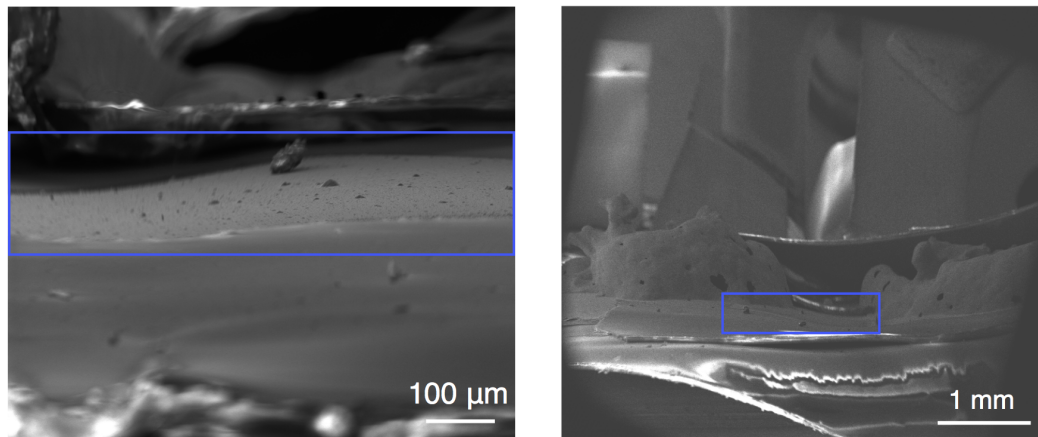


Figure 2.3: SEM images of the thin film cell with image distortion from Kapton tape, seen at the bottom of the images. The cell is contained in the blue rectangle. This distortion generally precludes any high magnification imaging and the ability to perform nanomechanical experiments.

(Figure 2.4(b)). The chamber was pumped down to $< 5 \times 10^{-5}$ torr, and the Li electrodeposited galvanostatically at 0.3 mA/cm^2 or potentiostatically at 4.1 V. Li growth was imaged in real time in the SEM during charging.

2.3 *In-situ* Uniaxial Compression

The SEM instrument that can perform *in-situ* electrochemical experiment can also perform mechanical experiments using a nanomechanical indenter arm. The nanoindenter head is attached to the end of the indenter arm and measures the load and displacement of the sample. Figure 2.5 illustrates the components of the nanoindenter head, which is inherently load controlled; a desired displacement is reached by applying load. To administer a load to the sample, the head applies a voltage on an electromagnetic driver coil. The head measures displacement from the applied load using a capacitive gauge, which is sandwiched between two support leaf springs with large lateral stiffnesses to reduce lateral motion of the head. The tip that will contact the sample is screwed into the bottom of the head before the head is inserted into the SEM.

Uniaxial compression tests of vertically-oriented, electrodeposited Li pillars (height: diameter aspect ratios of 3:1-5:1) were conducted in the same SEM chamber in which they were deposited immediately after charging the cell. These nanomechanical tests were performed by compressing individual nano-pillars with a $5 \text{ }\mu\text{m}$ diamond flat-punch indenter tip at a nominal strain rate of $\sim 3 \times 10^{-3} \text{ s}^{-1}$ or at a prescribed

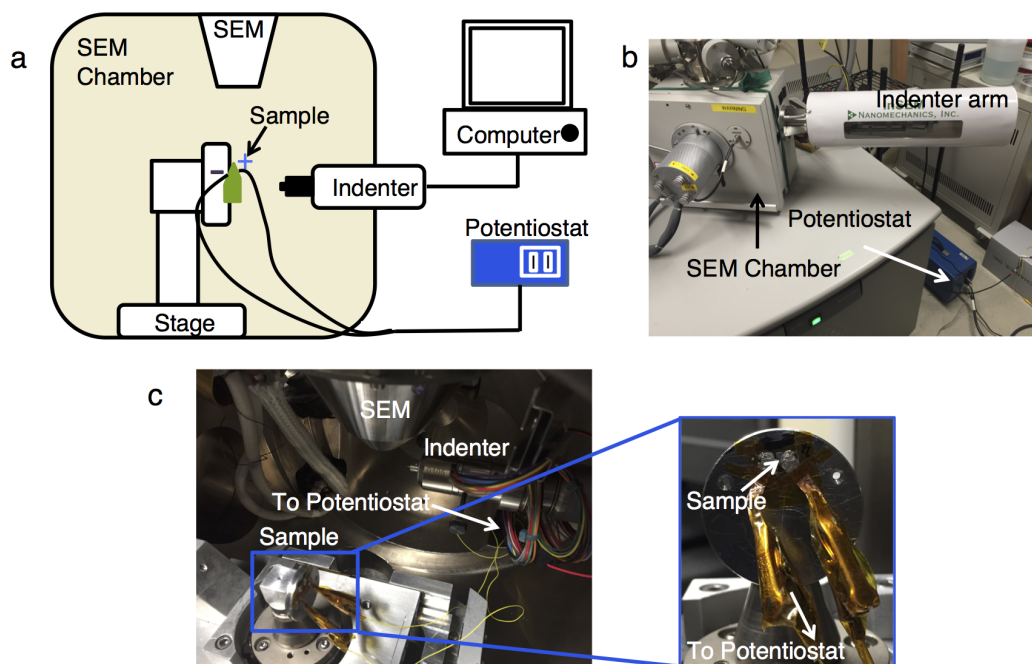


Figure 2.4: (a) A schematic of the *in-situ* electrochemical charging experiment. Photographs of (b) the *in-situ* instrument and (c) each component within the SEM chamber. The sample is mounted onto the SEM stub; clips connected to the potentiostat outside the chamber are attached to the Cu tape connected to the cell inside the chamber.

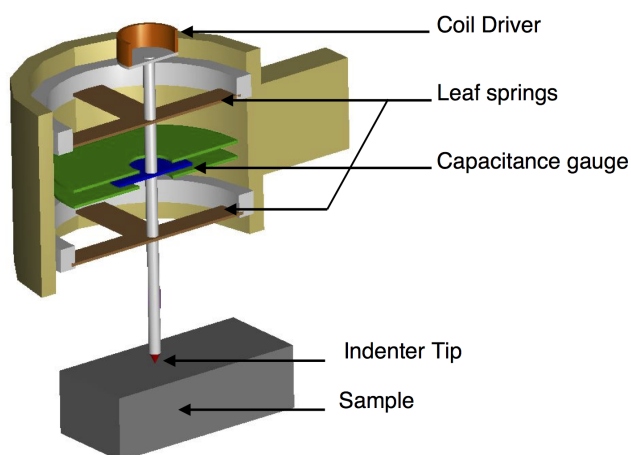


Figure 2.5: Schematic of the components of the nanoindenter head adapted from Agilent Technologies [85].

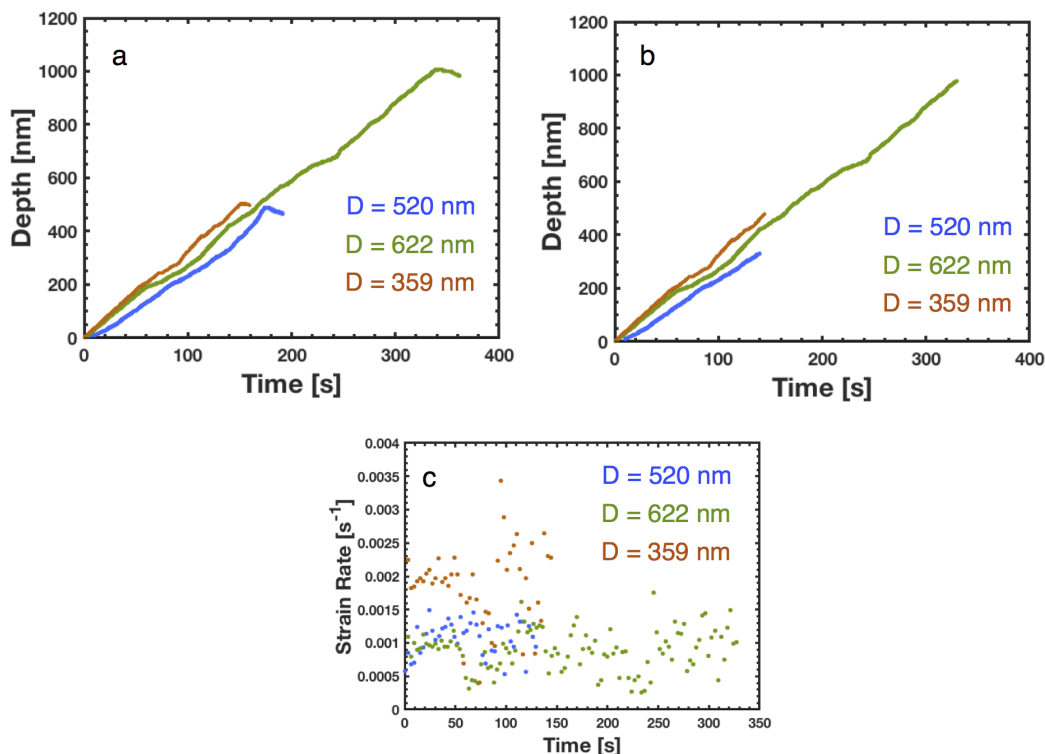


Figure 2.6: Examples of displacement vs. time for three pillars compressed at $0.5 \mu\text{N/s}$ throughout the whole experiment (a) and data cutoff to the relevant linear portion (b). (c) shows the strain rate from the curves in (b) taken at 3 second intervals.

loading rate of $0.5 \mu\text{N/s}$ (corresponding to an effective strain rate of $\sim 1 \times 10^{-3} \text{ s}^{-1}$, see Figure 2.6). The experiments were conducted in the continuous stiffness measurement (CSM) mode (in addition to the global constant strain rate), where the indenter tip oscillated with an amplitude of 0.5 nm at a frequency of 45 Hz . The *in-situ* experiment allowed the transfer of Li into the SEM without exposure to air, which is critical to investigate Li metal; the Li was also never exposed to a Ga^+ ion beam, as commonly used in FIB pillar carving [40, 86]. The cell was charged at a constant current density of 0.3 mA/cm^2 to increase the likelihood of locating vertically oriented isolated pillars of the target aspect ratios.

The compression experiments with a prescribed constant loading rate of $0.5 \mu\text{N/s}$ were in effect performed under a relatively constant displacement (strain) rate (Figure 2.6). The constant strain rate is due to the applied force being linear with time, but when corrected for the spring stiffness, load deviates from linearity because the sample dynamic stiffness is on the same order as the spring stiffness. This allows the displacement rate to be relatively constant, although small deviations in linearity

correspond to the deviations in linearity in load and stress-strain behavior. To calculate the effective strain rate for a prescribed loading rate, the depth vs. time data needs to be analyzed, as shown in Figure 2.6(a). The depth is mostly linear with time until unloading near the end of the experiment with a negative displacement rate. The curves can also be nonlinear at the very beginning of the experiment as the indenter tip contacts the sample. Figure 2.6(b) removes these nonlinearities by cutting off the very beginning and end of the data. The displacement rates, and thus strain rates, are relatively constant throughout the experiment. The R^2 values for linear fits in this region of the experiment range from 0.997 to 0.999. The maximum effective strain rate, taken at 3 second intervals (Figure 2.6(c)), is $3.4 \times 10^{-3} \text{ s}^{-1}$, with an average of $1.2 \times 10^{-3} \text{ s}^{-1}$ between the 3 pillars, demonstrating the quasistatic nature of the prescribed load-rate compression experiments.

Chapter 3

FORMATION OF LI IN LI-FREE SOLID-STATE BATTERIES

Adapted from

1. Citrin, M. A., Yang, H., Nieh, S. K., Berry, J., Gao, W., Pan, X., Srolovitz, D. J., & Greer, J. R. From Ion-to-Atom-to-Dendrite: Formation and Nanomechanical Behavior of Electrodeposited Lithium. (*In preparation*).

This chapter will address the formation of Li in thin film solid-state cells using the experimental methods described in the previous chapter. The sections will generally focus on the observation that Li preferentially grows at the domain boundaries on the surface of the cell, and the implications thereof. The chapter will begin with a brief introduction into Li-free cells.

3.1 Introduction-Li-free Cells

Neudecker et al. [79] investigated Li-free thin film batteries, which avoids excess Li in the battery and the need for special equipment to deposit Li. These batteries only cycled stably with cathodes thicknesses up to 3 μm (which corresponds to only $\sim 1 \mu\text{m}$ of electrodeposited Li) due to the electrodeposition-induced volumetric expansion. Substantially thicker Li deposits are required for most applications; for example, to reach the US Department of Energy capacity goal of 5 mAh/cm^2 , $\sim 25 \mu\text{m}$ of Li must be cycled on each charge [2]. This requires substantially thicker cathodes and further exploration of the mechanism and limitations of electrochemical Li growth.

In an approach similar to the work presented here, Motoyama et al. [72] used a custom symmetric (both electrodes were Li) thin film solid-state cell with LiPON deposited on both sides of a $\text{Li}_{1+x+y}\text{Al}_x\text{Ti}_{2-x}\text{Si}_y\text{P}_{3-y}\text{O}_{12}$ (LATP) SE sheet with a smooth topography and cycled it *in-situ* inside an SEM chamber. The authors discovered that rod-like Li deposits penetrated a thin ($\leq 100 \text{ nm}$) Cu current collector on top of LiPON, while large ($> 5 \mu\text{m}$) bumps formed under thicker ($\geq 1 \mu\text{m}$) Cu films. By modeling the Li particle as a hollow spherical shell with internal pressure induced by its growth, these authors suggested that the radial (normal) stress on the Li particle associated with the Cu film constraint to be 0.1-1 GPa [72]. The flat

topography contrasts the nodular surface of our cell; the importance of this will be discussed in the subsequent sections.

3.2 Li Electrodeposition

Figure 3.1(a) shows a time-lapse SEM image sequence of the Cu thin film surface during charging at 0.3 mA/cm^2 at the capacities indicated in Figure 3.1(b). These images reveal the emergence of $\sim 400 \text{ nm}$ diameter bumps that preferentially form at bundle domain boundaries (local minima or cusps in the Cu surface morphology) once the charging voltage exceeds $\sim 4 \text{ V}$. Continued charging produces a negligible voltage increase at these capacities (Figure 3.1(b)). When the charging capacity reaches $\sim 10 \text{ } \mu\text{Ah/cm}^2$, the bumps start to crack, and the Li that formed at the LiPON/Cu interface pierces the Cu film (Figure 3.1(a,ii)). With further charging, additional Li deposits at other bundle domain boundaries, and the existing Li continues to grow (see Figure 3.2 for additional Li growth images and details).

Figure 3.1(c) shows different observed electroplated Li morphologies: (1) up to $\sim 1 \text{ } \mu\text{m}$ diameter sphere-like particles, (2) pillars with diameters from $\sim 300 \text{ nm}$ to $\sim 1 \text{ } \mu\text{m}$ that grew in all directions from the substrate, and (3) $100\text{-}300 \text{ nm}$ diameter fibers with aspect ratios $>5:1$. Some of the Li particles looked faceted (Figure 3.1(c,iv)).

Upon charging, Li is formed at the LiPON / Cu interface, and then fractures through the thin Cu layer once the Li particle is large enough. More evidence of this is shown in the SEM images in Figure 3.2. Figure 3.2(a) shows the bumps in the Cu that form at the beginning of charge as the Li has grown and has just started to fracture the Cu surface. Figure 3.2(b) reveals Li growing at areas with fractured Cu. The dark areas in the red circles arise from the underlying LiPON layer, as the images were taken at 10 kV . The low Z of Li allowed the electron beam to penetrate through, illustrating the lack of Cu directly under the Li. Finally, Figure 3.2(c) shows Li particles at the end of charge with Cu “caps” attached from puncturing through the Cu current collector at the beginning of growth. The contrast is due to the low Z of Li, which appears darker under secondary electron imaging.

3.3 Preferential Li Formation at Domain Boundaries

The *in-situ* SEM experiments conducted in our work revealed that Li first nucleated at the LiPON/Cu interface as the Li ions in the electrolyte are reduced from the current collector and the amount of Li solubilized by the Cu is negligible. Under the Cu film, the Li first formed multiple $\sim 400 \text{ nm}$ diameter bumps that decorated the valleys of the nodular relief of the film stack associated with the LCO bundle domain boundaries

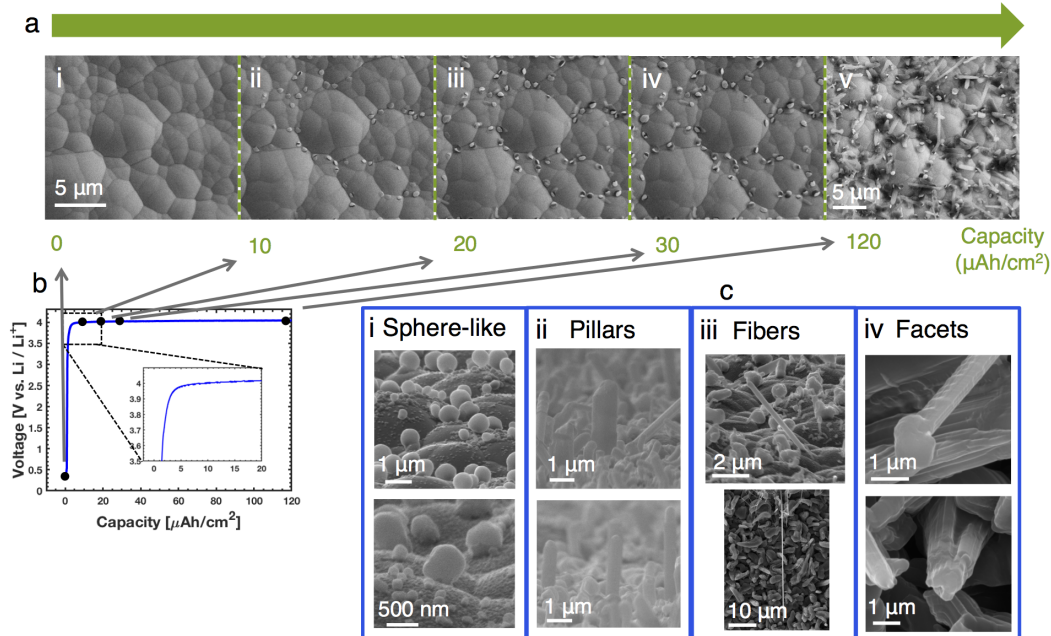


Figure 3.1: (a) Time-lapse SEM images that depict morphology evolution viewed from above the Cu layer during charging at 0.3 mA/cm^2 . (b) Charging profile with black points along the curve corresponding to the capacities in frames i-v in (a). (c) Different morphologies of electrodeposited Li that formed during charging at 0.3 mA/cm^2 to between 35 and $75 \text{ } \mu\text{Ah/cm}^2$ (i-iii) and at the end of charge (iii-iv).

— see Figure 3.1(a,i-ii). The Li then ruptured the Cu film at those locations and grew unimpeded (see Figure 3.1(a,ii) and 3.2). This resulted in different morphologies: Li fibers, pillars, and spheres (Figure 3.1(a,iii-iv)). Similar film rupture-followed-by-protrusion Li nucleation and growth behavior was observed by Motoyama et al. [72]; however, the smooth surface topography in their cell only produced rod-like Li protrusions. This is in contrast to our system, which exhibited a nodular surface topography and produces a variety of Li morphologies (Figure 2.1, 3.1(c)).

While a symmetric Li cell is useful for detailed voltage analysis, a cathode is needed to store energy, and vapor-deposited transition metal oxides (e.g., LCO) are common Li battery cathodes[76, 77]. The nodular surface morphology of our full cell is a common morphology in many commercial thin film solid-state batteries. We note, however, that unlike in commercial batteries which have an overlayer to increase cycle life and prevent air exposure, in our SEM experiments there is no overlayer (and hence no constraining pressure). Neudecker et al. [79] added a LiPON overlayer to a Li-free thin film battery that successfully cycled $1 \text{ } \mu\text{m}$ of Li 1000 times and found that at the end of first charge, the Li formed as individual particles instead of

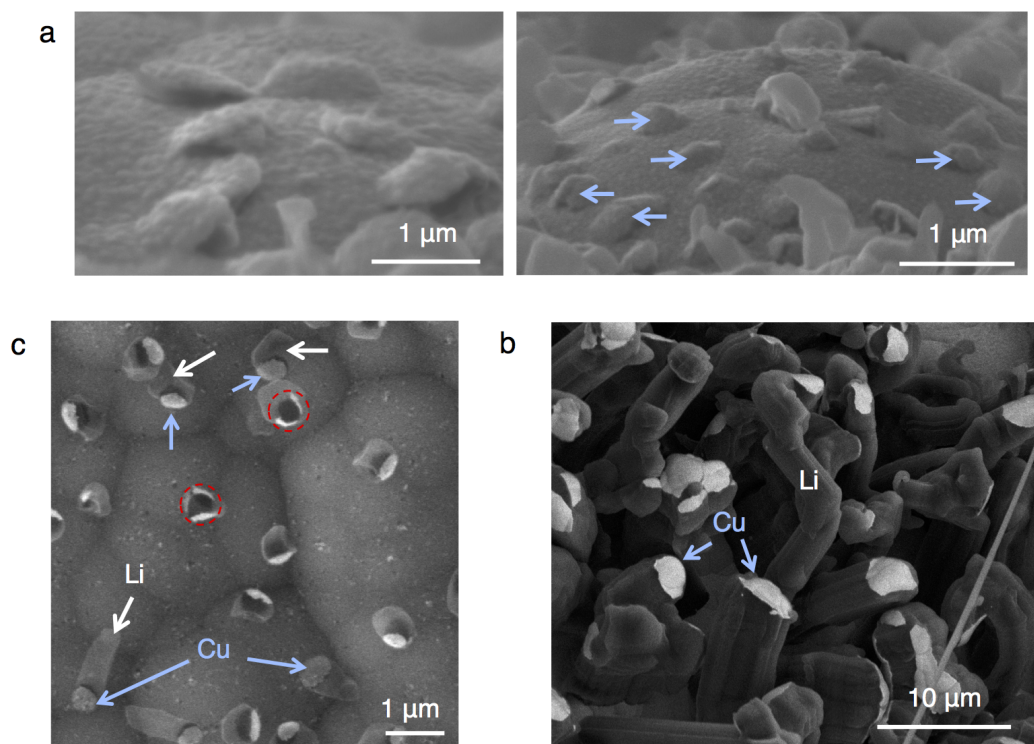


Figure 3.2: (a) Side-view SEM images showing bumps in the Cu (blue arrows) caused by Li growing underneath. (b) Top down SEM image showing Li (labeled in white) growing at areas with fractured Cu (labeled in blue). The dark areas in the red circles are from the underlying LiPON layer. (c) Top down SEM image showing Li (dark) particles with Cu (light) “caps” attached.

a smooth, continuous film. This morphology is similar to that of the Li observed in our work. Their Li thickness corresponds to $207 \mu\text{Ah}/\text{cm}^2$ which is $\sim 3\text{-}6\text{x}$ greater than the charge passed when we observed our initial Li morphologies. It is likely that the Li morphologies and current collector rupture correspond to the Li formed in thin film batteries at the beginning of charge ($< \sim 200 \mu\text{Ah}/\text{cm}^2$), even under an applied pressure from an overlayer. Thicker current collectors will suppress the rupture and allow the Li to plate underneath this layer, while the Li morphologies may evolve as more charge is passed and at subsequent cycles [72, 79].

To help understand the propensity for Li nucleation and growth along the topographical minima (cusps/valleys between domains) of the LiPON/Cu interface and the various Li morphologies observed in experiments, we simulated Li ion transport across the SE with the observed nodular cross-sectional geometry using COMSOL [87] Multiphysics[®] (Figure 3.4(a)). The Nernst-Planck equation for ion transport

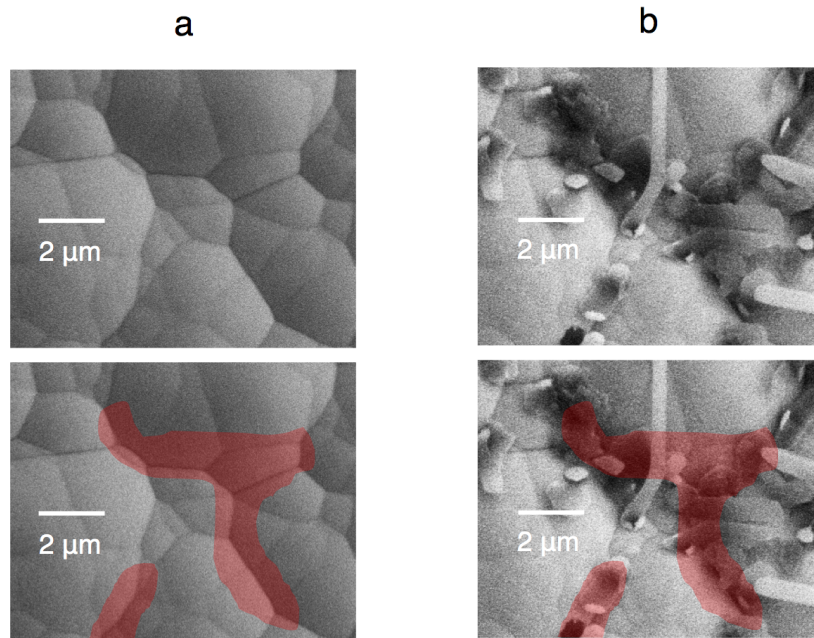


Figure 3.3: (a) Top down SEM images before charge showing areas of steeper curvature on the surface of the cell in red. (b) Top down SEM images after charging at 0.3 mA/cm^2 for $120 \text{ } \mu\text{Ah/cm}^2$. In the red areas, the Li morphology is more uniform / sphere-like, and the density of Li deposits is larger, both due to effects of the surface topography.

in the presence of an ion concentration gradient and an electric field was solved using a finite element method. We employed a constant applied current density (3 A/m^2), electrolyte conductivity (0.0001 S/m [88]), temperature (293 K), cathode thickness ($40 \text{ } \mu\text{m}$), electrolyte thickness ($4 \text{ } \mu\text{m}$, unless specified otherwise), Li diffusion coefficient ($3 \times 10^{-16} \text{ m}^2/\text{s}$ [89]) and various SE surface morphologies and amplitudes.

Figure 3.4 shows simulation results which demonstrate that an applied potential across the cell stack leads to current density enhancements near the cusps/valleys in the LiPON/Cu interface. This topography drives enhanced, localized Li ion flux into these regions (Figure 3.4(b)) leading to preferential Li metal nucleation and growth at the cusps at the LiPON/Cu interface (beneath the Cu film) (Figure 3.4(c)). This is consistent with our observation that Li metal is first observed on the top surface of Cu near the cusped valleys in the surface morphology (see Figure 3.1 (a, (ii))). Simulation results showed no qualitative dependence on surface profile type (cusped, $z = h[1 - (1 - 2|x|/w)^{1.75}]$; sawtooth, $z = 2h|x|/w$; or sinusoidal, $z = h \sin(2\pi w)/2$, where h and w are the heights and widths of the surface profile

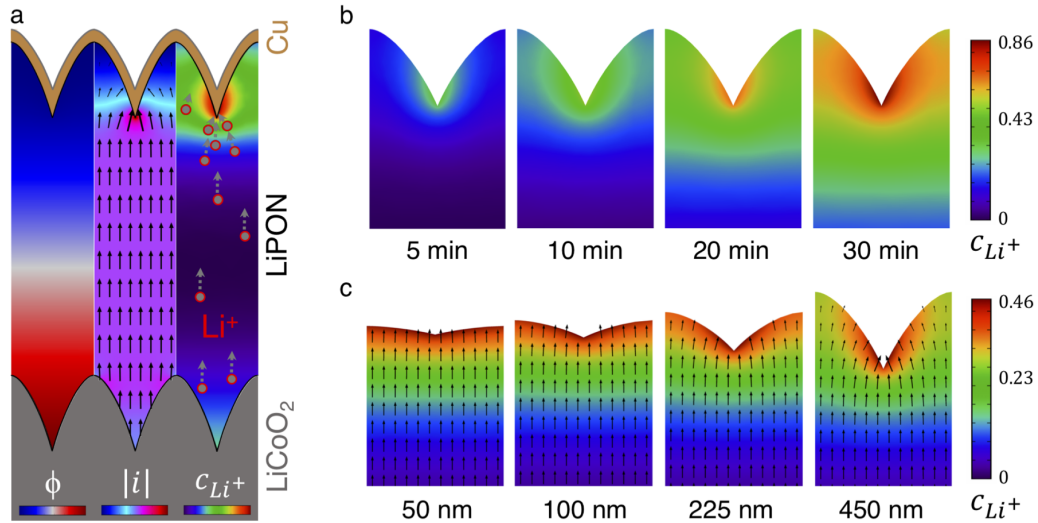


Figure 3.4: Electrochemical simulations of electrolyte potential ϕ , current density i , and Li⁺ concentration c_{Li^+} in the LiPON and at the LiPON/Cu interface. (a) Representative maps of ϕ , current density magnitude $|i|$ (colors) and field \vec{i} (arrows; lengths proportional to $|i|$), and c_{Li^+} across the cell. Current density and Li⁺ concentration exhibit distinct maxima near the cusps/valleys. (b) Representative Li⁺ concentration maps at progressively longer lithiation times that convey highest Li⁺ accumulation in the vicinity of a groove. (c) Maps of Li⁺ concentration and \vec{i} for three groove geometries (varying convexity) at $t = 10$ min that show increased current density and Li⁺ concentration enhancement near grooves with increased height-to-width ratio (width = 800 nm, height as indicated).

$z(x)$). The expansion associated with Li deposition generate an overall biaxial tensile stress within the Cu film that facilitates localized rupture of the film near the valleys where the Li deposition/expansion is a maximum. This geometric effect is only visible using a thin film full cell with a surface geometry associated with an underlying LCO layer.

The potential for more rapid Li deposition and growth at sharper bundle domain boundaries could be beneficial; they allow the cell to more effectively discharge/charge at higher currents. However, the heterogeneity in the surface profile produces a distribution of Li on top of the Cu film with different morphologies and sizes, which may impair cycle life as the Li will strip/deposit non-uniformly [89]. Hence the overall effect on battery performance is unclear.

3.4 Li Morphologies

We observed in our *in-situ* experiments that the sphere-like Li is more likely to grow at sharper domain boundaries; slender pillars and fibers tend to grow away from these locations (Figure 3.3). The geometry of Li deposits is likely determined by the local surface topography and local current density. The local current density of a Li deposit can be calculated from the charge passed, C , for a Li particle at a time step t , defined as:

$$C = V(t)\rho_{Li}M_{Li}F \quad (3.1)$$

where $V(t)$ is volume, ρ_{Li} is the density of Li, M_{Li} is the molar mass of Li, and F is the Faraday constant, assuming a Li^+ transference number of 1 through LiPON. C was plotted against time to obtain a linear relationship where the slope of the C vs. t plot is defined as the local current. The area to determine current density was calculated using a circular cross section using the diameter (for a fiber or pillar) and using the square of the measured length of the contact between the particle and surface (for a sphere; the sphere-like Li contacts the surface as a spherical cap). The volume of the sphere was calculated by estimating the depth as the average between two orthogonal axes across the surface and multiplying it by the area seen in the SEM. The local current density applied to grow a Li pillar was calculated as ~ 5 mA/cm^2 when the global current density was 0.3 mA/cm^2 , while the local current density to grow a Li sphere was ~ 90 mA/cm^2 when the global current density was 0.1 mA/cm^2 .

We hypothesize that at the larger local current densities associated with sphere-like deposits, the Li may be driven to diffuse toward the upper surface of the exposed deposit as the local concentration of Li ions drives increased stresses on the Li deposits (Fig. 6(c)), inducing growth near the top of the particle and spherical cap formation, while at the smaller local current densities associated with fibers or pillars, the Li fiber or pillar grows from the bottom as Li ions are reduced at the LiPON/Li interface. The self-diffusion rate of Li at room temperature is large enough to accommodate the growth rate of sphere-like particles, assuming a diffusion distance of $\sqrt{6D_{Li}t}$, where D_{Li} is the self-diffusion coefficient of Li and t is time. This diffusion distance is an underestimate because it does not take account of the external driving force of a stress gradient. The Li self-diffusion coefficient (6×10^{-15} m^2/s [90]) is 20x larger than that of Li in LiPON (3×10^{-16} m^2/s [89]) at 298 K. This difference in diffusion coefficients (20x) is similar to the difference in

measured local current densities ($\sim 18\times$). It is plausible that Li fibers and pillars grow in an electrolyte-limited transport regime and sphere-like Li grows in a Li-diffusion limited regime. This mechanism is consistent with the results of the simulations, as the local current density will be largest directly at the boundaries at the topographic minima, producing more sphere-like Li. The morphology of the initial Li deposits are then determined by the surface topography of the cell, in contrast to Li deposited in a liquid electrolyte, whose morphology is determined by the current distribution around the particle and is more fiber-like at higher current densities [91]. Without the surface topography-based local current enhancement, Li should deposit only in fiber or pillar morphologies, as was observed on a flat LiPON/Cu interface [72].

3.5 Conclusions

In-situ electrochemical experiments were performed on a commercial, solid-state Li-free, LiCoO₂ (40 μm , cathode)/LiPON (4 μm , solid electrolyte)/Cu (30 nm, current collector) thin film battery inside an SEM chamber. These experiments, in addition to numerical simulations, demonstrate that during cycling of the cells, Li preferentially nucleates and grows at the local topographical minima on the Cu/LiPON interface along the LCO bundle domain boundaries arising from the underlying cathode layer. Further deposition of Li ruptures the Cu film and grows into different morphologies: spheres, pillars, and fibers with dimensions $\leq 1 \mu\text{m}$. The growth of sphere-like Li is correlated with the topographical-enhanced current densities at the cusps of the Cu/LiPON interface.

*Chapter 4***MICROSTRUCTURE OF LI ELECTRODEPOSITED FROM A SOLID ELECTROLYTE**

Adapted from

1. Citrin, M. A., Yang, H., Nieh, S. K., Berry, J., Gao, W., Pan, X., Srolovitz, D. J., & Greer, J. R. From Ion-to-Atom-to-Dendrite: Formation and Nanomechanical Behavior of Electrodeposited Lithium. (*In preparation*).

This chapter will investigate the microstructure of the Li electrodeposited from thin film solid-state cell, as discussed in the previous chapters. Various methods to effectively transfer Li into the TEM chamber for microstructural analysis will be considered. Ultimately, cryo-EM was chosen as the method to probe the microstructure of Li and its transfer method and results will be discussed in the following sections.

4.1 Challenges Performing TEM Analysis on Li

Chapter 3 describes the formation of Li in thin film solid-state batteries. Li was electrodeposited in various morphologies generally $< 1 \mu\text{m}$ in size. As mentioned in Section 1.4, the microstructure of metals greatly influences their strength, especially at these submicron length scales. For example, single crystalline, submicron samples can exhibit much larger strengths than bulk poly-crystals [43] and the crystallographic orientation of single crystals can greatly affect the modulus for an anisotropic material like Li [40].

The principle technique for revealing microstructural information on the atomic level is transmission electron microscopy (TEM). During TEM analysis, high energy electrons bombard a thin sample and transmit through it to reveal microstructural information about the sample, even at atomic resolution. Electron diffraction can also be performed to investigate the crystal structure of small samples. TEM is particularly challenging to perform on Li because of Li's extreme reactivity with air and sensitivity to high-energy electron beams [92]. Conventional preparation methods using polishing and FIB lift-out do not lend themselves to handling Li because Li will quickly react with air at the thicknesses needed for electron transparent samples

(< 1 μm for a low Z material like Li) [92]. Attempts to examine the microstructure of electrochemically cycled Li have had limited success because of challenges with oxidation and beam sensitivity [92–94], allowing for only low magnification observation in the TEM [95] and inconclusive microstructural observations [92, 96].

4.2 *In-situ* TEM

Typically, TEM analysis is performed on samples in the state they remain during analysis. *In-situ* TEM is a valuable tool that can directly observe the dynamics of samples under different conditions, including electrochemical cycling. For example, Mehdi et al. [95] used an *in-situ* microfluidic electrochemical TEM holder to directly observe the plating and stripping of Li in a conventional liquid electrolyte. Thin foils of solid-state thin film batteries fabricated using the FIB have been examined using *in-situ* biasing in the TEM. These "nanobatteries" can be cycled by connecting one electrode to a TEM grid and the other to a nanoprobe [97] or connecting both electrodes to a microelectromechanical system (MEMS) device [98] to examine solid-state transformations in the electrodes during cycling. No known study has investigated the microstructure of Li deposited using *in-situ* TEM.

In-situ TEM techniques would allow for the transfer of Li metal into the TEM chamber without air exposure by utilizing a thin cross section of a Li-free battery as the sample. All the Li would be initially stored in the cathode, and the Li would form in the TEM under high vacuum when the sample is charged, similar to the SEM experiments. A thin cross-section of the Front Edge solid-state thin film battery was carved with the FIB using standard TEM sample FIB lift out procedures. First, ion beam induced-deposited (IBID) Pt was locally applied to the top of the sample to protect the Cu and LiPON layers and to increase the thickness of the top conductive layer. Next, a thin cross-section of the battery (IBID Pt/Cu/LiPON/LCO) was FIB milled with Ga^+ ions (30 kV unless otherwise noted) to about 25 μm wide and 14 μm deep and lifted out using a nanoprobe (Omniprobe). Instead of a TEM grid, the samples were then moved to an E-chip (Protochips [99]), which was eventually placed into the TEM holder. The E-chip is a Si chip with a trench at the edge and patterned Au electrodes at either side of the trench that connect to larger electrodes at the other end of the chip (see Figure 4.1(a, b)).

The sample is then placed down over the trench and electrically connected to the electrodes using IBID Pt because IBID Pt is much more electrically conductive than electron beam induced-deposited (EBID) Pt [98]. Some EBID Pt is occasionally

used to help mechanically attach the sample to the chip, but there still needs to be an electrically conductive pathway between the IBID Pt and the electrodes. While the E-chips are designed to make this step as simple as possible, it is still more difficult than standard FIB lift out. The difficulty arises for several reasons: the nanoprobe must move close to the E-chip to place down the sample, while the probe can easily touch the chip accidentally to prevent attachment. The orientation between the chip and sample needs to align very closely, and attaching the sample parallel to the substrate is more difficult due to the orientation of the FIB and Pt source. Occasionally during the sample attachment-to-chip step, slight drifting would move the chip relative to the sample and bend the connection between the sample and probe, ruining the sample, as illustrated in Figure 4.1(d). Great care needed to be taken to electrically connect the sample to the electrodes without any short circuit. The whole length of the sample was thinned/cleaned after connection to the E-chip to help prevent shorting from the redeposition of material from the earlier, larger FIB cuts. To help prevent shorting between the Au electrodes across the trench from the IBID Pt layer or LCO, notches were cut at 8 kV between the LCO and LiPON and the Pt/Cu and LiPON; this should allow ion transport through LiPON to be the only mechanism of current between the Au electrodes (Figure 4.1(c)). The sample was then thinned to an electron transparent (~ 100 nm) thickness at low voltage (8 kV) to reduce Ga^+ damage. Once finished, the samples were immediately sealed in a vacuum sealed bag, then transferred to an Ar-filled glovebox within 10 minutes.

Once the samples were attached to the E-chip and sufficiently thinned, they were taken the TEM (JEOL JEM-ARM300F Grand ARM) at the University of California, Irvine Materials Research Center (IMRI) and placed into the TEM holder (Protochips Fusion). The samples were transferred into the TEM in under one minute. Unfortunately, many samples fell off the E-chip at some point between the FIB and the TEM. Once inside the TEM, the samples were charged at constant current or voltage using a Gamry Reference 600 potentiostat. We expected the Li to grow from the Cu/Pt layer, similar to how it grew in the SEM (Figure 3.1). Seven lift out samples were attempted on five different days and all exhibited an unstable electrical response. Figure 4.2(a, b) demonstrates that, for example, -12 V was measured when applying 100 pA to a sample, and applying 5 V, 10 V, or -10 V all resulted in a response of ~ 1 μA .

The inconsistent electrical response is likely due to some high resistance shorting happening across the cell, possibly from Ga^+ damage of the LiPON layer and

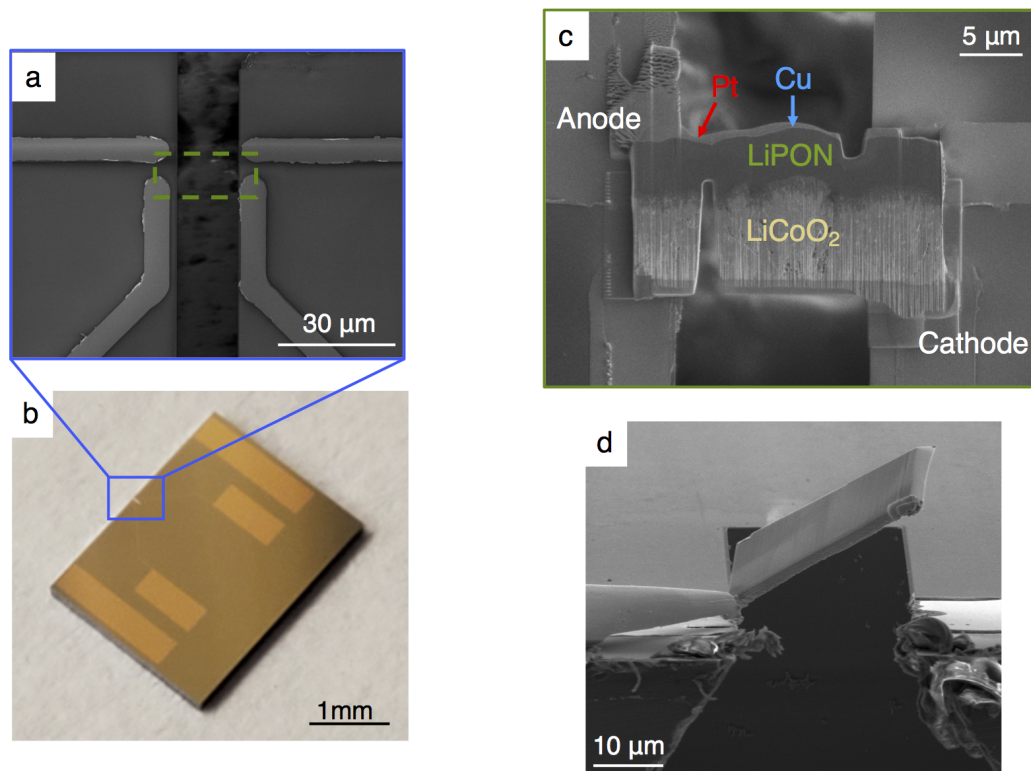


Figure 4.1: (a) The 4 Au electrodes surrounding the trench (center) on the E-chip. (b) The entire E-chip contains 4 larger Au pads connected to the 4 electrodes in (a). (c) Representative FIB lift out sample of the cell cross-section placed in the green box in (a). The electrodes are connected with IBID Pt on both sides of the trench. The anode side (Cu/Pt) is attached to the left electrode and the cathode side (LCO) is connected to the right electrode in this configuration. The Cu layer lies in between the IBID Pt and LiPON. (d) Example of a small drift moving the chip into the probe during sample attachment. This bends the sample at a large angle, preventing sample attachment.

redeposited material. It is difficult to remove redeposited material on the bottom side of the sample where it lies on the chip and around the notches. One way to potentially avoid the redeposition issue is to attach the sample to the E-chip in an orientation 90° from previous attempts so that the layers of the cell line up parallel to the trench (Figure 4.3(c)). This angle places each electrode on either side of the trench. The orientation allows for direct cleaning of the LiPON layer that lies completely in the trench; any short along the Cu/Pt or LCO layer will not short the sample because the LiPON should be clear of redeposited material. However, the lift out procedure in this orientation is much more difficult to perform. The thin film battery must be oriented with its cross section facing up towards the electron

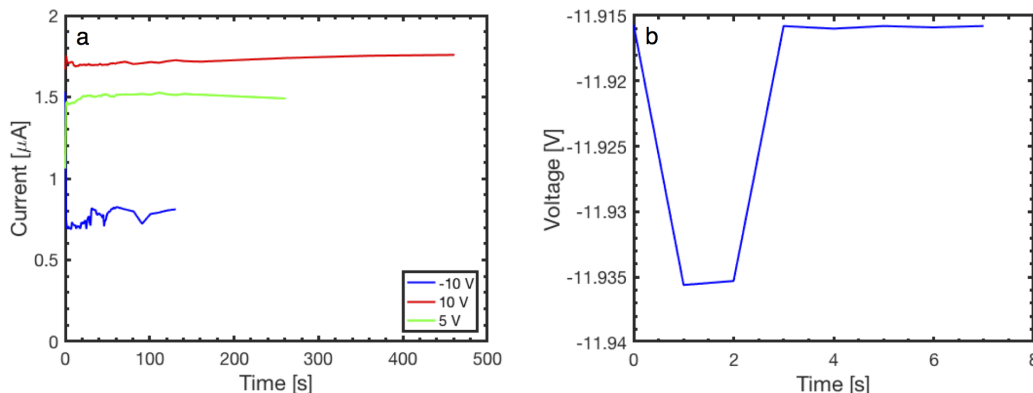


Figure 4.2: Electrical response of a sample similar to the one shown in Figure 4.1(c). (a) The current response under an applied voltage of 5 V, 10 V, and -10 V. (b) The voltage response under an applied current of 100 pA.

beam to be seen by the FIB and electron beam and be reachable by the Pt needle and nanoprobe, which are all orientated at different angles compared to the sample. The relative views in the FIB and SEM, for example, are shown in Figure 4.3(a,b). The cell was fractured with a razor blade in the glovebox and the remaining part of the cell was attached to the edge of an SEM stub and placed vertically onto a 90° SEM cube in the SEM chamber. To be observed in the TEM, the area where Li will grow cannot lie over the E-chip (Figure 4.3(c)). The samples were therefore attached partially over the edge of the sample above the electrodes, and IBID Pt lines were used to connect the Au electrodes to the Cu/Pt and LCO. Unfortunately, drifting again prohibited the successful attachment of the samples to the E-chips.

4.3 Cryo-EM

During this process, it was revealed that TEM on electrodeposited Li could be successfully performed using cryogenic electron microscopy (cryo-EM) [92, 96]. This technique, originally developed for sensitive biological samples, allows the investigation of samples that would otherwise not be stable at room temperature under high vacuum and irradiation by high energy electron beams [92]. In cryo-EM, both the sample preparation and imaging occurs at cryogenic temperatures. Li et al. [92] electrodeposited Li onto a Cu TEM grid from a conventional liquid electrolyte (1 M LiPF_6 in 1:1 ethylene carbonate / diethyl carbonate), then transferred the Li in a sealed microcentrifuge tube with Ar into LN_2 (Li does not react with LN_2). The Li was then moved to the TEM without air exposure, and the authors successfully examined its microstructure using cryo-EM. However, the transfer of

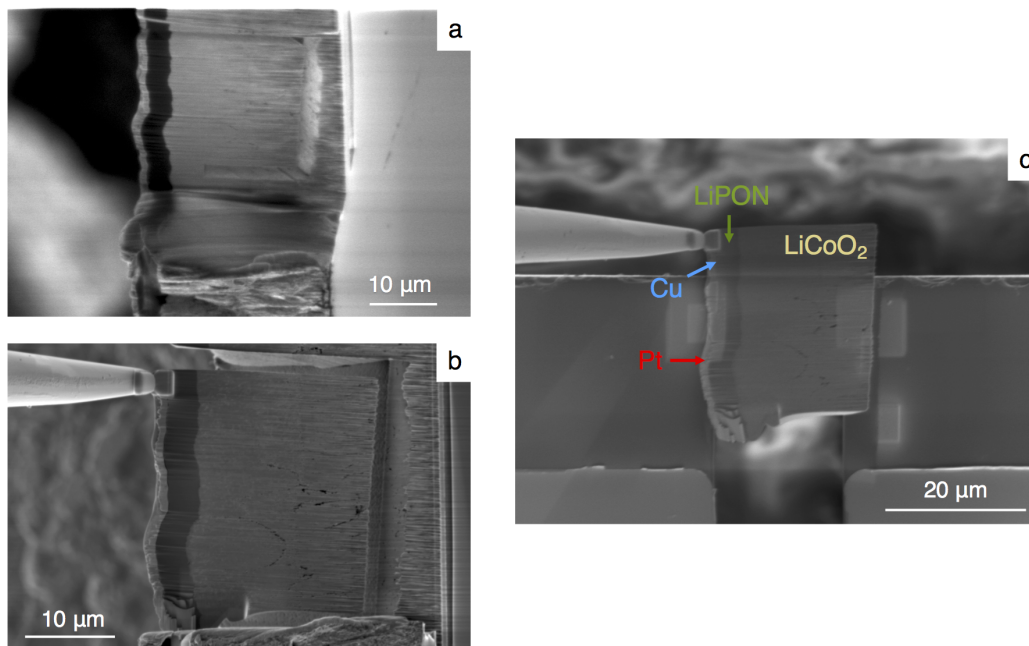


Figure 4.3: (a) View of sample being lifted out at a 90° orientation in the FIB. (b) View of the sample at the same location with the SEM. Note the large angle in between the two images; the sample must be at the very top edge of the SEM stage to view both the SEM and FIB. (c) Sample laid down at the edge of an E-chip. The Au electrodes are located at the bottom of the image. Part of the sample must lie off the edge of the E-chip in order for some Li to be grown over vacuum in the TEM.

Li grown in a solid-state cell is more problematic because effective solid-to-solid contact between a TEM grid and a solid electrolyte is more difficult than contact with a liquid electrolyte.

The first, simple attempt to transfer the Li grown out of the solid-state thin film cells was to gently scrape a carbon coated TEM grid on the cell after charging in the glovebox, carbon side down. In the cryo-EM (FEI Talos Arctica), some single crystalline particles were seen on the grid that did not resemble the Li electrodeposited from the cells. To directly observe and attach the Li to a TEM grid, FIB lift out can be performed. However, because of the reactivity of Li metal, the samples need to be transferred into and out of the FIB without air exposure. Similar to the operation of cryo-EM, a cryogenic focused ion beam (cryo-FIB) process can be performed to transfer the Li samples while remaining entirely under Ar, LN₂, or vacuum. The cell is charged in the glovebox, then taped on top of Kapton tape (to prevent short circuiting) onto the cryo-FIB transfer shuttle, shown in Figure 4.4(a). Ag epoxy is applied to Cu tape attached to the top of the cell to electrically connect

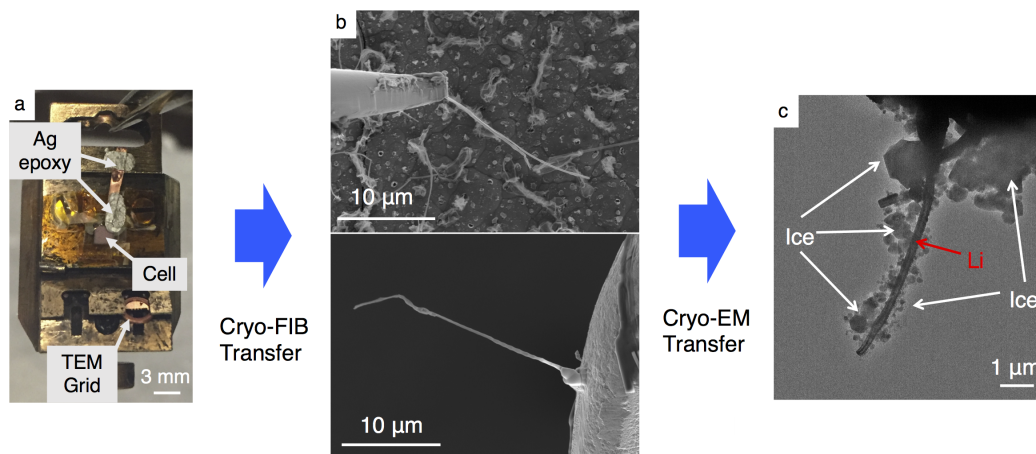


Figure 4.4: (a) Image of the cryo-FIB transfer shuttle with the cell and TEM grid attached. The top of the cell is electrically connected to the shuttle with Ag epoxy to mitigate drifting in the SEM/FIB. (b) A Li fiber lifted off the top of the cell with the nanoprobe (top). The fiber is then moved to the TEM grid and attached with IBID/EBID Pt (bottom). (c) A similar Li fiber seen in the cryo-EM surrounded by ice crystals. The ice forms at the air / LN₂ interface.

the cell to the shuttle to mitigate drifting in the SEM/FIB. The shuttle is sealed under Ar in a polyethylene vial and polypropylene container (for extra protection) and brought to the microscope, where the vial is opened under LN₂. The cryo-FIB transfer procedure directly transfers the shuttle from LN₂ to vacuum, where it is then transferred into the microscope chamber. Because cryogenic temperatures are only needed for transfer, all procedures performed in the chamber are at room temperature. At cryogenic temperatures, it would be difficult to apply beam-deposited Pt and there would be a large temperature gradient with the non-cooled nanoprobe, so special equipment would be needed in addition to the cryo-FIB equipment [100].

Individual Li fibers are located in the SEM and attached to the nanoprobe using deposited Pt. The bottom of the fibers attached to the cell are milled away by the FIB to lift out and attach them to posts of a TEM lift out semicircle grid (Figure 4.4(b)). The sample is then cooled down to -170 °C and removed under vacuum and LN₂, where it remains until transferred into the cryo EM. Unfortunately, many fibers that were attached to the grid were lost before the samples reached the TEM, probably from the transfer into LN₂ or from handling the grid with tweezers. Figure 4.4(c) shows that the Li fibers seen in the TEM were covered in many ice crystals and did not show a diffraction pattern; ice is commonly seen during cryo-EM, but the fibers displayed an excessive amount of crystals. The lack of a supporting film

on the grid may have concentrated the ice crystals. Many of cells used for cryo-FIB self-discharged, where most of the Li was stripped from the surface of the cell before the sample could be moved into the FIB. This limited the amount and quality of Li fibers that could be lifted out from the cell.

We eventually discovered that a much simpler method is an effective approach to transfer Li from the solid-state cell to the cryo-EM. To transfer the Li, the cell is taped to a stainless steel disc in the glovebox (Figure 4.5 (a, i)). A 3mm Cu TEM grid with a carbon support film is placed on the surface of the cell, carbon side down, as shown in Figure 4.5 (a, ii)), and a 15.9 mm diameter polydimethylsiloxane (PDMS) disc is placed on top of the grid (Figure 4.5 (a, iii)). Binder clips are clamped around the whole assembly to apply stress to improve the contact between the grid and cell (Figure 4.5 (b)). The PDMS is used to distribute the stress and to help improve contact between the cell and grid. The cell was then charged at 4.1 V for 20 minutes to plate Li out of the surface of the cell and onto the grid. After charging, the grid was placed in a polytetrafluoroethylene (PTFE)-sealed microcentrifuge tube. The tube was placed in two polypropylene containers, one sealed with parafin film, and an Al heat seal bag, all to protect the sample from atmosphere during transfer from the glovebox to LN₂. All containers were baked under vacuum at 80 °C for 5 hours before introduction into the glovebox. At the TEM facility (IMRI), the tube was quickly placed into LN₂ and once cool, the tube was opened with tweezers under LN₂ and the grid was removed. The grid was moved under LN₂ into the TEM holder and was transferred into the LN₂-cooled TEM (JEOL JEM-2100F TEM, 200 kV) in ~1 second. The grid was immersed under LN₂ for about 10 minutes in total. Bright field (BF) and selected area electron diffraction (SAED) images were obtained using an electron dose of $\sim 4 \text{ e } \text{Å}^{-2} \text{ s}^{-1}$.

4.4 Microstructure of Electrodeposited Li via Cryo-EM

Figure 4 shows TEM analysis and an SAED pattern of a representative 436 nm diameter Li pillar. This SAED pattern in Figure 4.6(b) corresponds to a body-centered cubic (bcc) crystal structure with a [311] zone axis (see the overlaid standard diffraction pattern in black); the experimental and standard patterns are in good agreement, with a slight discrepancy attributable to small misalignments from the exact Bragg condition. The SAED diffraction spots that do not correspond with Li arose from a non-Li crystal on the fiber surface (see the small black spot on Figure 4.6(a)). The pillar contains lines, likely surface features (see Figure 3.1(c)) parallel to the pillar axis and some fibers are kinked (see Figure 4.7). The measured lattice

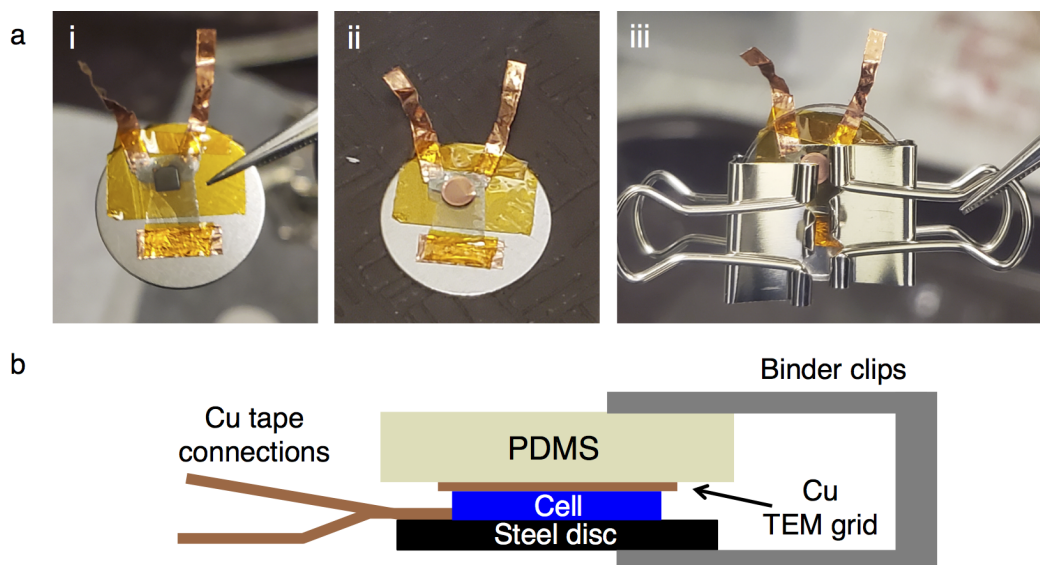


Figure 4.5: (a) Top view of the cell assembly to transfer Li to a TEM grid. (i) The cell mounted to a stainless steel disc. (ii) A Cu TEM grid with a carbon support film placed on the surface of the cell. (iii) The whole assembly with the PDMS disc and binder clips around the the entire stack. (b) Side view schematic of the assembly.

parameter from the SAED pattern is 3.47 \AA , which is close to the lattice parameter of Li (3.49 \AA) at $\sim 110 \text{ K}$ [101]. Figure 4.6(c) shows a high-resolution image of the crystal with parallel lattice planes, spaced at 2.4 \AA , which is (within the error of the measurement) consistent with the $\{110\}$ interplanar in Li, 2.47 \AA .

The morphology of electrodeposited Li grown from a SE into a vacuum here led to similar observations as in the cryo-EM liquid electrolyte study [92]: faceted single crystalline Li fibers of 200-700 nm diameters with occasional kinks (cf. Figure 4.7 and Figure 4 in [92]). In a liquid electrolyte cell, Li ions are supplied to the electrode surface through an SEI layer and reduced at the electrode/SEI interface to form Li metal. In our solid-state battery, Li ions are reduced at the LiPON/electrode interface directly to leave a pristine Li metal surface, yet both deposition methods produce similar morphologies. The $\{110\}$ planes are the planes with the lowest surface energy in Li [102], so a single crystal with a large surface area of $\{110\}$ planes can approach the minimum overall energy state. The lack of SEI allows the pristine Li surface to be exposed and form a faceted single crystal.

The grid-on-cell method to transfer the Li into the TEM in this work only allowed the fiber or pillar-like Li to be observed, likely because most of the sphere-like Li grew near the topographical minima and were not in contact with the grid. We expect

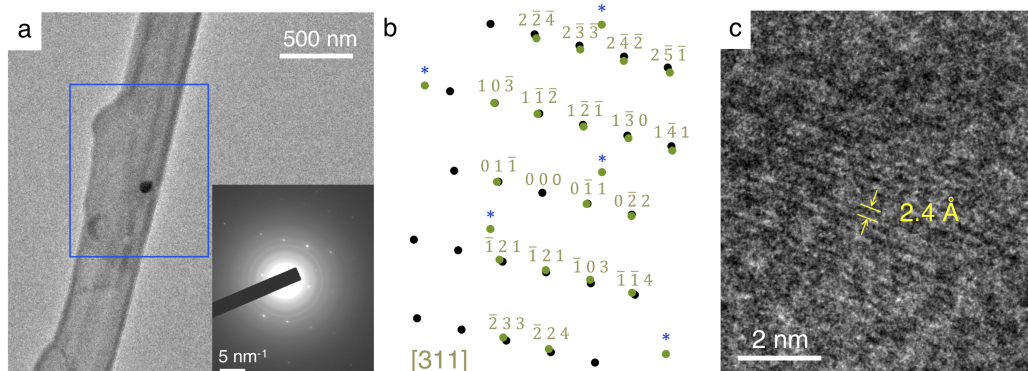


Figure 4.6: (a) BF image of a representative electrodeposited Li pillar (436 nm diameter) showing surface striations and a dark crystal. Inset shows the corresponding SAED pattern collected from the rectangle on the BF image along a $[311]$ zone axis. (b) Measured SAED pattern (green) overlaid on the standard diffraction pattern for bcc crystal taken along a $[311]$ zone axis (black). Blue *s refer to diffraction from the dark non-Li crystal on the fiber. (c) High-resolution TEM image that shows lattice fringes with a spacing of 2.4 \AA that corresponds to the distance between $\{110\}$ planes in Li. The relatively strong background of the carbon film and bending of the fiber prevent the observation of more fringes.

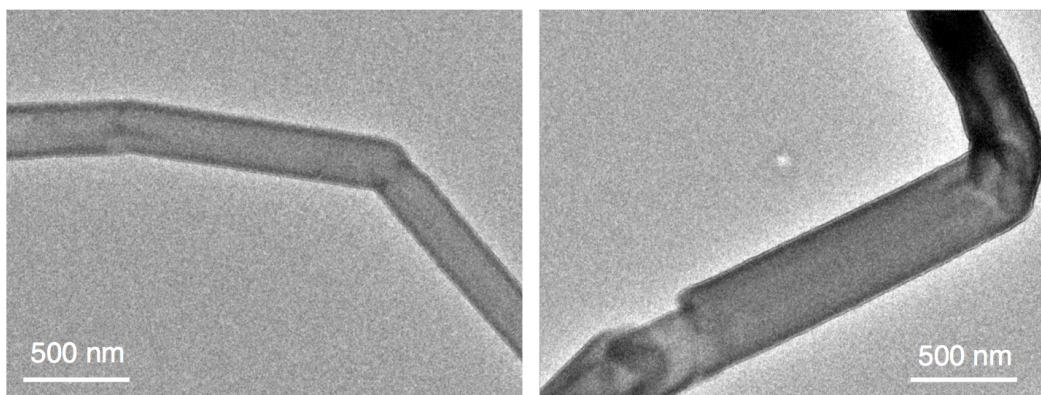


Figure 4.7: BF images of two kinked Li fibers viewed in the TEM. The diameters in the middle of the images are 263 nm (left) and 423 nm (right).

the sphere-like Li to be polycrystalline, as a sphere would not allow a single crystal to minimize its surface energy. The Li in the TEM was charged potentiostatically and the Li used for nanomechanical experiments was charged galvanostatically; the same morphologies were observed in the SEM for both constant potential and current charging. Potentiostatic charging increased the probability of successful Li transfer to the grid.

4.5 Summary and Conclusions

In-situ TEM was investigated as a method to introduce Li metal into the TEM chamber without air exposure. To also prevent beam sensitivity issues with Li, cryo-EM was ultimately utilized to successfully probe the microstructure of Li electrodeposited through a solid electrolyte. The Li was transferred into the TEM by charging the cell in contact with a TEM grid with pressure applied by binder clips. The microstructure of Li fibers was determined to be single crystalline, similar to that discovered in cryo-EM of Li deposited in conventional liquid electrolytes.

MECHANICAL PROPERTIES OF LI ELECTRODEPOSITED THROUGH A SOLID ELECTROLYTE

Adapted from

1. Citrin, M. A., Yang, H., Nieh, S. K., Berry, J., Gao, W., Pan, X., Srolovitz, D. J., & Greer, J. R. From Ion-to-Atom-to-Dendrite: Formation and Nanomechanical Behavior of Electrodeposited Lithium. (*In preparation*).

The previous chapters examined the formation and microstructure of Li electrodeposited from thin film solid-state cell. Once the Li is formed in the SEM chamber, mechanical experiments can be performed on individual Li deposits. This chapter will address the mechanical response of these samples and its context within the framework small scale plasticity.

5.1 Young's Modulus and Strength

A small fraction of the Li pillars that grew from the thin film solid-state cells (fewer than 1 in 5,000 Li deposits) had aspect ratios of 3:1 – 5:1 and were oriented perpendicular to the substrate. These pillars were amenable to *in-situ* uniaxial compression experiments. Figure 5.1(a) shows successive SEM images of a typical pillar compression experiment for a 520 nm diameter, 2.26 μm tall pillar tested at a nominal strain rate of $\sim 1 \times 10^{-3} \text{ s}^{-1}$. The load-displacement data for tests conducted at a prescribed (fixed) loading rate consistently showed less noise than those at a prescribed fixed displacement (strain) rate (Figure 5.2). The engineering stress-strain data (stress obtained by dividing the load by the initial area, assuming a circular cross-section, and the displacement by the initial length) and the dynamic contact stiffness (the instantaneous contact stiffness between the pillar and indenter tip), are shown in Figure 5.1(b, c, d).

The stress-strain data reveal that the pillars first deformed elastically, yielded at a strain of 1-3% (point 2 in 5.1(b)), and hardened at a near constant rate of 170 MPa. The yield strength (measured as the highest stress prior to the 0.2% strain offset line — see 5.1(c) inset) from this measurement was $\sigma_y = 21.7 \text{ MPa}$. The stress-strain

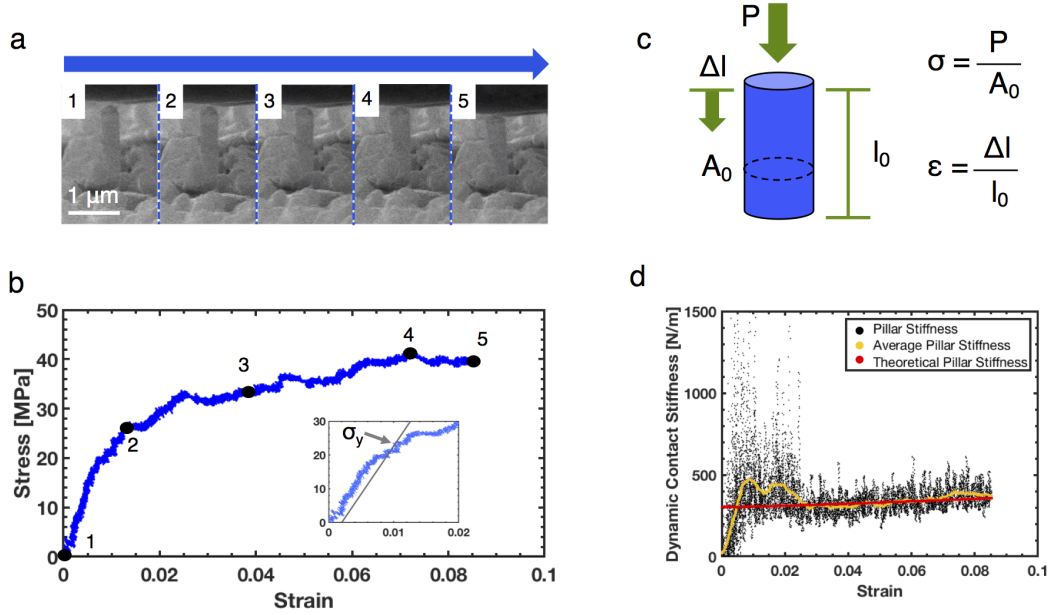


Figure 5.1: (a) SEM images during a uniaxial compression experiment on a 520 nm diameter, 2.26 μm -tall electrodeposited Li pillar at an effective strain rate of $1 \times 10^{-3} \text{ s}^{-1}$. The numbers in (a) correspond to the strains in the stress-strain curve in (b). Inset shows the determination of the 0.2% strain offset yield stress. (c) A sketch of a pillar with input variables defined to calculate engineering stress and strain. (d) The dynamic stiffness vs. engineering strain measured by CSM. The yellow curve is a running average of the raw data over 0.005 strain. A video of this experiment is shown as Supplementary Video 1.

curve during elastic deformation was commonly noisy, with occasional short strain bursts 0.3% – see Figure 5.3. Upon loading beyond 9% strain, the contact stiffness increased to 426 N/m, attributable to the indenter tip contacting other (out-of-view) Li deposits.

Uniaxial compression experiments were performed on 11 pillars with diameters between 360 nm and 759 nm. We used dynamic contact stiffness between the indenter tip and the pillar using CSM to determine the Young's modulus, E . CSM measures $k_{measured}$, the dynamic contact stiffness between the Li pillar and the indenter tip, which relates to the elastic modulus by:

$$E = k_{measured} \frac{L_p}{A_p} \quad (5.1)$$

where L_p is the instantaneous length and A_p is the instantaneous area of the pillar. L_p is calculated from the CSM data of the pillar with an initial length of L_0 and

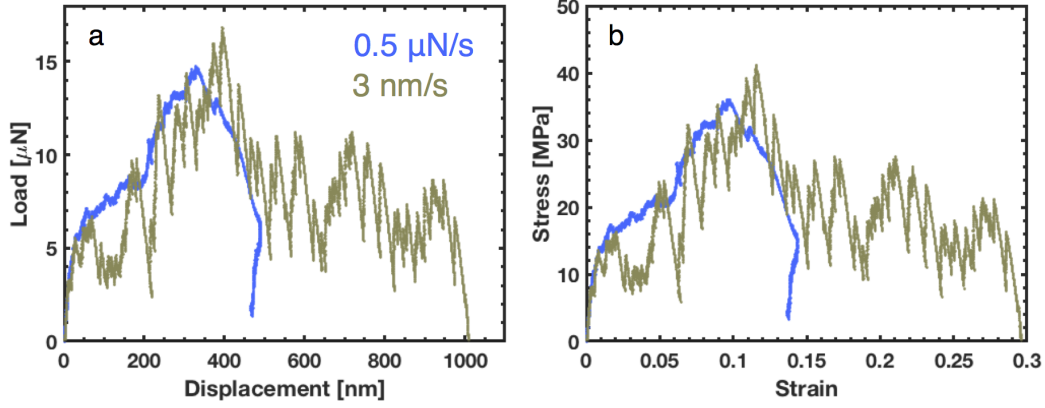


Figure 5.2: (a) Load vs. depth and (b) stress vs. strain for a representative pillar with a diameter of 520 nm at a prescribed constant load-rate of 0.5 $\mu\text{N/s}$ compared with a representative pillar with a diameter of 721 nm at a prescribed constant displacement rate of 3 nm/s (0.0015 s^{-1}). The noise in the data is much greater with the prescribed constant displacement rate.

circular cross-sectional area using:

$$L_p = L_0 - \left(u_{tot} - \frac{P}{k_{measured}} \right) \quad (5.2)$$

where u_{tot} is the total displacement measured by the indenter and P is the applied load.

With an assumption of volume conservation during deformation [50], A_p can be calculated as:

$$A_p = \frac{A_0 L_0}{L_p} \quad (5.3)$$

The modulus is then calculated as:

$$E_{Li} = \left(\frac{1}{k_{measured}} - C_{Sneddon} \right)^{-1} \frac{L_p^2}{A_0 L_0} \quad (5.4)$$

where $C_{Sneddon}$ is the contact compliance of a cylindrical punch into an elastic half-space. Further details can be found in Reference [103] and section 5.2.

To calculate the theoretical dynamic stiffness of the pillar, a similar approach is taken in the reverse direction, with the modulus as an input and the dynamic stiffness as an output. The instantaneous length of the pillar can be calculated as:

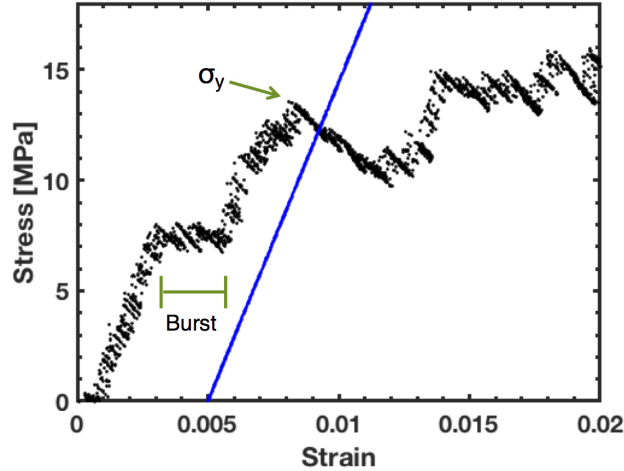


Figure 5.3: Example of a strain burst on the order of 0.3% strain being added to the strain offset to determine yield stress for a Li pillar.

$$L_p = \frac{EA_0L_0}{2P} \left(1 - \sqrt{1 - 4\frac{P}{EA_0L_0}(L_0 - u_{tot})}\right) \quad (5.5)$$

The theoretical stiffness is then simply calculated as:

$$k_{theoretical} = \frac{EA_0L_0}{L_p^2} \quad (5.6)$$

Further details can be found in Reference [50]. Due to the large noise in the CSM data, a suitable part of the dynamic stiffness needs to be chosen for the elastic modulus calculation. This region is after the pillar is in full contact with the indenter tip and the dynamic stiffness is relatively flat. The theoretical stiffness is used to check where the pillar deviates from the expected stiffness. The theoretical and measured stiffnesses will match in the region chosen for the modulus calculations because the inputs of the theoretical stiffness include the modulus calculated from the measured dynamic stiffness. A region between 50 and 150 nm is chosen and an average value is used with a low-pass filter to remove a few extraneously large stiffness data points. The CSM data produced moduli of 6.76 ± 2.88 GPa (\pm is the standard deviation).

Using the data from all 11 samples, we find a yield strength of $\sigma_y = 16.0 \pm 6.82$ MPa, a maximum compressive stress of 43.2 ± 17.0 MPa (the largest measured stress was 69.4 MPa — likely an overestimate because of contact of the indenter tip with other Li particles), and a hardening slope of 410 ± 251 MPa. We did

not find any systematic relationship between the yield stress and pillar diameter. SEM micrographs of the post-mortem pillar morphology did not reveal clear slip offsets such as those observed in other uniaxial compression tests of FIB-carved metallic samples [40, 43, 52, 103]; all pillars showed widening of the pillar tops during deformation in a barreling or extrusion-like manner, more similar to the deformation of other low- T_m metals [104, 105]. Videos of the deformation process (Supplementary Video 1-3, all as 10x speed) demonstrate that these stress-strain signatures were consistent across all samples, with some increase in stress after yielding and attaining a maximum load at strains of 10-15%. The deformation of all samples was relatively homogeneous (no visible slip offsets) with localized plastic deformation towards the top half of the samples.

5.2 Mechanical Response in Context

The size and the geometry of the Li nano-pillars that form during electrochemical charging in this work were small compared with those commonly used for uniaxial nanomechanical experiments, i.e., 0.2-5 μm [40, 49–51, 53, 54, 104]. The cylindrical pillar geometry and uniaxial deformation geometry allowed simple calculation of engineering stress and strain, represented in Fig. 5(c), from the measured load P and uniaxial length change, Δl : $\sigma_{eng} = p/A_0$ and $\varepsilon_{eng} = \Delta l/l_0$. In the last decade, the majority of such nanomechanical experiments have been performed on cylindrical pillars carved from a film or a bulk material using the FIB (a subtractive process) [43]. Such experiments and simulations show a “smaller is stronger” effect, often described by Equation 1.4.

Uniaxial compression experiments on individual nanostructures fabricated without the use of the FIB are relatively uncommon and have material limitations, e.g. electrodeposition into molds (Au [50], Cu [51]), catalyst-controlled vapor deposition (ZnO [106]), and directional solidification (Mo alloys [44]). The mechanical properties and deformation of these types of samples appear to be dependent on fabrication method and do not always exhibit a size effect. For example, the pristine, directionally solidified single crystalline Mo fibers exhibited theoretical strength with no dependence on size [44], while single crystalline Cu pillars electroplated into a template show the same size scaling as FIB-milled single crystalline fcc pillars [51]. A common signature of uniaxial compression experiments on single crystal metallic micro- and nano-pillars fabricated using both subtractive and additive techniques is the presence of multiple rapid, stochastic strain bursts in the stress-strain response (corresponding to the operation of discrete dislocation sources that pro-

duce dislocation avalanches over a strain of $\sim 1\text{-}5\%$ with a power law distribution [107, 108]).

The stress-strain compression data in this work (Figure 5.1) appears to be smoother and contains fewer abrupt strain bursts characteristic of the deformation of FIB-fabricated single crystalline Li micro-pillars (e.g., see Figure 1 in [40] and other bcc pillars of similar diameters [53]). The discrete events in our experiments occurred over seconds, 3-4 orders of magnitude slower than the typical fast strain bursts in FIB-milled samples [43]. This slower time scale suggests that the deformation mechanism in the electrodeposited Li pillars may be associated with thermally activated processes (e.g., surface reconstruction, dislocation climb, dislocation cross-slip, and/or Nabarro-Herring creep-like deformation [64, 69]) rather than rapid dislocation avalanches. We also discovered that the load-displacement data contained substantial high-frequency background noise and oscillations (Supplementary Videos 1-3) that probably stem from the ungrounded indenter tip and the very small applied loads, on the order of $10\ \mu\text{N}$, which required extra precautions when analyzing and interpreting the data.

For example, the compression experiment videos (Supplementary Videos 1-3) show stochastic lateral motion of the indenter tip during compression on the time scale of seconds for all samples. This is likely due to an electrostatic effect caused by the connection of the cell to the potentiostat during mechanical compression, and has a negligible effect on the mechanical data. The motion does not correlate with any mechanical response and was not visible on any other sample in our instrument, none of which had an electrical connection outside the chamber (Supplementary Videos 1, 2). Besides these general common characteristics, some samples underwent minor strain excursions, an example of which can be seen at 4% strain in Figure 5.4 for the $622\ \text{nm}$ diameter sample.

While all experiments were performed under a nominal strain rate of $\sim 1 \times 10^{-3}$ (see Figure 2.6), our experiments revealed that the load-displacement data for tests conducted under a prescribed fixed loading rate consistently showed less noise than those at a prescribed fixed displacement (strain) rate. The latter contained large fluctuations in load, usually between 1 and $5\ \mu\text{N}$, that do not correlate with the corresponding mechanical response (Supplementary Video 3) and that were likely caused by an extra feedback loop in the indenter system, which is inherently load controlled (Figure 5.2). Beyond these load fluctuations in the post-yield, the general signature of the mechanical behavior, as well as the elastic modulus and the yield

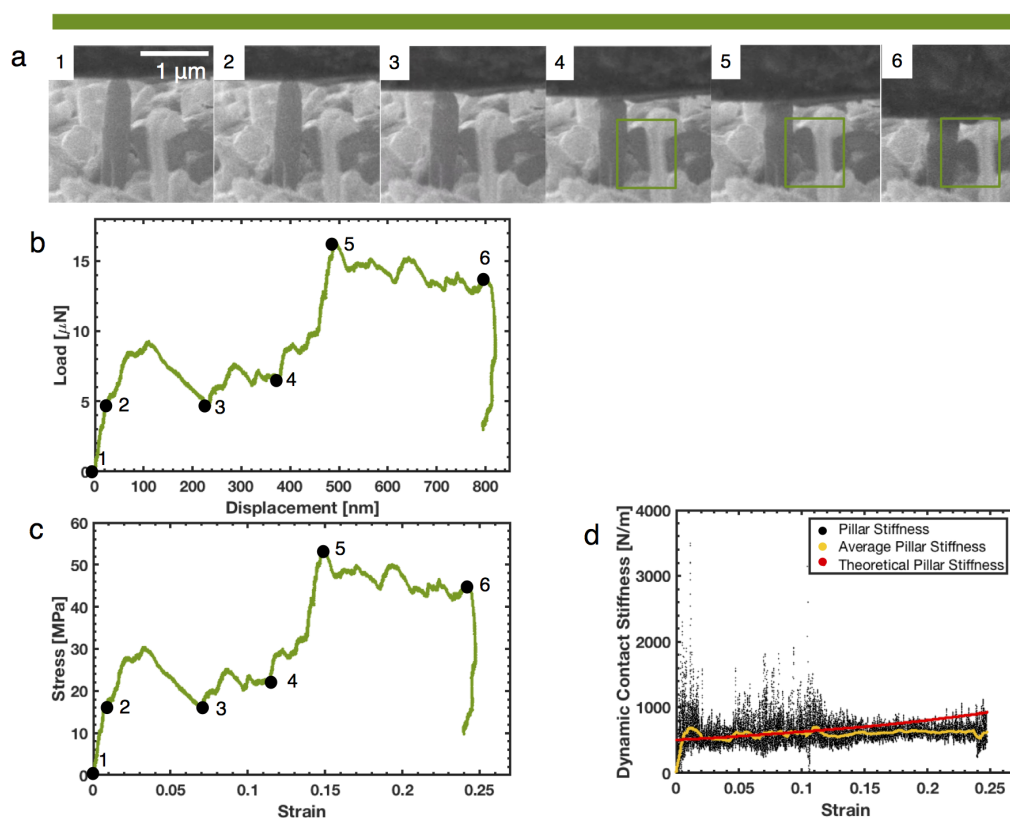


Figure 5.4: (a) SEM snapshots during a uniaxial compression experiment at an effective strain rate of $1 \times 10^{-3} \text{ s}^{-1}$ on a 622 nm diameter, 2.42 μm tall electrodeposited Li pillar. The green box shows the Li particle that starts to contact the pillar at point 4. The number in the top left corner of each image corresponds to the displacements (b) and strains (c) indicated in the load vs. displacement and engineering stress vs. engineering strain curve, respectively. The inset shows the location of the 0.2% strain offset yield stress. (d) The dynamic stiffness vs. engineering strain measured using CSM. The yellow curve is a running average of the raw data over 0.005 strain.

strength, under these two different loading conditions is very similar.

We have observed the tip touching a thin Li fiber bent at roughly 60° . The tip still has the lateral motion while the indenter bends the Li fiber further down, but negligible load is measured until the tip contacts a vertically oriented Li pillar, which is expected (Figure 5.5). The tip does not move in this manner when it is not in contact with the sample; the lateral movement of the tip does not correspond to any feature of the mechanical data. We therefore believe this movement has an insignificant effect on the mechanical response.

We measured the moduli using CSM because the extent of plastic deformation in the electrodeposited Li pillars renders the unloading slope inappropriate for

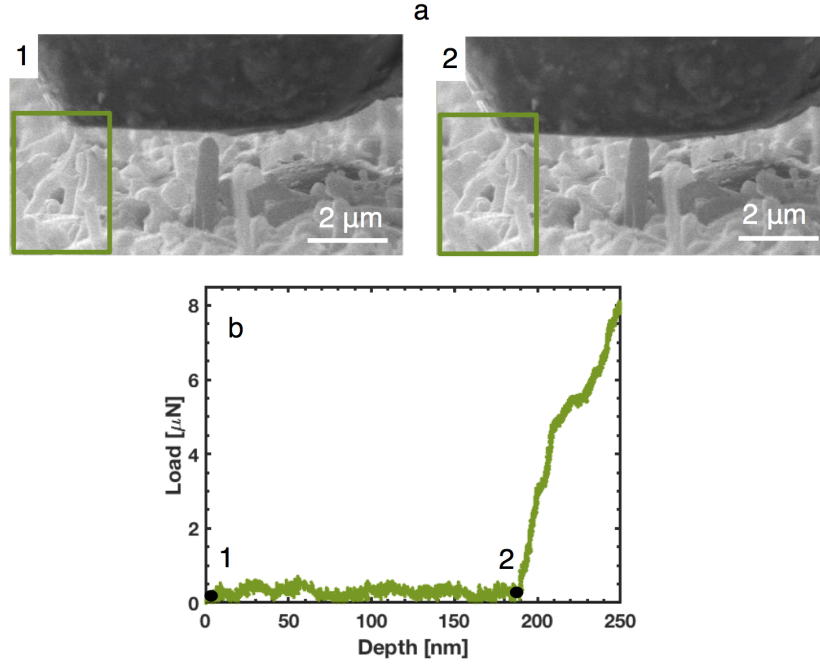


Figure 5.5: (a) The indenter tip touching a thin Li fiber at an angle, denoted by the green box at the left side of the indenter tip. (b) The corresponding points on the load-displacement curve. The load is negligible before the pillar starts to be compressed right after point 2. Between points 1 and 2, lateral motion of the indenter tip is still observed.

determining the Young's modulus. Additional elastic compliances of the substrate were accounted for by treating the pillar as an elastic circular punch indenting into an elastic half space of LiPON [50]. Sneddon [109] first described the contact compliance, $C_{Sneddon}$, of this process as:

$$C_{Sneddon} = \frac{\sqrt{\pi}(1 - \nu^2)}{2E_{LiPON}\sqrt{A_p}} \quad (5.7)$$

where ν is the Poisson's ratio of Li (0.362 [73]) and A_p is the instantaneous plastic area of the pillar, which can be approximated as the initial area of the pillar A_0 . Since LiPON is an amorphous ceramic, it can be taken as elastically isotropic, so E_{LiPON} is the measured elastic modulus of LiPON, 77 GPa [110]. The Sneddon compliance is multiplied by the load and subtracted from the displacement. The Sneddon correction will slightly increase the measured stiffness and modulus of the material. This correction is small (< 2%) because the Young's modulus of LiPON is significantly higher than that of Li in all crystallographic orientations [40, 110].

The average measured Young's modulus of the single crystalline electroplated Li pillars was determined to be 6.76 ± 2.88 GPa, consistent with the 5.28 GPa reported for uniaxially compressed single crystalline (FIB milled) Li pillars [40] and 9.8 GPa measured via nanoindentation on single grains of thermally evaporated polycrystalline Li thin films [73], both in a variety of crystallographic orientations. The anisotropic Young's modulus of single crystalline Li varies from 3.00 GPa in the $\langle 100 \rangle$ direction to 21.2 GPa in the $\langle 111 \rangle$ direction [40, 111]; the large standard deviation in the measured elastic modulus (43%) is likely due this substantial elastic anisotropy of Li and from the noise in dynamic contact stiffness data at the μN loads (Figure 5.1(c)).

Unlike the modulus, which is largely microstructure and size-independent, post-yield deformation and mechanical properties of metals are a strong function of microstructure: crystal structure, grain size, dislocation density, porosity, impurity concentration, etc. The measured yield stresses of electrodeposited Li varied from 4.99 MPa (729 nm diameter pillar) to 26.0 MPa (622 nm diameter pillar). These values are on average $24\times$ larger than the 0.66 MPa reported for bulk polycrystalline Li; with the strongest pillar in this work being $39\times$ stronger [56, 66, 69–71]. We determined the out-of-plane crystallographic orientations of each sample using the modulus calculated from CSM data, and used them to calculate the resolved strengths as:

$$\tau_{Res} = \sigma_y \cos \phi \cos \lambda \quad (5.8)$$

where τ_{res} is the strength resolved onto the $\{110\}\langle 111 \rangle$ slip system, σ_y is the yield stress, ϕ is the angle between σ_y and the normal to the slip plane, and λ is the angle between σ_y and the slip direction. Table 5.1 contains the results of these calculations.

The calculations revealed the average resolved shear strength to be 6.95 ± 2.82 MPa. This $\sim 41\%$ standard deviation in strength cannot be explained by the elastic anisotropy of Li. Some factors that could contribute to this broad range of strengths include differences in sample morphology driven by the kinetics of electrodeposition, variations in defect density and distribution, surface energy state and flaw distribution, the low homologous temperature (T/T_m , T_m = melting temperature) of Li during room temperature experiments, and variations in the cross-sectional geometry, which could substantially change the measured stress.

Diameter (nm)	Modulus (GPa)	Orientation	Schmid Factor ($\cos \phi \cos \lambda$)	Yield Strength (MPa)	Resolved Strength (MPa)
709	4.88	<311>	0.445	6.38	2.84
613	11.3	<221>	0.408	10.94	4.47
515	3.41	<410>	0.480	14.54	6.98
546	9.15	<110>	0.408	24.8	10.12
759	6.94	<320>	0.471	17.5	8.24
729	8.23	<110>	0.471	4.99	2.04
721	5.06	<311>	0.408	13.5	6.01
678	11.3	<221>	0.408	26.0	10.61
622	4.92	<311>	0.445	18.0	8.02
520	3.27	<100>	0.408	21.7	8.86
359	5.92	<421>	0.486	17.1	8.31

Table 5.1: Mechanical data for all pillar samples. The orientation is estimated using the measured modulus and is used to calculate the Schmid factor and resolved strength, as shown in 5.8.

When calculating the area to convert force to stress, we measure the diameter of the pillars in the SEM and convert to area assuming a circular cross-section. However, it is possible that the pillars do not have circular cross-sections due to any faceting on the pillars. The faceted Li fibers seen in cryo-SEM by Li et al. [92] are triangular, hexagonal, and rectangular with a 2:1 aspect ratio. Using these geometries, the difference in cross-sectional area can be calculated by assuming a constant diameter, defined as the largest distance perpendicular to the electron beam. Figure 5.6 demonstrates the largest and smallest area for each cross-sectional geometry. Only the large aspect ratio rectangular cross-section shows a large (>30%) difference in area, but in our images, we did not observe these geometries. We only observed close to circular or triangular cross-sections, and thus the effect of cross-sectional geometry is < 30%.

Such a non-negligible spread in yield strength is not uncommon in small-scale pillar experiments because they are susceptible to common small experimental artifacts,

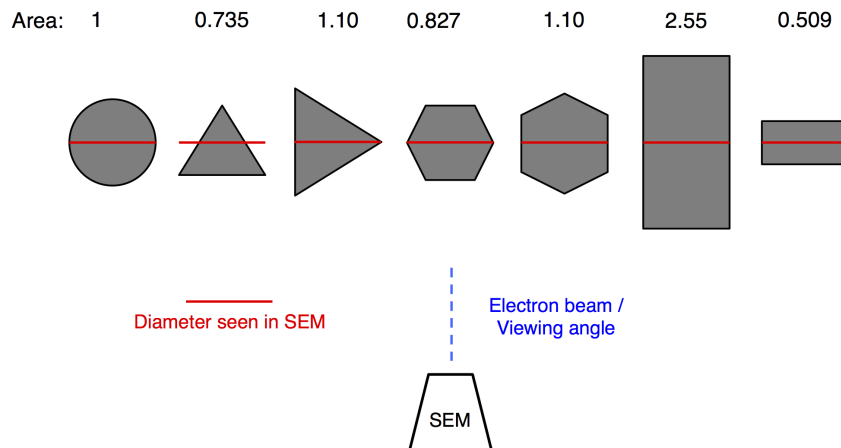


Figure 5.6: Possible Li cross-sections, shown with a constant diameter in red. All areas are normalized to a circle of unit area.

like small misalignments between the indenter tip and the sample, differences in microstructure and defect content among samples, and the stochastic nature of their deformation, all of which would be negligible in similar macroscopic experiments [112, 113]. The large standard deviation in strength in slightly pre-strained Mo pillars of 37%, for instance, was attributed to a spatially inhomogeneous dislocation distribution [114]. In a similar material to Li, 560 nm diameter electroplated-into-template In pillars, containing at most a few grains and whose homologous temperature of 0.69 at 298 K is close to that of Li, had a similar relative standard deviation in their average yield strength: 40.8 ± 18.5 MPa [104].

All small-scale single-crystalline Li samples — regardless of size and fabrication route and testing techniques — consistently exhibit strengths that are a factor of about 10 to 100x higher than what has been reported for bulk polycrystalline Li [40, 64, 65]. The yield strength of FIB-milled 1 μm diameter Li pillars was reported to be 105 MPa and decreased in a power law fashion as $\sigma \sim D^{-0.68}$ for larger samples [40]. The enhanced strength can be explained in the framework of dislocation starvation, where mobile dislocations are annihilated at the surface during deformation and dislocations are nucleated at single-arm sources or surfaces [40, 43]. The yield stresses of electrodeposited Li in this work are over an order of magnitude lower than those reported for the FIB-carved single-crystalline Li pillars. The -0.68 power law scaling would predict the ~ 700 nm diameter electroplated pillars in this work to yield at ~ 240 MPa, which is 15x larger than the measured ~ 16 MPa. Nanoindentation into 5-18 μm thick thermally evaporated Li films with a Berkovich tip revealed a peak of 40 MPa in the average hardness at an indentation depth of 360 nm, which decreased

to 22 MPa at 1 μm under a load rate of $\dot{P}/P = 0.05 \text{ s}^{-1}$ [64, 65, 73]. The authors attributed the peak in hardness to a transition from diffusion-mediated to dislocation-mediated plastic flow. This peak hardness obtained using nanoindentation at a depth of $\sim 360 \text{ nm}$ is 2.5x higher than the average yield stress measured for the electroplated Li pillars (360-759 nm diameter), a difference similar to the Tabor factor. The deforming volume, which ranges from 0.18 to 1.4 μm^3 for the pillars and $\sim 1 \mu\text{m}^3$ at 360 nm depth for nanoindentation, is also similar in both cases.

The plot in Fig. 7 places the yield stresses of the single crystalline electrodeposited Li nano-pillars into the strength vs. size parameter space for Li and reveals three key observations: (1) no obvious size effect over the range of diameters studied, (2) 24x higher strengths than bulk [56, 66, 69–71] and a factor of 16 lower than the theoretical tensile strength of Li, ($\sigma_{<100>,theo}^{Li} = 253 \text{ MPa}$ [115]), and (3) similar strengths observed between the electrodeposited pillars and single grains within Li thin films probed via nanoindentation at similar deforming volumes, over an order of magnitude lower than the strengths of FIB-produced Li pillars at similar dimensions. These findings are in contrast to virtually every study on uniaxial compression of single crystalline metallic nano- and micro-pillars, which either reported the existence of a power law size effect (smaller is stronger for FIB-milled and electroplated samples [40, 43, 49–51, 53, 54, 103, 116]) or no size effect and close-to-theoretical strengths (for pristine nanopillars produced by directional solidification [44, 112]). Little control over the size and orientation of individual pillars, a limited range of sizes, and a dearth of samples oriented favorably for mechanical experiments after charging render this lack of size effect inconclusive. The larger pillars ($D = 678$ to 759 nm) had an average strength of 13.7 MPa and the smaller pillars ($D = 359$ to 622 nm) had an average strength of 17.8 MPa; these values are substantially below the theoretical strength of Li (253 MPa [115]), which suggests that the electrodeposited samples are not pristine nanowires despite the faceted morphology. The relatively high standard deviation is consistent with 37% observed in single crystalline directionally solidified Mo pillars over a similar dimensional range [114].

These profound differences in the compressive strengths of Li pillars with similar dimensions suggests that the electrochemical cycling conditions, the surface energy state, and/or the microstructure of the deposited materials may play a significant role on their mechanical response and robustness. One significant distinction among the three types of samples discussed above (FIB-milled, nanoindentation, electrodepo-

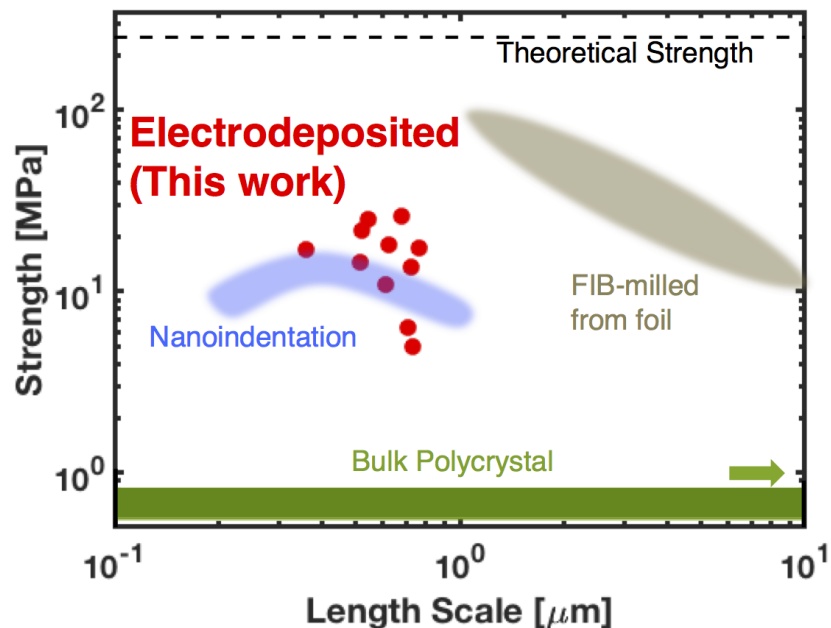


Figure 5.7: Parameter space for strength vs. size for Li of various form factors, dimensions, microstructures, and fabrication techniques. The gray region represents data for FIB-carved Li micro-pillars from [40]; the blue region represents the strengths estimated from nanoindentation under a load rate of $\dot{P}/P = 0.05 \text{ s}^{-1}$ from [64, 65] using the Tabor factor, and the green bar corresponds to the reported strengths of bulk polycrystalline Li based on [56, 66, 69–71]. The theoretical strength is taken from [115].

sition) is likely the atomic density and the energy state of the sample surfaces: the surfaces of the FIB-fabricated Li pillars were created by etching the surrounding material with high-energy (30kV) Ga^+ ions; such irradiation can elevate the surface energy by 0.014 eV per atom [117] and induce atomic arrangements on the surface into a far-from-equilibrium state [117, 118]. For example, a 2-3% increase in free volume at the surface due to Ga^+ FIB irradiation can induce ductility in nano-sized metallic glass structures [118, 119]. Ga also readily alloys with Li at room temperature [120], potentially passivating the surface of the pillar, which can prevent dislocation annihilation at free surfaces and cause an increase in yield strength by creating a barrier for plasticity [121]. At the homologous temperature of 0.66 at 298 K, some of this damage may have been recovered by room temperature annealing, which could suppress dislocation nucleation at the surfaces and is consistent with the observed size effect even at diameters close to $10 \mu\text{m}$ [40, 65, 86].

During nanoindentation, the volume of material probed is deformed inhomoge-

neously with large stress/strain gradients, potentially leading to larger plasticity at the very tip of the indenter vs. elsewhere in the deforming volume. There are no free surfaces around the deformed volume, in contrast to nanopillars, so dislocations cannot annihilate or nucleate at these surfaces [50]. The Li nano-pillars studied in this work were deposited electrochemically, by applying a bias and driving Li-ion transport from LCO through a solid LiPON electrolyte to the LiPON/Cu interface, where the ions reduced, and Li grew into high vacuum. The electrodeposition is unconstrained (without a template); this lack of lateral boundary conditions and ion bombardment (as in the FIB-milled case) results in a closer-to-equilibrium material microstructure - single crystalline samples with faceted morphology and thermodynamically-favored surface orientations. The kinetics of Li transport during growth leads to an overall more relaxed surface energy state and large variations in strength compared to a template-set geometry for all samples [51, 116]. The electroplated samples are particularly susceptible to morphological variations because electrodeposition is a kinetically-driven process, which leads to different surface energy states compared with ion-milled surfaces [118, 119].

5.3 Possible Strengthening Mechanisms

The electrodeposited Li pillars in this work have a close-to-equilibrium microstructure, with naturally formed faceted morphology and thermodynamically-favored surface orientations. The energy state of such surfaces is close to the lowest energy state, which can be 0.014 eV per atom lower than that of irradiated surfaces for the same material [117]. Theoretical computations by Zhu et al. [122] demonstrated that during deformation, the edges adjoining crystallographic facets serve as energetically favorable sites for partial dislocation nucleation during compression, which drives incipient plasticity in these types of nano-sized samples. Jennings et al. [123] built upon this theory and demonstrated through experiments and theory that the activation volume of $\sim 10b^3$ for surface dislocation source initiation in single crystalline Cu nano-pillars with 75 to 500 nm diameters electroplated into a poly(methyl methacrylate) (PMMA) template remains constant for all sample sizes, which may help explain the invariance of strength with size.

Jennings et al. [123] demonstrated this effect by investigating the strength of these Cu pillars as a function of their diameter and deformation strain rate and found that below a critical transition diameter, which scales with strain rate, the flow stress deviates from power law strengthening with further size reduction and becomes insensitive to size (see Figure 4 in [123]). For example, at a strain rate of 10^{-3} s^{-1} ,

this critical strengthening-to-constant strength transition diameter is ~ 150 nm and at a strain rate of 10^{-1} s^{-1} , it is ≤ 75 nm, which highlights thermal vs. athermal processes that contribute to deformation.

Below this transition diameter, the deformation mechanism was attributed to dislocation starvation followed by dislocation nucleation at the surface of the pillars to accommodate plasticity [123]. The implicit formulation of stress that accounts for thermal (strain rate, temperature) and athermal (collective dislocation dynamics, etc.) activation processes is:

$$\sigma = \sigma_a - \frac{k_B T}{\Omega} \ln \frac{k_B T N \nu_0}{E \dot{\epsilon} \Omega} \quad (5.9)$$

where σ is the most probable stress that a dislocation will nucleate, σ_a is the athermal strength, k_B is Boltzmann's constant, T is temperature, Ω is the activation volume, N is the number of equivalent surface nucleation sites, ν_0 is the attempt frequency, E is the elastic modulus, and $\dot{\epsilon}$ is the strain rate [123]. In this nucleation-governed regime, there is a strong temperature dependence, $T \ln T$, of the nucleation stress.

It is reasonable to estimate the critical temperature of Li, defined as the temperature above which the Peierls barrier becomes negligible, to be lower than room temperature, because it is commonly 0.1-0.2 T_m [52, 53]. One characteristic of bcc metals is that the mobilities of screw and edge dislocations below this temperature are distinct, with screw dislocations being $10\times$ slower than edges [124]; above the transition temperature, their mobilities become equal during plastic deformation, and the dislocations are able to easily move through the potential energy landscape [40, 52, 53] 21,34,62. Equation 5.9 indicates that dislocation sources are activated more easily at higher homologous temperatures, which implies that Li (bcc) has a greater transition length scale compared with Cu (at 298 K, $T/T_m = 0.22$) [123]. As a first approximation, the activation energy for surface dislocation nucleation scales with temperature as:

$$Q(\sigma, T) = (1 - T/T_d)Q_0(\sigma) \quad (5.10)$$

where $Q(\sigma, T)$ is the activation free energy for dislocation nucleation as a function of stress and temperature, T_d is the surface disordering temperature, and $Q_0(\sigma)$ is the activation energy on a zero-T potential energy landscape [122]. The surface disordering temperature scales with T_m [125]; if T_d is estimated as $0.75 T_m$ [125],

then $Q(\sigma, t)$ for surface dislocation nucleation in Li would be ~ 0.2 that of Cu for a given $Q_0(\sigma)$. The direct relation between activation energy and transition diameter is complex and would require uniaxial compression experiments at different diameters and strain rates to experimentally measure. As an example, if the transition diameter scales linearly with the activation energy, then the transition diameter for Li deformed at $\sim 10^{-3} \text{ s}^{-1}$ would be $\sim 750 \text{ nm}$, which would place almost all the electrochemically grown sub-micron-diameter Li nano-pillars in this work below the critical transition length scale (one sample had a 759 nm diameter) and lead to size-invariant strength [123]. This line of reasoning suggests that the most probable deformation mechanism of electrochemically grown Li nano-pillars is surface dislocation nucleation, which explains the lack of size effect in these samples and a strength between bulk Li and the micron sized FIB-carved pillars.

Even though the electrodeposited Li pillars contain pristine and thermodynamically-favored surfaces, their strength was over an order of magnitude lower than theoretical strength. This is likely due to defects / dislocations in the internal microstructure. Both faceted surfaces and a dislocation-free internal microstructure was needed to reach close to theoretical strength in Mo pillars [44, 112] and Cu whiskers [126], while heavy prestraining to induce dislocation formation was found to reduce strength about 10x [114]. Due to the kinetically-driven process of electrodeposition, the Li pillars in this work are unlikely to be defect-free [116, 127], especially with a stress of 0.1-1 GPa potentially being applied to the Li before it fractures through the Cu layer [72]. There may also be chemical impurities in the Li that prevent a pristine internal microstructure; chemical identification was not available in the *in-situ* SEM instrument or cryo-EM.

The lack of stochastic strain bursts and visible slip offsets in the deformed pillars, which are observed ubiquitously in nearly all nanomechanical experiments on micron- and sub-micron single crystalline metals, as well as the high homologous temperature of room-temperature experiments, suggests the operation of another deformation mechanism in electroplated Li pillars, in addition to dislocation glide. These include high-homologous temperature processes, i.e. creep-like deformation, such as dislocation climb and cross-slip [40, 104] and diffusive deformation in the bulk or at the surface [64]. The post-mortem morphology of electroplated Li pillars is similar to that of electroplated In (containing at most a few grains) [104] and single crystalline Sn [105] pillars, whose homologous temperatures at 298 K are also high (0.69 and 0.59, respectively), characterized by extrusion-like plastic flow with less

localized slip, the absence of any size effect (for In pillars), and a large scatter in strength. Similar homogenous deformation also describes the FIB carved Li pillars deformed at 363 K, whose yield strength of 35 MPa for 1 μm diameter samples is somewhat similar to that of the electrodeposited Li pillars in this work deformed at 298 K [40]. A transition from deformation dominated by glide to more creep-like deformation may explain the 5-26 MPa strength range of the electrodeposited Li.

These deformation processes are also a strong function of strain rate. The electrodeposited Li pillars were deformed at a slightly lower strain rate $\sim 1 \times 10^{-3} \text{ s}^{-1}$ than the FIB-carved pillars $5 \times 10^{-3} \text{ s}^{-1}$ [40]. Nanoindentation into evaporated Li films was performed at strain rates from $\dot{P}/P = 0.05 \text{ s}^{-1}$ to 1 s^{-1} , in addition to 12.5 $\mu\text{N/s}$; the maximum hardness revealed during indentation increased with strain rate, from 40 to 90 MPa [64, 65]. Because of the complicated strain gradients created by nanoindentation, it is difficult to obtain an equivalent uniaxial strain rate. Only the lowest strain rate (0.05 s^{-1}) was used to compare between all three small-scale Li mechanical experiments on Figure 5.7 due to the high strain rate sensitivity. Surface dislocation nucleation is also sensitive to strain rate, with larger strain rates decreasing the thermal contribution in Equation 5.9 to allow for larger stresses before a transition to surface dislocation nucleation-mediated deformation [123]. At the bulk scale, the flow stress of polycrystalline Li has been shown to increase from ~ 0.5 MPa to ~ 0.8 MPa by increasing the strain rate from $4 \times 10^{-5} \text{ s}^{-1}$ to $3 \times 10^{-3} \text{ s}^{-1}$ due to power-law creep [69]. Strain rate is a critical parameter to consider during battery performance as it is proportional to current density for a uniform layer or pillar of Li [69]. Altogether, the different deformation mechanisms for Li at different length scales are all sensitive to strain rate, re-emphasizing the importance of strain rate and current density to the mechanical response of Li during battery operation.

The peak strength of thermally evaporated Li thin films probed via nanoindentation at a load rate of $\dot{P}/P = 0.05 \text{ s}^{-1}$, estimated using the Tabor factor, is $\sim 83\%$ of the yield strength of the electrodeposited Li pillars at a similar deforming volume [64, 65, 73]. Thermally evaporated Li and electrodeposited Li have different microstructures, defect content, and dislocation densities due to differences in the deposition processes, but are both formed under kinetically driven conditions. They are more similar to one another compared with Li formed via melting and slow recrystallization, which is a closer-to-equilibrium process [127, 128]. Unlike the electrodeposited pillars examined here, the single crystal FIB-milled pillars were carved out of large individual grains formed from melting and slowly cooling to

room temperature. These pillars, in the diameter range of 1 – 10 μm , were never electrochemically cycled, never exposed to an electrolyte, and had uniform, smooth surfaces that were formed as a result of ionic bombardment. These factors may explain the similar strengths of the single crystalline electrodeposited and evaporated Li at a similar scale and their lower strengths compared to single crystalline submicron recrystallized FIB-carved Li pillars, even though they were mechanically probed under different applied strain fields.

5.4 Implications for Solid-State Batteries

This fundamental investigation into the formation, microstructure, and mechanical properties of electrodeposited Li has direct implications for Li metal-based electrochemical storage systems, and especially for solid-state Li batteries. The microstructure and length scale of the electrodeposited Li investigated in this work is similar to that encountered in solid-state batteries with a ceramic electrolyte, where Li grows along grain boundaries, in deposition-induced cracks, or in other free spaces in the electrolyte at the submicron scale during cycling [37]. In a solid-state Li metal battery, these submicron defects are common in the SE at the Li / electrolyte interface [37]. Cell failure can occur when the stresses accumulated at these defects during Li plating and stripping become large enough to induce crack growth in the SE. If the maximum stresses are limited by the strength of Li, it is apparent from our results that nano-scale Li is capable of withstanding and thus generating far greater stresses than bulk polycrystalline Li. Due to the volume changes associated with plating and stripping Li, stresses may plausibly reach the highest strength measured on the electrodeposited Li in this work, over 27 MPa, or the largest stress measured, almost 70 MPa. These stresses are sufficient to induce crack growth in ceramic SEs with reasonable ($< 20 \mu\text{m}$) flaw sizes [37].

The large spread in the elastic modulus and strength quantified here for electrodeposited Li is also significant because only a single defect is required to penetrate through or fracture the SE to short circuit a battery. The strongest or stiffest Li dendrite could puncture or fracture the electrolyte or packaging even if the majority of formed dendrites are suppressed by the electrolyte. The 24x-greater-than-bulk strength of electrodeposited Li at small scales is intimately tied to the performance and implementation of solid-state batteries because it determines how much stress the Li layer can withstand, which ultimately may determine how the battery will perform.

5.5 Conclusions

In-situ nanomechanical compression experiments conducted on individual electrochemically grown single-crystalline Li nano-pillars expand the existing strength vs. size property space for Li and reveal (1) a range in the elastic modulus from 3.3 to 11.3 GPa, with an average of 6.76 GPa, and (2) strengths of 16.0 ± 6.82 MPa with no observable size effect, which is 24x greater than bulk polycrystalline strength and 16x lower than theoretical strength. This work highlights a profound dependence of the mechanical properties of small-scale Li on its deposition mechanism, resulting microstructure, environment, formation kinetics, and dimensions, and highlights the impact of these fundamental phenomena on operation and function of solid-state Li batteries.

Chapter 6

3D ARCHITECTED LI-ION CATHODES

Adapted from

2. Yee, D. W.*, Citrin, M. A.*, Taylor, Z., Tovmasyan, V. & Greer, J. R. Additive Manufacturing of Complex Metal Oxides for 3D Li Ion Battery Cathodes. (*In preparation*).

The previous four chapters discussed the formation, microstructure, and mechanical properties of Li grown out of a solid electrolyte. Using a Li metal anode can improve energy density, but changes to the battery architecture itself can also improve performance, especially to take advantage of the favorable properties of Li solid-state cells. This chapter will discuss the fabrication and characterization of efficient 3D architected LIB cathodes using a novel additive manufacturing process.

6.1 Three-Dimensional Batteries

The traditional planar design of LIBs presents a fundamental trade-off between energy and power density. To increase the energy of a battery without changing materials, more active material must be added. However, as the active material layer becomes thicker, the transport length of Li ions and electrons through the electrode increases as the thickness increases, reducing capacity at higher rates and reducing power [129, 130]. The energy density is usually dependent on the active material mass loading, defined as mass per areal footprint (mg/cm^2). Mass loading is particularly important for Li anode solid-state batteries and microbatteries, which require thin SEs due to the electrolytes' relatively low ionic conductivity as well as thin layers of Li and the cathode to maximize the overall energy density [2, 41, 129–132]. In conventional LIBs, composed of liquid electrolytes and electrodes formed of powders of an active material, conductive additive, and binder (“slurry electrodes”), thin cells can be wound around a central post in the “jelly-roll” design to increase energy density without increasing film thickness [133]. However, SEs, which are often brittle ceramics, and monolithic electrodes, such as sputtered ceramic cathodes, would likely fracture in this configuration [130, 131].

One promising approach to realize both high energy and power densities in solid-state batteries is to change the two-dimensional (2D) planar design into a three-dimensional (3D) architecture. By intelligently utilizing the height of the electrode, the mass loading can be increased while maintaining short Li ion and electron transport lengths [129, 130]. 3D electrodes are commonly measured by their areal capacity (mAh/cm^2), which can be improved by increasing the mass loading using the height of the electrode [130]. “3D batteries” commonly refer to any type of electrode design that utilizes an architected or porous design used to increase mass loading with shorter transport lengths [130]. However, many 3D electrode designs are “pseudo-3D”, i.e. their cross sections do not change with at least one spatial dimension. A common 3D battery electrode design is to use 1D structures like posts or nanowires [134, 135]. The 1D structures are often created by depositing active material into a template [134, 136–138], depositing the active material on a scaffold [139, 140], or directly growing the individual structures [141, 142]. These structures can increase the mechanical stability of the thin active material [141] and increase the areal capacity over a thin film [139], but they require high aspect ratios to greatly decrease Li ion diffusion paths, which limits their heights as the structures often fail or agglomerate when they are too tall [41]. 2D patterned electrodes can achieve similar increases in areal capacity, but have similar issues with height [143–145]. While many pseudo-3D and 3D electrodes can perform well in a liquid electrolyte by simply replacing a planar electrode, different electrode configurations must be utilized to exploit the advantages of 3D batteries with a full solid-state cell (anode, electrolyte, and cathode) [130]. One of the most common electrode configurations is to use interdigitated electrodes, which decreases the diffusion path between electrodes [146–148]. Interpenetration beyond planar interdigitation is difficult to achieve with only a few known examples [149, 150].

An ideal 3D electrode would include a large connectivity, controllable and ideal pore size, and be composed of an ordered structure to optimize the material loading and pore size. A single active material thickness and pore size is usually required to optimize the energy and power density of a cell, and a stochastic material will contain deviations of the optimum thickness and/or pore size [41, 151]. An ordered, periodic structure reduces defects that could short circuit the cell or increase the ion diffusion path [135, 152] and would be stronger than a stochastic foam at the same densities [153]. True 3D electrodes are less common and can be fabricated by depositing onto a 3D current collector / scaffold (often carbon or metal foam) [154–156], or by directly forming the active material using a heat treatment [149, 157, 158].

Additive manufacturing, commonly referred to as 3D printing, provides a promising route to create 3D electrodes with tunable geometries and dimensions. Currently, the majority of 3D printed LIB electrodes are created by adding powders of active materials to a slurry or ink [148, 159–162] or polymer [163]. These methods add inactive ingredients into the electrodes, thereby reducing energy density, and are often limited in geometry. Inks sometimes cannot be printed over free space and must be supported by a printed layer underneath [164]. To our knowledge, there is only one existing study that developed a 3D printed electrode composed of just the active material, in that case a Ag microlattice electrode fabricated using Aerosol Jet 3D printing [158]. One of the largest challenges for 3D printing LIB electrodes is the difficulty in printing non-polymeric materials that are commonly used in LIBs [165]. Recently, we have developed a new additive manufacturing technique called photopolymer complex synthesis to 3D print oxides [166].

Utilizing this method, 3D architected transition metal oxide LIB cathodes were fabricated. This technique incorporates metal salts with desired cations into a photoresin that can be 3D printed into hydrogel structures using digital light processing (DLP). The cubic lattices were manufactured and calcined in air to produce structures 7.5-8 mm wide and ~1.3 mm tall. The primary material studied was LCO because of its well understood electrochemical properties and its common use as a LIB cathode material. The largest challenge for 3D solid-state batteries is the conformal deposition of solid electrolytes on 3D structures [130, 131], normally performed using atomic layer deposition (ALD) [167, 168] or polymer electrodeposition [169, 170]. The use of a solid electrolyte with the 3D electrode is outside the scope of this work, so a conventional liquid electrolyte was used to investigate the electrochemical performance of the lattices. The lattices have a porous microstructure formed of ~230 nm diameter crystallites and have reasonable gravimetric discharge capacities of 122 mAh/g and areal capacities up to ~8 mAh/cm² with a capacity retention of 82% over 100 cycles.

6.2 Fabrication of 3D Architected LCO Electrodes

To fabricate the 3D electrodes, a custom aqueous photopolymer resin with the necessary metal cations was formulated. The aqueous resin contains LiNO₃ and Co(NO₃)·6H₂O aqueous salt solutions mixed with poly(ethylene glycol) diacrylate (PEGDa, Mw = 575 g/mol) and a lithium phenyl-2,4,6 trimethylbenzoylphosphinate (LAP) photoinitiator and Benetex OB-M1 UV blocker with a salt loading of 230 mg / mL resin (Figure 6.1(a)). The resin was poured into the tray of the DLP 3D printer

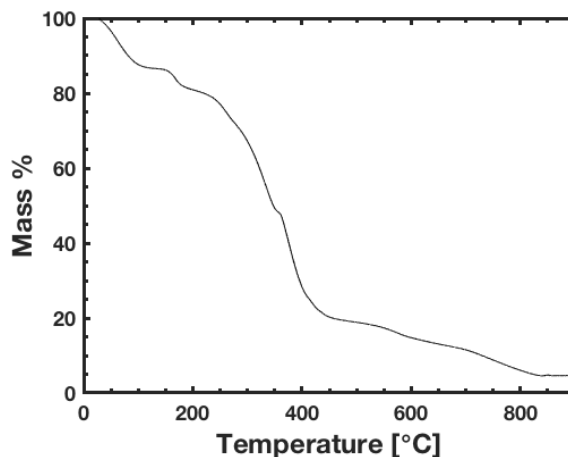


Figure 6.2: Thermogravimetric analysis (TGA) of the Li^+ and Co^{2+} containing resin under N_2 flow. Most of the mass decrease happens between 235 and 450 °C.

of organic material. The mass then decreases more gradually by 15% until 850 °C. An important caveat is that this was done under N_2 gas instead of air (like the calcination process) because the TGA under air was not available. We would expect the mass change during calcination to be more similar to that in Reference [166] (TGA performed in air), where the combustion happens ~ 130 °C with a sharp decrease in mass and most of the mass loss is completed around 400 °C. However, that resin had a salt loading of 760 mg/mL, much larger than the LCO resin, so the mass loss will likely be somewhat slower for this work. Based on this information, we chose our burn profile to minimize the thermal ramp rate in the temperature range with the largest mass loss (100- 500 °C) while increasing the ramp rate over other temperatures to minimize the overall time of the calcination. The samples were calcined in a furnace (MTI OTF-1500X) in air at ~ 22 torr at 1 °C / min to 100 °C, 0.25 °C / min to 500 °C, 2 °C / min to 700 °C, a 3 hour hold at 700 °C, then cooled down to room temperature at 2 °C / min. 700 °C was chosen as the maximum temperature because it has been shown to optimize the rate capabilities of LCO [171]. This process has some similarities with solution combustion synthesis, where a metal salt with an oxidizing anion and fuel are mixed in a solvent and heated, producing metal oxide nanoparticles of compounds involving the metal cation due to the heat and gas produced by the combustion reaction [172]. Our process's combination of solution combustion synthesis with photolithography and polymer complex solution has been termed "photopolymer complex synthesis" [166].

Free-standing lattices were printed with cubic unit cells and beam diameters of ~ 870

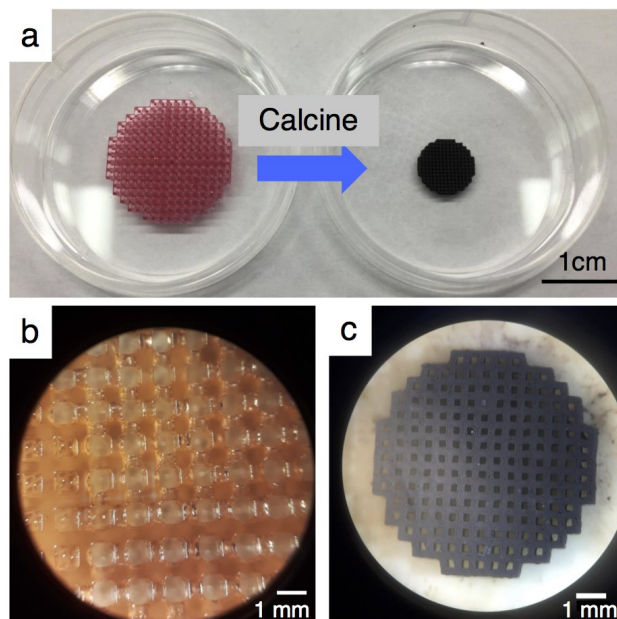


Figure 6.3: (a) Image of the lattices before and after calcination. (b) Beams of the as-printed lattice and (c) calcined lattice at the same magnification.

μm and $\sim 240 \mu\text{m}$, respectively. The overall shape was roughly cylindrical with 15-20 unit cells in width and 3 unit cells in height producing overall dimensions of 15-16 mm wide and $\sim 2 \text{ mm}$ tall (Figure 6.3(a, b)). The water content in the printed structures gradually evaporated, so the size of the structures fluctuated due to the time between printing and calcination. Features could be seen on the surface in an ordered pattern with a spacing of $\sim 48 \mu\text{m}$. The ordered pattern on the surface of the lattices likely arises from the pixels from the projector. The relative density of the structure, i.e. the volume of material in the unit cell divided by the length of the unit cell cubed, is 43%.

Post calcination, the lattices turned black with unit cell and beam diameters of $\sim 410 \mu\text{m}$ and $\sim 140 \mu\text{m}$, respectively (Figure 6.4(a)) with a mass loading (mass / area) of $50\text{-}60 \text{ mg/cm}^2$. The overall dimensions were 7.5-8 mm wide and $\sim 1.3 \text{ mm}$ tall and the ordered pattern on the surface of the beams, with a spacing of $23 \mu\text{m}$, became more evident (Figure 6.4(b)). Figure 6.4(d,e) show the microstructure formed of crystallites with sizes of $230 \pm 76 \text{ nm}$ with a microscale porosity of $\sim 36\%$ determined by image analysis. The lattices contained some cracks on the surface, mostly located at the nodes (Figure 6.4(c)). These cracks were more common if the thermal ramp rate of the calcination process was relatively high ($1 \text{ }^\circ\text{C} / \text{min}$); ramp rates of $0.5 \text{ }^\circ\text{C} / \text{min}$ and below produced few surface cracks at the nodes.

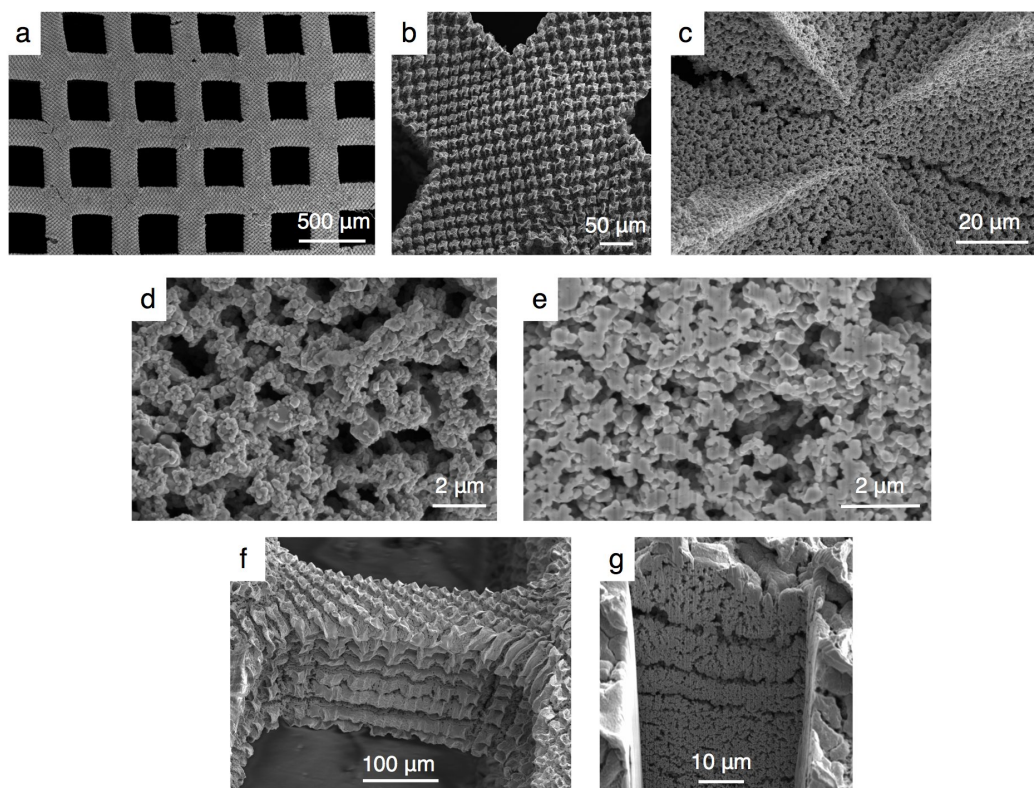


Figure 6.4: (a) Low magnification image of pristine beams of a calcined LCO lattice. (b) The pattern of pixels on a node. (c) A node crack on a heavily-cracked lattice. (d) A high magnification image of the particle microstructure in the node crack. (e) FIB cross section image of the particles microstructure in the interior of an intact node. (f) The side of a beam revealing the layers of the print, which can also be seen in the FIB cross section (g).

The layers of the printing process were also visible on the sides of the beams, seen in Figure 6.4(f). FIB cross sections of the beams showed a similar porosity as the surface, sometimes with small $\sim 2 \mu\text{m}$ spacing between the print layers (Figure 6.4(g)). However, at the nodes, the cross sections revealed large pores of at least $123 \mu\text{m}$ tall x $34 \mu\text{m}$ wide, illustrated in Figure 6.5(a). The nodes of damaged lattices that contained more surface cracks showed large spherical pores between 33 and $146 \mu\text{m}$ in diameter (Figure 6.5(b)).

The cubic unit cell was chosen for its simplicity and because some other printing methods, such as inkjet printing, struggle to print overhanging features over free space, which DLP printing easily performs [164]. During the calcination process, water is driven off and the nitrate salts combust the organic molecules in the resin around $130 \text{ }^\circ\text{C}$. During this combustion and the heat treatment, the cations in the

salt oxidize to become oxide nanoparticles [172], which gives rise to the lattice porosity. Theoretical linear shrinkage was calculated as 77% following the method in Reference [166]. Briefly, all the Li and Co in the resin are assumed to fully transform into LCO during calcination and the radius shrinkage of a sphere of resin to a sphere of monolithic LCO is calculated. The calcination decreased the mass of the lattice to an average of 5.44% of the original mass. The measured structural linear shrinkage after heating is 52.7%, so volumetrically it shrinks 89.4% assuming isotropic shrinkage, while the decrease in mass is 94.6%. The pixel pattern on the lattices also shrinks by 52%. The shrinkage in height of about 35% is less than that of the other linear dimensions. This may be due to the difficulty measuring the height of the LCO lattices because of their lack of mechanical robustness and any warping after calcination would increase the apparent height of the lattices.

The discrepancy in the leftover material (10.6% of original volume and 5.44% of the original mass) can be explained by the porosity: the mass shrinkage is 51% of the volume shrinkage, somewhat larger than the measured porosity of 36%. However, this porosity is the microscale porosity of the crystallites; it does not take into account the many large pores in the nodes or any other large pores in the lattice, so it is underestimated. The “true” porosity is thus likely close to 51%. To compare the shrinkage to the theoretical shrinkage, the measured linear shrinkage should be multiplied by the porosity, which gives 79.6%, similar to the theoretical linear shrinkage of 77%. The discrepancy may be due to the impurities in the material and non-linearities in shrinkage. Therefore the full porosity of the lattices, including both the prescribed structural relative density and porosity, is ~80%.

The cracks and pores seen preferentially located on the nodes likely result from the $\sqrt{2}$ times longer distance that gas needs to escape in the node vs. a beam. A slower thermal ramp rate should allow more time for the gas to escape during calcination and produce fewer cracks, especially at the nodes. Our observations are consistent with this explanation, as a 0.2 °C / min ramp rate produces many fewer cracks than a 1 °C / min ramp rate.

The porous, particle-like microstructure seen in these lattices is distinct from the monolithic morphology of lattices with submicron features printed using a similar photoresin and calcination process [166]. That work fabricated structures using two-photon lithography, where a laser is rastered in a photoresin that polymerizes at the laser voxel when the polymer locally absorbs two photons, which allows for a much higher resolution (~1 μm as printed) and smaller throughput (~1000 $\mu\text{m}^3/\text{hr}$

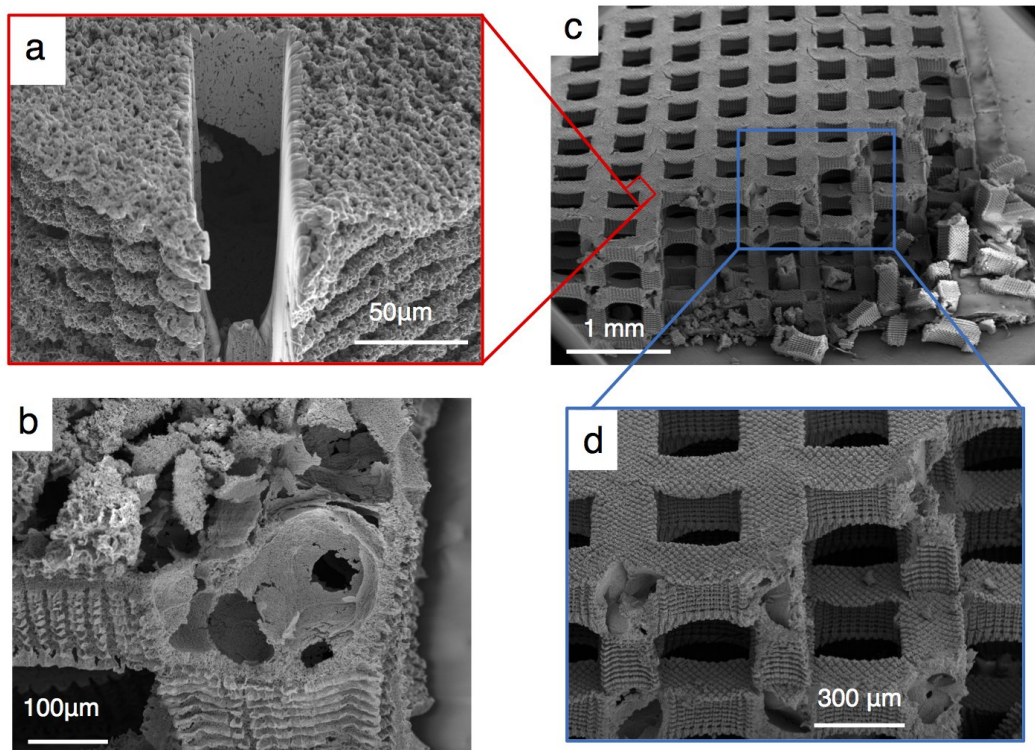


Figure 6.5: (a) FIB cross section of an internal node illustrating a $>100\ \mu\text{m}$ pore. (b) Spherical pores are seen in broken nodes of very cracked lattices. (c) LCO lattice with a damaged edge. (d) Zoomed-in image of the nodes of the damaged edge demonstrating node failure.

as printed). Because DLP printing produces feature sizes much larger than the grain size and gas has larger distance to escape compared to two-photon lithography, the structures in this work are porous instead of monolithic. In addition, the lower mass loading of salts in our work produce more shrinkage, which also leads to a more porous structure.

Unfortunately, the lattices were damaged very easily; lattices with cracked nodes calcined at higher ramp rates crushed under very light pressure, while lattices with fewer node cracks survived some light handling with tweezers. The low mechanical robustness of the lattices is intimately tied to its morphology. The porous structure contains many crystallites that are connected at only a few points, similar to poorly consolidated granular materials, which have low strength when poorly connected [173]. The contribution of the nodes plays a crucial role in the deformation of lattice architectures [174]. The internal pores at the nodes significantly weaken the structure because there is less material there to support any applied stress, resulting

in failure controlled by beam failure at the nodes (see Figure 6.5(c,d)). The strength of brittle materials is largely governed by the flaw size and population inherent in the material due to its processing, with the stress to propagate a crack proportional to $1/\sqrt{a}$, where a is the flaw length [175]. The large pores and defects in the lattices will contribute to their low toughness by greatly decreasing the stress necessary to propagate cracks to fracture the structure. The surface cracks from faster thermal ramp rates provide large flaw sizes to further decrease toughness, consistent with our observations that the low thermal ramp rate lattices better resist failure.

6.3 Materials Characterization of LCO Structures

Samples were pulverized into a fine powder between glass slides in order to perform powder x-ray diffraction (XRD) on a PANalytical X'Pert Pro x-ray powder diffractometer at 45 kV and 40 mA with a Cu k_α source. Figure 6.6(a) shows the XRD spectrum of the lattices with peaks consistent with the α -NaFeO₂ layered structure of LCO (Figure 6.6(b)). The (003)/(104) peak ratio is 1.52; ratios greater than one signal that the cations in the structure are well ordered, improving cycle life [176]. A small peak shift of $\sim 0.7^\circ$ compared to the reference sample [177] was consistent between all samples, even a commercial LCO powder (Sigma Adrich), and so was likely an instrument artifact.

The chemical composition of the lattices were investigated by energy-dispersive x-ray spectroscopy (EDS), performed on a Zeiss 1550VP FESEM with an Oxford X-Max SDD EDS detector at 10 kV (Figure 6.6(c)). EDS spectra of the lattice exhibited mostly Co and O with the composition shown in Table 6.1. Unfortunately, Li cannot be seen in EDS without specialized equipment due to its low scattering cross-section and absorption of the produced x-rays by the detector window [179]. The ratio of O to Co was 1.9, similar to the ratio in stoichiometric LiCoO₂. The impurities in the structure were, in descending order of atomic percentage (at%), C, P, S, Na, and S. The combined at% of impurities was 6.6 at%, assuming an equivalent atomic percentage of Li and Co. The impurities arise from incompletely combusted organic material (C), the photoinitiator (P), the counter ion of the UV blocker (Na), and the UV blocker (S). The elemental maps were generally uniform, even at the pixel level ($\sim 20 \mu\text{m}$), with a few spots containing excess S around 2 at%. It is possible that S and P reacted with oxygen and another cation to form sulfates or phosphates. These were not detected in XRD; Co fluoresces under Cu k_α radiation, which produces a strong background that can obscure any trace impurities [180]. The amount of material that is likely LCO is therefore $\sim 93 \text{ at}\%$ / $\sim 95 \text{ wt}\%$.

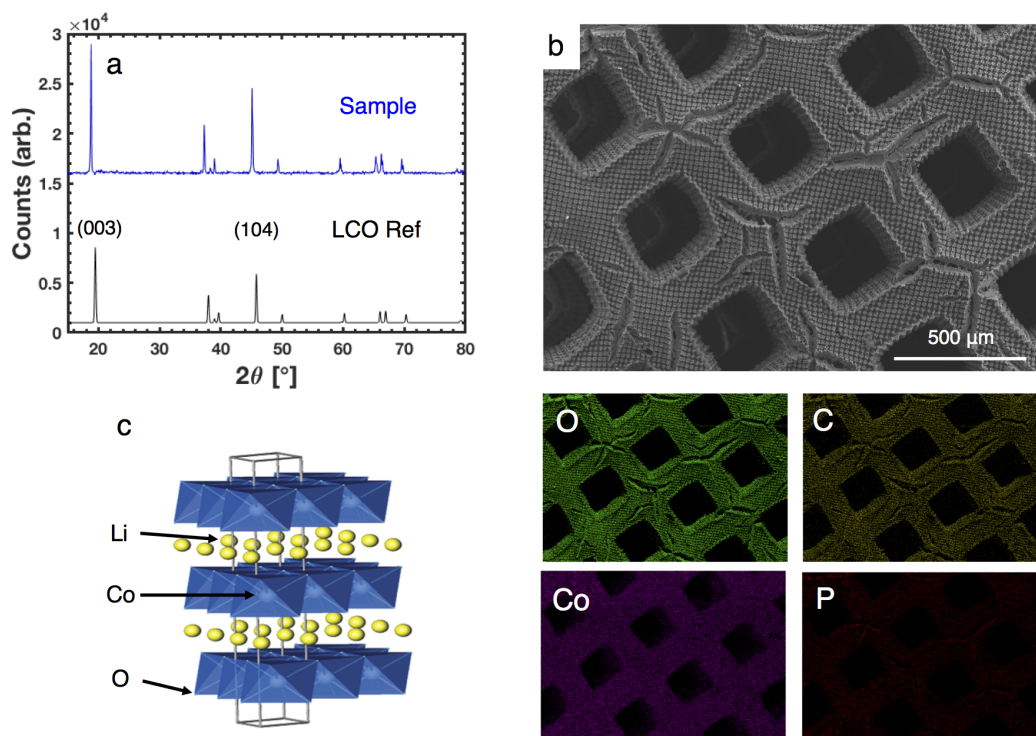


Figure 6.6: (a) XRD spectrum from a pulverized LCO lattice and reference spectrum taken from Reference [177]. (b) Crystal structure of LCO adapted from Reference [178]. Co^{3+} ions lie in the center of O^{2-} octahedra and the gray box outlines a unit cell. (c) SEM image of the lattice with elemental maps from EDS illustrating the four elements with the highest atomic concentrations.

Quantitative elemental data from EDS is somewhat inaccurate, especially for lighter elements, so the exact compositions may vary by a few at%.

To further confirm the lattices were indeed composed of electrochemically active LCO, cyclic voltammetry (CV) was performed on slurry electrodes fabricated from lattices pulverized by crushing between glass slides. In a CV experiment, the voltage is swept from the OCV up to an upper voltage, where it is swept back down to a lower voltage. The cycles can then be repeated. Cyclic voltammograms reveal at which voltages electrochemical reactions take place by measuring a peak in current at these voltages.

To fabricate the slurry electrodes, the powder from the crushed LCO structure was first mixed in vortex mixer in a polyethylene vial with isopropyl alcohol and zirconia ball-mill balls for 2 hours. The resulting mixture was poured into a glass dish and dried at 60 °C for 2 hours then at 100 °C in vacuum for 18 hours. The electrode slurry was composed of 80 wt% of this active material, 10 wt% conductive additive

	At%	At% w/ Li
O	59.5	45.1
Co	31.8	24.1
Li	-	24.1
C	5.1	3.9
P	2.7	2.0
Na	0.5	0.4
S	0.4	0.3

Table 6.1: Atomic percentages taken from EDS spectra. The first at% column is the data from the instrument and the second at% column assumes the same at% for Li and Co and recalculates the overall composition.

(super C65 carbon black), and 10 wt% binder polyvinylidene fluoride (PVDF) in N-methyl-2-pyrrolidone (NMP). The slurry was mixed in a polyethylene vial with zirconia ball-mill balls for 5 hours. It was then cast onto Al foil with various thickness using a film applicator blade and dried for 12 hours at 50 °C. 11.1 mm diameter electrode discs were punched out of the foil and the electrodes were dried for 18 hours at 100 °C under vacuum. Samples were tested in CR2032 coin cells that were assembled in an argon-filled glovebox. 30 μ L of 1 M LiPF₆ in 1:1 ethylene carbonate:diethyl carbonate electrolyte (EC:DEC, BASF Selectilyte LP 40) was used as the electrolyte. Li foil was used as the counter electrode (Sigma Aldrich, purity: 99.9%) with a 25 μ m thick polypropylene (PP) separator. CV was performed using a BioLogic BCS-805 battery cycler scanning between 3 V and 4.2 V at a scan rate of 0.005 mV/s, slow enough to approach equilibrium.

Figure 6.7(a) illustrates the primary peaks in the CV scan. During the first cycle, the anodic scan exhibited a large peak at 3.929 V with two smaller peaks at 4.068 V and 4.184 V. The reverse cathodic scan showed corresponding peaks at 3.893 V, 4.056 V, 4.170 V. During the second cycle, the peaks shifted slightly to 3.928 V, 4.071 V, and 4.181 V in the anodic scan and 3.894 V, 4.053 V, and 4.107 V in the cathodic scan. The peaks in the CVs performed on slurry electrodes from LCO lattices are virtually identical to the peaks observed in literature [181, 182]. The redox couple at 3.929 / 3.893 V corresponds to a first order phase transition between two hexagonal phases, while the peaks at 4.068 / 4.056 V and 4.184 / 4.170 V correspond to an order / disorder transition of Li ions with a distortion to a monoclinic phase [181, 183, 184].

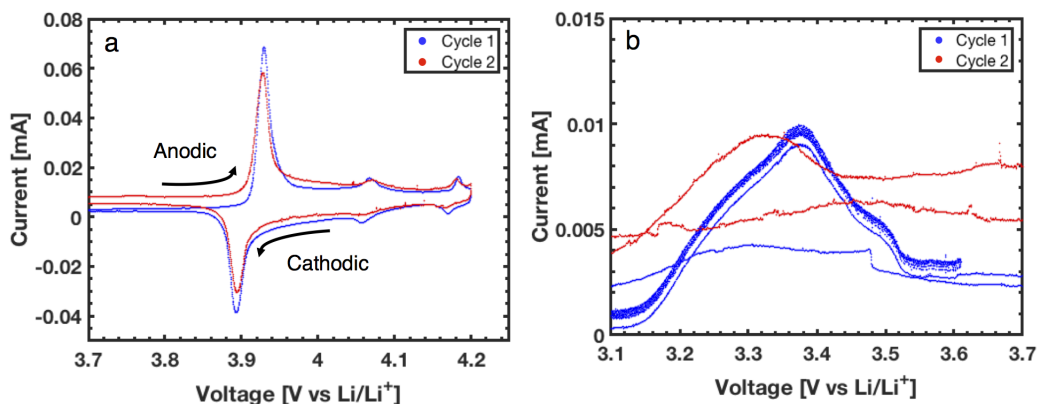


Figure 6.7: (a) 2 cycles of a CV scan at 0.005 mV/s between 3 and 4.2 V. The 3 major LCO peaks fall between ~ 3.9 and 4.2 V. (b) Lower voltage peak of the CV scan ~ 3.4 V. The denser data points below 3.6 V on the anodic scan of the first cycle are due to a different data acquisition rate. The rate was changed around 3.6 V to reduce the overall number of data points.

The peaks in the second cycle were only 11 mV different on average compared to the first cycle, illustrating the reversibility of Li ion intercalation and deintercalation in the fabricated LCO. On the first cycle, there was a broad low voltage peak at 3.38 V that did not have a corresponding cathodic peak (second cycle: 3.35 V), seen in Figure 6.7(b). The difference in current between the anodic and cathodic scans at this peak for the first cycle was 7.66 μA and decreased on the second cycle to 4.96 μA . This peak is likely due to some impurity in the LCO material or in some other part of the cell, such as the electrolyte, because LCO is not electrochemically active in this range [181]. The current decay between cycles is indicative of the irreversibility of this peak and the small currents suggest that the peak is due to a low concentration impurity.

6.4 Electrochemical Performance of 3D LCO Electrodes

Because of the LCO structures' low mechanical robustness, replacing the traditional slurry electrodes in conventional 2032 coin cells to investigate the electrochemical performance of the lattices is infeasible. The stress applied to the layers in the coin cell stack to crimp the cell and keep components in electrical contact can reach the order of 1 MPa [185]. This stress easily destroys the LCO lattices; to electrochemically probe the structures, they need to be electrically connected to the cathode current collector and infilled with the electrolyte without any applied direct pressure. A conductive adhesive can connect the lattice to a current collector

(stainless steel spacer) and taller-than-sample rings can be placed around the lattice so direct pressure is applied to the rings instead of the lattice (see Figure 6.8 (a)). PP rings were used because PP is a common LIB separator material and is stable under cycling conditions. The conductive adhesive cannot react with the electrolyte and needs to be stable under the chemical environment and large voltages applied to the cell. Carbon glue (Ted Pella) was first used to stick the lattice to the spacer, and the cell showed no capacity. Upon disassembling, the lattice was not attached to the spacer and the electrolyte was black, i.e. the electrolyte dissolved the carbon glue. This highlights the reactivity of the cell environment and the importance of a conductive adhesive that is stable during cycling.

Carbon black and PVDF are very commonly added to LIB electrodes as a conductive additive and binder, respectively, and are therefore stable under cycling conditions. A conductive adhesive was fabricated by mixing 75 wt% conductive super C65 carbon black and 25 wt% PVDF binder in NMP in a 1.28 mL:100 mg solvent:solid ingredients ratio. The solution was mixed in a vortex mixer in a polyethylene vial with zirconia ball-mill balls for 24 hours. The mixture was drop-casted onto a 0.2 mm stainless steel spacer and thinned to ~0.5 mm thickness using a film applicator blade to minimize cracking. The LCO lattice was then carefully placed into the middle of the adhesive and the whole stack was dried at 35 °C for 4 hours (Figure 6.8(b)). Cracks still occurred in the adhesive but the lattices were firmly attached and did not move when the spacer was flipped upside down and shaken with tweezers. PP rings with thickness of 1.6 mm and 0.18 mm with inner and outer diameters of 9.5 mm and 15.9 mm, respectively, were thinned using a rotary power tool to an inner diameter of ~11 mm to more easily fit around the lattices. The rings were placed around the LCO structure to support the stress of the coin cell spring. A 0.18 mm thick PP ring is added if necessary to increase height. Figure 6.8 (a) illustrates the cell stack from bottom to top: smaller coin cell case, spacer with lattice attached, a 1.6 mm thick PP ring, a PP separator, Li counter electrode, spacer, spring, and top case. Cells were assembled in an argon-filled glovebox and the electrolyte (1 M LiPF₆ in 1:1 EC:DEC) is inserted into the cell cavity until the cell case is full of electrolyte (~ 400 µL) after the PP rings are placed down. Some electrolyte spilled out the cell during crimping, so the actual amount of electrolyte in the cell is less than 400 µL. The available volume in the cell cavity for the electrolyte is approximately 150-200 µL. Control cells that contain PP rings and the carbon adhesive without the 3D LCO cathode did not exhibit any capacity.

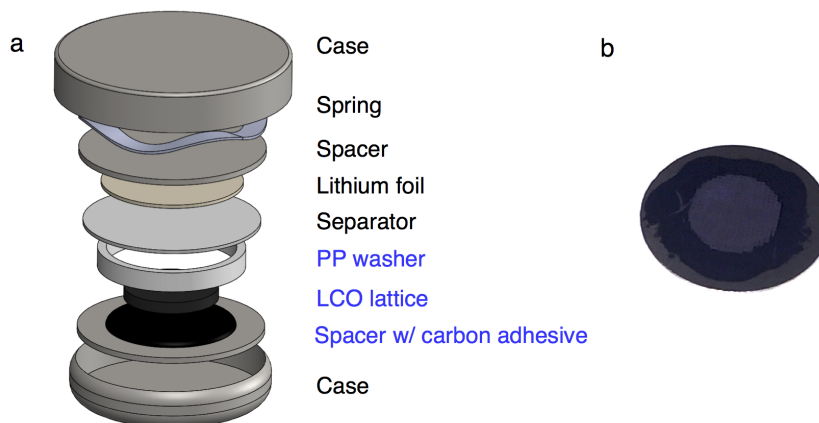


Figure 6.8: (a) Schematic of the cell stack in the 2032 coin cells. Liquid electrolyte is applied into the cell before the separator is added. (b) LCO lattice attached to a stainless spacer with the carbon adhesive.

Coin cells were analyzed by either a BioLogic BCS-805 battery cycler or Neware BTS4000 cycler and were cycled galvanostatically between 3.0 and 4.2 V at $C/40$ for two cycles, slow enough to minimize polarization, then at increasing rates for 5 cycles each to $2C$, then for up to 200 cycles at $C/10$. A rate of $1C$ corresponds to a discharge or charge in 1 hour based on the theoretical capacity of LCO (155 mAh/g), $2C$ corresponds to a 30 minute half-cycle, etc. The voltage profiles for LCO lattices seen in Figure 6.9(a) show a plateau around 3.93 V on charge and 3.88 V on discharge and small plateaus ~ 4.15 V and 4.2 V on charge and discharge with a first cycle irreversibility of 20 mAh/g at $C/40$. This voltage profile is similar to that of LCO reported in the literature, with a plateau ~ 3.9 V and small plateaus ~ 4.1 and 4.2 V around 10 mAh/g of charge or discharge [182]. These plateaus correspond to the peaks in the CV, which arise from a first order phase transition and order / disorder transition, respectively [183]. The combination of CV, voltage profiles, XRD, and EDS all provide confidence that the 3D architected electrodes are composed of electrochemically active LCO, virtually identical to that commonly used in LIB cathodes.

The first specific discharge capacity at $C/40$ was 122 mAh/g, and the the first discharge capacities at $C/20$, $C/10$, $C/5$, and $2C/5$ are 96.6%, 91.4%, 85.0%, and 57.2% of the first discharge capacity at $C/40$, respectively (Figure 6.9(b)). The lattices did not show capacity at rates of $1C$ or $2C$. Two samples cycled at $2C/3$ showed a capacity of 21.9% compared to $C/40$. The average Coulombic efficiency (CE), the ratio between the discharge and charge capacities, for the first 88 cycles at $C/10$

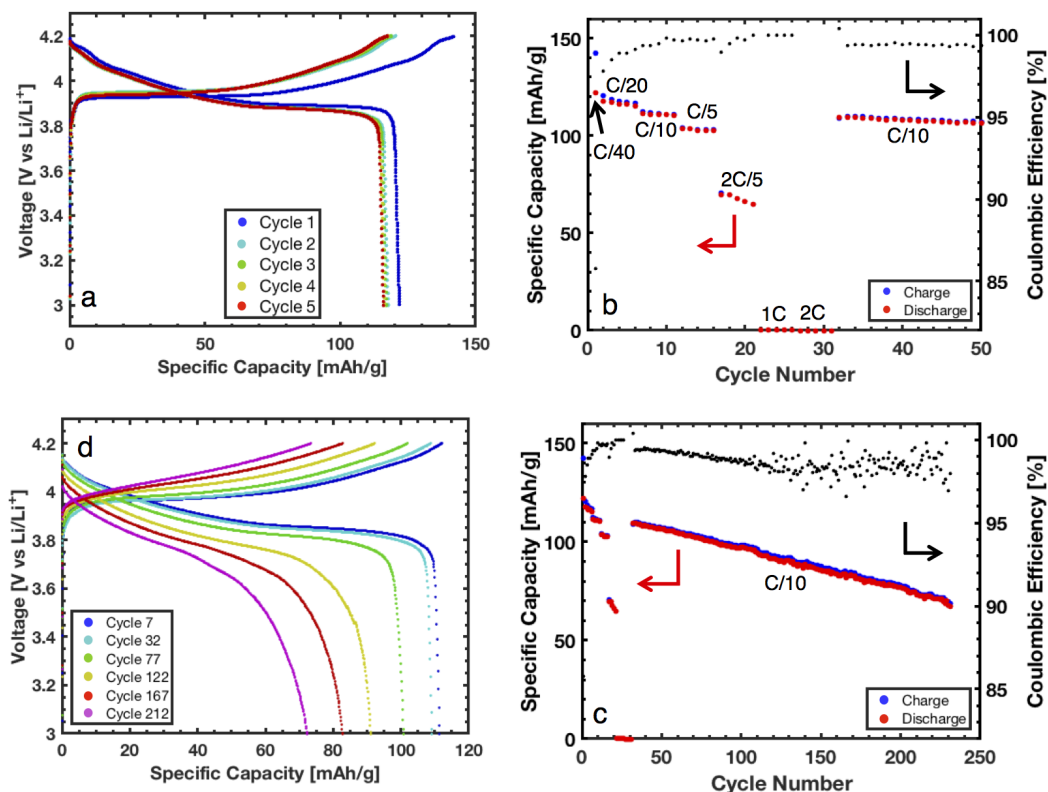


Figure 6.9: Electrochemical performance of the LCO lattice. (a) Voltage profile during charge at C/40 for 1 cycle and C/20 for cycles 2-5. (b) Specific capacity and Coulombic efficiency during the first 50 cycles at various currents. (c) Specific capacity and Coulombic efficiency over 231 cycles. (d) Voltage profile at various cycles at C/10. Cycle 7 is the first C/10 cycle and cycle 32 is the sixth C/10 cycle; all subsequent cycling was at C/10.

(110 overall cycles) was 99.0% with a standard deviation of 0.373%. Interestingly, during the subsequent cycles, the variance in CE increased, with an average of 98.4% and standard deviation of 0.608%. Small sections of the structure losing and regaining electrical contact during the later cycles could explain the variance increase. Figure 6.9(c) illustrates the extended cycling, with a linear capacity decay of 0.18% per cycle over 231 cycles. The first specific discharge capacity at C/40 of 122 mAh/g is lower than the theoretical capacity of 155 mAh/g for $\text{LiCoO}_2 \rightarrow \text{Li}_{0.5}\text{CoO}_2$, although it is very similar to LCO particles fabricated by conventional combustion synthesis [186, 187].

The somewhat lower capacity arises from many factors, including the 5 wt% of impurities, small amounts of the lattice breaking and becoming disconnected during coin cell fabrication, some parts of the lattice possibly covered by the C adhesive,

incomplete electrolyte infiltration, and the Ohmic drop across the electrode. Because there is no conductive additive and the electrode is relatively tall, the electrical resistance from LCO (a semiconductor in the lithiated state [188]) contributes to a large Ohmic drop. The addition of a large (~ 30 wt%) amount of conductive additive has been shown to increase gravimetric capacity [171]; this amount of inactive materials would decrease the absolute capacity, however.

The polarization, defined as the difference in voltage between charge and discharge at 10% state of charge, gradually increased during extended cycling at C/10, with a polarization of 0.14 V for cycle 7 (first C/10 cycle), 0.15 V for cycle 32, 0.19 V for cycle 77, 0.41 V for cycle 122, 0.51 for cycle 167, and 0.62 V for cycle 212 (Figure 6.9(d)). Cycle 32 is the sixth C/10 cycles and all subsequent cycles were at C/10. Polarization increasing during cycling is typical for LIB electrodes and is normally attributed to disconnection of active material and a gradually thickening SEI layer [189]. These degradation mechanisms may be somewhat exacerbated in the LCO structures due to their lack of mechanical stability and larger surface area.

The polarization also increased for increasing current, with values of 0.046 V for C/40, 0.090 V for C/20, 0.14 V for C/10, 0.29 V for C/5, and 0.52 V for 2C/5. The voltage curves for the first cycle at each current are shown in Figure 6.10(a). Polarization almost always increases with current, as the Ohmic drop, activation polarization, and concentration polarization increase with current [16]. The lack of conductive additive and large electrode height will increase the Ohmic drop, reducing the capacity at larger currents. If the polarization, which is linear with current, is extrapolated to 1C, the polarization would be 1.3 V, greater than the experimental voltage range, resulting in no measured capacity.

Slurry electrode fabricated from pulverized lattices exhibited lower gravimetric capacities around 97 mAh/g at C/40. The capacities at C/20, C/10, C/5, 2C/5, 1C, and 2C are 95.8%, 86.0%, 84.1%, 79.9%, 65.2%, and 37.9% of the first discharge capacity, respectively (Figure 6.10(b)). The areal capacity of the lattice was 35x larger than the areal capacity of the slurry electrodes, largely driven by the 28x increase in mass loading provided by the relatively tall structure. Because of the thinness of the slurry (~ 25 μm thick), the transport length for Li ions during cycling is greatly reduced, allowing for much higher relative capacity at 2C/5, 1C, and 2C compared to the lattice. In addition, the 10 wt% of C conductive additive improves the high rate performance of the slurry electrodes. The decay rate was also roughly linear and smaller than that of the lattices, at 0.12% per cycle (Figure 6.9(c)). The

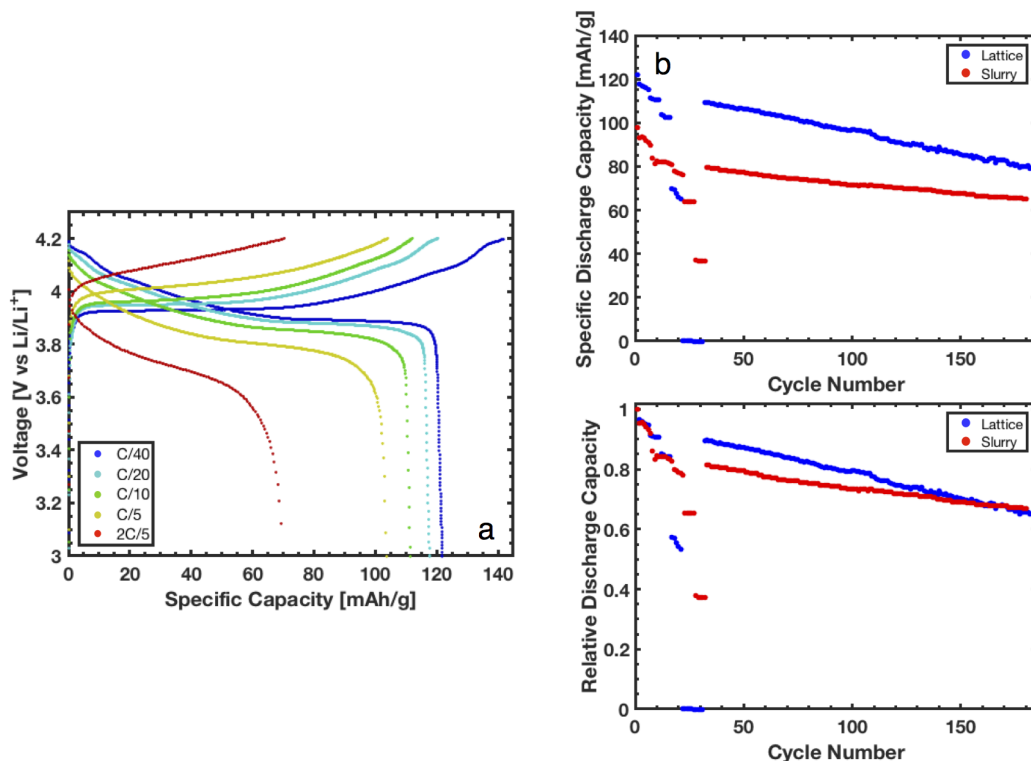


Figure 6.10: (a) Voltage profile of the first cycle at various currents. (b) Specific discharge capacity of an LCO lattice vs. a slurry electrode fabricated from pulverized LCO lattices. (c) Discharge capacity of an LCO lattice vs. a slurry electrode fabricated from pulverized LCO lattices relative to the first discharge capacity.

larger decay rate and worse high current performance of the 3D LCO structures is again likely due to the lack of conductive additive and structural features that can disconnect during cycling. The lower specific capacity for the slurry is surprising, as it should be similar to that of the lattice. Likely, the slurry-making procedure resulted in the lower specific capacity, possibly due to film delamination; the slurry electrodes exhibited lower gravimetric capacity compared to the lattice electrodes over all 9 samples. Nevertheless, this comparison allows us to decouple the electrochemical properties of the 3D structure vs. the material; the poor performance of the 3D electrodes at higher rates is due to the structure and height, while the capacity of the architected electrodes at low currents is limited by the inherent material.

The first areal discharge capacity of the lattices at C/40 is 7.6 mAh/cm², ~2 times larger than conventional slurry electrodes. The areal capacity during cycling is shown in Figure 6.11(a, b). The improvement in areal capacity is due to the large increase in height made feasible by the additive manufacturing process. It is difficult

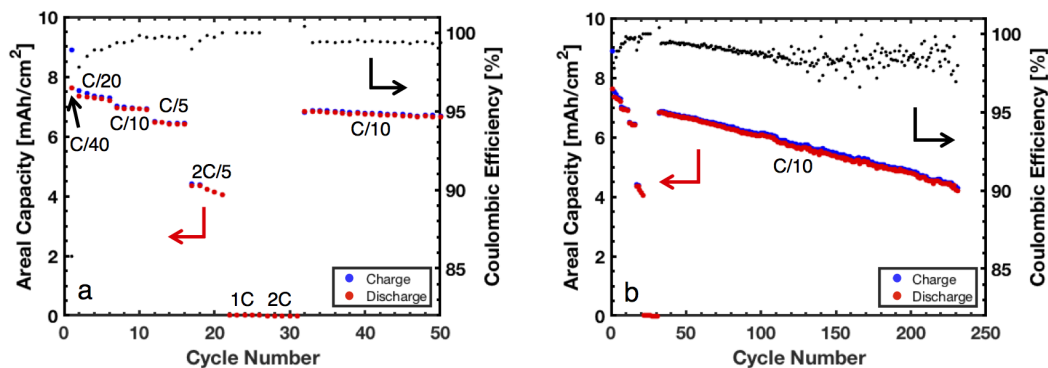


Figure 6.11: (a) Areal capacity and Coulombic efficiency of an LCO lattice during the first 50 cycles of cycling at various currents. (b) Areal capacity and Coulombic efficiency of an LCO lattice over 231 cycles.

to create electrodes with these heights using other methods, often requiring densely sintered electrodes [188] or ink based 3D printing [159]. Areal capacities over 10 mAh/cm² have been demonstrated using various deposition methods. For example, Wei et al. 3D printed 1 mm Li₄Ti₅O₁₂ and LiFePO₄ electrodes using an ink-based printing process and measured ~13 mAh/cm² for a full cell at low current densities (0.2mA/cm²) [159]. Using LCO electrodeposited onto a carbon foam, Zhang et al. achieved ~20 mAh/cm² at C/5 [154]. Lu et al. fabricated ~1 mm thick LCO electrodes by infilling a wood template and infilling the resulting structure again to reach 22.7 mAh/cm² [190]. The 3D printed LCO lattices in this work did not reach the large areal capacities of these other works due to their mass loading limitations from the overall porosity of the structure ~80%. However, the lattices still provided a ~2 increase in areal capacity over traditional planar electrodes and provide other advantages, such as the ability to print arbitrary structures that are binder and scaffold-free. DLP printing is also inherently a faster and more scalable technology compared to many other 3D printing technologies [164]. The time to print scales almost exclusively with height because each layer prints simultaneously, so the printing of structures that are much larger in the x-y directions or many smaller structures of the same height happens in virtually the same time as one coin cell-sized structure.

There are multiple routes that can be explored to improve and optimize the electrochemical performance of printed LCO structures. Other unit cell geometries, such as an octet, could increase mass loading with the same beam diameter and provide more stiffness and strength. The burn profile can be optimized to reduce

porosity and defects by reducing the thermal ramp rate and burning at the maximum temperature for longer times. A second infill step could be used to greatly increase mass loading, similar to Li et al. [190]. The chemistry in the resin can also be tuned; salts that are less oxidizing than nitrates, such as acetates, could reduce the violence of combustion and therefore increase mechanical robustness and mass loading. The concentration of salts could be optimized to control the resolution and porosity of the structure. Reduction in pixel size in the micrometer display of DLP printers could also improve resolution. If the calcination profile is optimized to increase mechanical stability and carbon content, then the electrochemical performance may also be enhanced by reducing polarization.

The metal cations in the photoresin and their concentrations can be tuned to produce oxide 3D structures of various LIB-relevant materials. This chapter was focused on fabricating and characterizing LCO lattices, but some resins were made with salts in the correct stoichiometric ratios to produce another common LIB cathode, $\text{LiNi}_{0.8}\text{Co}_{0.15}\text{Al}_{0.5}\text{O}_2$ (NCA). Using a very similar procedure as discussed in this chapter, NCA lattices were fabricated with similar dimensions to LCO lattices. Figure 6.12(a) shows the XRD spectrum from pulverized NCA lattices that reveals peaks from the lattices that match with the $\alpha\text{-NaFeO}_2$ layered structure of NCA with a (003):(104) peak ratio of 1.12. EDS reveals that the lattices are composed of mostly O and Ni in addition to Co and Al (Figure 6.12(b)), with impurities of C, P, S, and Na. The molar ratio of Ni/Co and Ni/Al was 5.4 and 13.6, respectively, similar to the ideal ratio of 5.3 and 16 for NCA. The deviation in the Ni/Al ratio is likely due to the inaccuracies of EDS for light elements and small at%. However, the measured ratio of Ni/O is 0.63, much higher than the ideal ratio of 0.4. The reason for this is currently unclear, but the composition may be corroborated with other techniques, such as x-ray photoelectron spectroscopy and mass spectroscopy. The voltage profile of the NCA lattices, measured by cycling at C/40 and C/20 between 3 and 4.3 V, is shown in Figure 6.12(c), which reveals a sloping voltage with a sharp drop ~ 3.4 V on discharge and a first discharge specific capacity of 135 mAh/g. This profile is similar to the characteristic voltage profile of NCA, while the specific capacity of NCA can reach 200 mAh/g [191]. The lower capacity is likely due to similar reasons as the lower capacity from the LCO lattices, in addition to deviations from the ideal stoichiometry. The capability of photopolymer complex synthesis to fabricate efficient LIB electrodes out of more complicated oxides, such as NCA, is still currently under investigation.

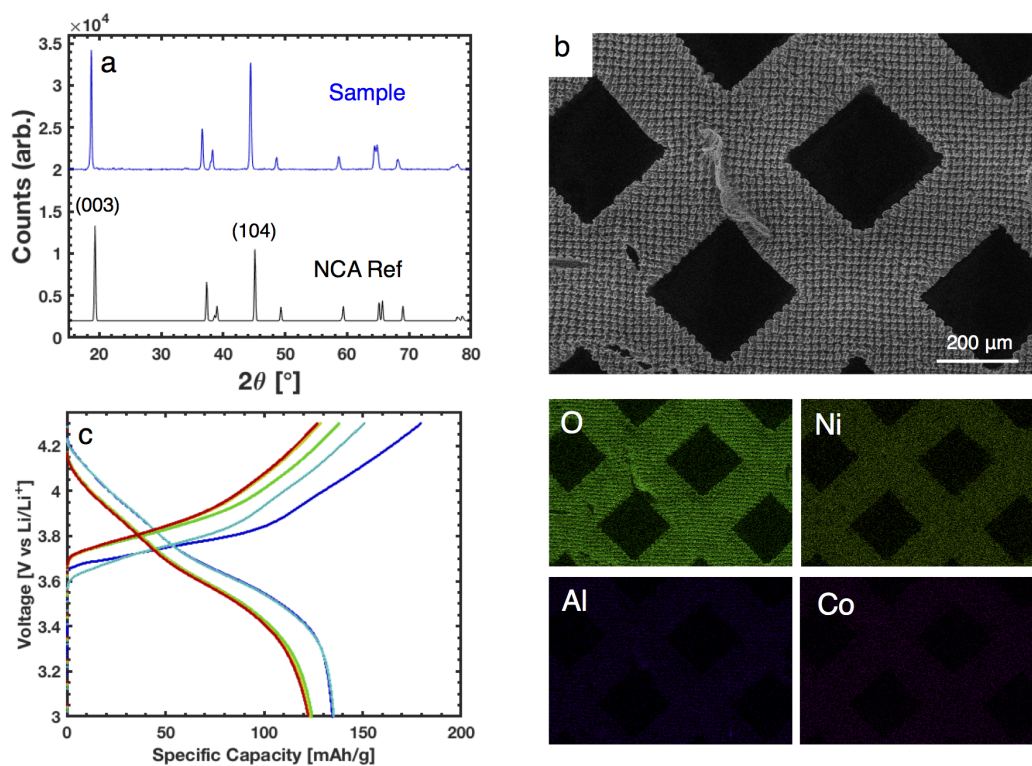


Figure 6.12: (a) XRD spectrum from a pulverized NCA lattice and reference spectrum taken from Reference [192]. (b) SEM image of the NCA lattice with elemental maps from EDS illustrating the four non-Li elements of NCA. (c) Voltage profile during charge at C/40 for 2 cycles and C/20 for cycles 3-5.

6.5 Conclusions

Free-standing architected 3D LCO electrodes were fabricated at coin cell dimensions using a novel photopolymer system with DLP 3D printing. Metal salts in the photopolymer resin were oxidized during calcination to create an architected oxide structure. The lattices were printed with ~ 120 μm beam diameters with overall (structural and microscale) porosities $\sim 80\%$. XRD, EDS, and CV all provide complimentary evidence that the lattices were indeed composed of LCO, with ~ 5 wt% of impurities. The LCO lattices exhibited gravimetric capacities of 122 mAh/g and areal capacities up to ~ 8 mAh/cm² with a capacity retention of 82% over 100 cycles. This represents a reasonable gravimetric capacity and cycle life with an areal capacity $\sim 2\times$ higher than conventional electrodes. The large variable space of this fabrication process could be optimized to improve the electrochemical properties of printed structures and can be adapted to manufacture architected 3D electrodes out of many other LIB-relevant materials, such as NCA. 3D architected cathodes such as those discussed in this chapter may eventually be utilized in Li solid-state

batteries with high energy and power densities.

Chapter 7

THESIS SUMMARY AND OUTLOOK

In this thesis, we investigated fundamental materials properties of Li metal, namely microstructure, modulus, and strength, as well as the growth of Li at the beginning of charge. These are important parameters that influence the operation of Li solid-state batteries. We also explored a new additive manufacturing method and its feasibility in creating architected LIB cathodes.

To explore these properties and processes, we developed an experimental set-up to charge thin film solid-state batteries composed of an LCO cathode, LiPON electrolyte, and Cu current collector, *in-situ* inside the SEM chamber. This instrumentation allowed for the direct observation of dynamic Li formation when the cell was charged and provided access to electrodeposited Li for nanomechanical experiments without exposure to air. The surface topography of the cell showed nodes or hills that arise from the underlying LCO layer, which form domains on the surface. While charging the cells, we observed that the Li first nucleated at the Cu/LiPON interface underneath the Cu, then punctured through the Cu layer to form a variety of morphologies, including fibers, pillars, and spheres. Li formed preferentially at the domain boundaries on the surface of the cell, which was corroborated with electrochemical simulations that showed the current density was enhanced at the cusps of the domain boundaries. These cusps also exhibited preferential growth of sphere-like Li, possibly because of increased potential gradients at these areas driving Li self-diffusion.

To investigate the microstructure of Li grown in these cells, we explored various techniques to probe Li using TEM while avoiding the problems of air exposure and beam sensitivity. *In-situ* TEM samples were fabricated from a cross-section of the cell using FIB lift out and guidance was provided to help fabricate a successful sample. Cryo-FIB was also endeavoured to directly transfer single Li fibers from the cell into the TEM. We explored cryo-EM and found it to be a successful method to investigate the microstructure of Li deposited from a solid-state battery by charging the cell connected to a TEM grid. The Li fibers that grew from the cell displayed a single crystalline microstructure, similar to that of Li deposited in a liquid electrolyte examined by cryo-EM.

In-situ charging experiments in the SEM chamber allowed for the transfer of Li into the SEM without air exposure. A small percentage of Li deposits grew into pillar morphologies and orientations that were favorable to perform uniaxial compression experiments. By performing experiments at constant loading rates instead of constant displacement rates, we were able to mitigate the noisy data produced from small sample loads. Uniaxial compression experiments revealed the moduli of these pillars closely matched those measured in the literature, validating the measured mechanical response. The single crystalline pillars, with diameters 360-759 nm, first deformed elastically, then plastically flowed with no visible slip offsets. The Li pillars exhibited yield strengths 24x higher than bulk polycrystalline Li with a large, 43% standard deviation. The deformation of the single crystalline pillars is likely governed by dislocation surface nucleation and thermally activated deformation processes.

Another route to improve the performance of Li based batteries is to utilize 3D battery electrodes to provide high energy and power. We investigated a novel additive manufacturing technique to fabricate 3D architected LCO structures. Dimensional transformations and morphology after calcining were investigated and related to the lack of mechanical robustness of these structures. XRD, EDS, CV, and electrochemical cycling were performed to establish that the material created was electrochemically active LCO. We developed a coin cell-stack design that can be used to electrochemically probe low toughness structures. The electrochemical performance of the LCO structures exhibited a relatively high areal capacity ~ 8 mAh/cm² with a capacity retention of 82% after 100 cycles. The performance is discussed in terms of the printed structure, microstructure, and porosity of the LCO lattices, and the constitutive material.

This thesis has explored some of the fundamental issues that need to be solved in order to successfully implement batteries with higher energy and power density with improved safety. Novel experiments were performed to characterize properties of Li metal that is formed under methods that are very relevant to the conditions of Li battery operation. This thesis also emphasizes the importance of size and fabrication conditions on the mechanical properties of Li. Researchers may need to direct more efforts on the mechanical response of electrodeposited Li due to its strong dependency on these two factors. The high strengths of Li measured in a commercial, thin film solid-state battery can hopefully assist researchers in designing solid electrolytes that can more effectively handle mechanical degradation

when used in a Li solid-state cell, as the strength of Li may be different from the bulk strength. Interest in Li mechanics has only recently emerged, and thus many questions remain, such as the effects of battery cycling under different conditions on the mechanical response of Li. In terms of electrode architecture, photopolymer complex synthesis is an intriguing fabrication method for 3D architected oxide cathode materials. The versatility of this method could be utilized to tune the material, structure, and dimensions produced by this technique. Ultimately in the future, some of the techniques and properties discussed here may be used to produce 3D, all solid-state Li metal batteries.

REFERENCES

- [1] C. Curry, "Lithium-ion battery costs and market," *Bloom. New Energy Finance*, vol. 5, 2017.
- [2] P. Albertus, S. Babinec, S. Litzelman, and A. Newman, "Status and challenges in enabling the lithium metal electrode for high-energy and low-cost rechargeable batteries," *Nat. Energy*, vol. 3, no. 1, p. 16, 2018.
- [3] Z. P. Cano, D. Banham, S. Ye, A. Hintennach, J. Lu, M. Fowler, and Z. Chen, "Batteries and fuel cells for emerging electric vehicle markets," *Nat. Energy*, vol. 3, no. 4, p. 279, 2018.
- [4] G. E. Blomgren, "The development and future of lithium ion batteries," *J. Electrochem. Soc.*, vol. 164, no. 1, pp. A5019–A5025, 2017.
- [5] B. Scrosati, "History of lithium batteries," *J. Solid State Electrochem.*, vol. 15, no. 7-8, pp. 1623–1630, 2011.
- [6] M. S. Whittingham, "Chemistry of intercalation compounds: Metal guests in chalcogenide hosts," *Prog. Solid State Chem.*, vol. 12, no. 1, pp. 41–99, 1978.
- [7] K. Mizushima, P. C. Jones, P. J. Wiseman, and J. B. Goodenough, " Li_xCoO_2 ($0 < x < 1$): A new cathode material for batteries of high energy density," *Mater. Res. Bull.*, vol. 15, no. 6, pp. 783–789, 1980.
- [8] R. Yazami and P. Touzain, "A reversible graphite-lithium negative electrode for electrochemical generators," *J. Power Sources*, vol. 9, no. 3, pp. 365–371, 1983.
- [9] A. Yoshino, K. Sanechika, and T. Nakajima, "Secondary battery," May 1987.
- [10] S. Flandrois and B. Simon, "Carbon materials for lithium-ion rechargeable batteries," *Carbon*, vol. 37, no. 2, pp. 165–180, 1999.
- [11] N. Nitta, F. Wu, J. T. Lee, and G. Yushin, "Li-ion battery materials: Present and future," *Mater. Today*, vol. 18, no. 5, pp. 252–264, 2015.
- [12] K. Xu, "Electrolytes and interphases in Li-ion batteries and beyond," *Chem. Rev.*, vol. 114, no. 23, pp. 11503–11618, 2014.
- [13] M. F. Lagadec, R. Zahn, and V. Wood, "Characterization and performance evaluation of lithium-ion battery separators," *Nat. Energy*, p. 1, 2018.
- [14] J. B. Goodenough and K.-S. Park, "The Li-ion rechargeable battery: A perspective," *J. Am. Chem. Soc.*, vol. 135, no. 4, pp. 1167–1176, 2013.

- [15] X. H. Liu, L. Zhong, L. Q. Zhang, A. Kushima, S. X. Mao, J. Li, Z. Z. Ye, J. P. Sullivan, and J. Y. Huang, "Lithium fiber growth on the anode in a nanowire lithium ion battery during charging," *Appl. Phys. Lett.*, vol. 98, no. 18, p. 183107, 2011.
- [16] T. B. Reddy, *Linden's Handbook of Batteries*, vol. 4. McGraw-hill New York, 2011.
- [17] J. Lee, A. Urban, X. Li, D. Su, G. Hautier, and G. Ceder, "Unlocking the potential of cation-disordered oxides for rechargeable lithium batteries," *Science*, vol. 343, no. 6170, pp. 519–522, 2014.
- [18] M. M. Thackeray, S.-H. Kang, C. S. Johnson, J. T. Vaughey, R. Benedek, and S. A. Hackney, "Li₂MnO₃-stabilized LiMO₂ (M= Mn, Ni, Co) electrodes for lithium-ion batteries," *J. Mater. Chem.*, vol. 17, no. 30, pp. 3112–3125, 2007.
- [19] H. Li, J. Pang, Y. Yin, W. Zhuang, H. Wang, C. Zhai, and S. Lu, "Application of a nonflammable electrolyte containing Pp13TFSI ionic liquid for lithium-ion batteries using the high capacity cathode material Li [Li 0.2 Mn 0.54 Ni 0.13 Co 0.13] O₂," *RSC Adv.*, vol. 3, no. 33, pp. 13907–13914, 2013.
- [20] A. Abouimrane, I. Belharouak, and K. Amine, "Sulfone-based electrolytes for high-voltage Li-ion batteries," *Electrochem. Commun.*, vol. 11, no. 5, pp. 1073–1076, 2009.
- [21] H. Wu and Y. Cui, "Designing nanostructured Si anodes for high energy lithium ion batteries," *Nano Today*, vol. 7, no. 5, pp. 414–429, 2012.
- [22] "Sila Nanotechnologies." <https://silanano.com/>.
- [23] "Nexeon | Building better batteries | Transformative silicon-based anode technology." <https://www.nexeon.co.uk/>.
- [24] W. Xu, J. Wang, F. Ding, X. Chen, E. Nasybulin, Y. Zhang, and J.-G. Zhang, "Lithium metal anodes for rechargeable batteries," *Energy Environ. Sci.*, vol. 7, no. 2, pp. 513–537, 2014.
- [25] D. Lin, Y. Liu, and Y. Cui, "Reviving the lithium metal anode for high-energy batteries," *Nat. Nanotechnol.*, vol. 12, no. 3, p. 194, 2017.
- [26] Z. Li, J. Huang, B. Y. Liaw, V. Metzler, and J. Zhang, "A review of lithium deposition in lithium-ion and lithium metal secondary batteries," *J. Power Sources*, vol. 254, pp. 168–182, 2014.
- [27] F. Orsini, A. Du Pasquier, B. Beaudoin, J. M. Tarascon, M. Trentin, N. Langenhuisen, E. De Beer, and P. Notten, "In situ scanning electron microscopy (SEM) observation of interfaces within plastic lithium batteries," *J. Power Sources*, vol. 76, no. 1, pp. 19–29, 1998.

- [28] M. D. Tikekar, S. Choudhury, Z. Tu, and L. A. Archer, "Design principles for electrolytes and interfaces for stable lithium-metal batteries," *Nat. Energy*, vol. 1, no. 9, p. 16114, 2016.
- [29] Y. Lu, Z. Tu, and L. A. Archer, "Stable lithium electrodeposition in liquid and nanoporous solid electrolytes," *Nat. Mater.*, vol. 13, no. 10, p. 961, 2014.
- [30] A. Zhamu, G. Chen, C. Liu, D. Neff, Q. Fang, Z. Yu, W. Xiong, Y. Wang, X. Wang, and B. Z. Jang, "Reviving rechargeable lithium metal batteries: Enabling next-generation high-energy and high-power cells," *Energy Env. Sci*, vol. 5, no. 2, pp. 5701–5707, 2012.
- [31] F. Ding, W. Xu, G. L. Graff, J. Zhang, M. L. Sushko, X. Chen, Y. Shao, M. H. Engelhard, Z. Nie, and J. Xiao, "Dendrite-free lithium deposition via self-healing electrostatic shield mechanism," *J. Am. Chem. Soc.*, vol. 135, no. 11, pp. 4450–4456, 2013.
- [32] H. Yang, E. O. Fey, B. D. Trimm, N. Dimitrov, and M. S. Whittingham, "Effects of Pulse Plating on lithium electrodeposition, morphology and cycling efficiency," *J. Power Sources*, vol. 272, pp. 900–908, Dec. 2014.
- [33] C. Monroe and J. Newman, "The impact of elastic deformation on deposition kinetics at lithium/polymer interfaces," *J. Electrochem. Soc.*, vol. 152, no. 2, pp. A396–A404, 2005.
- [34] A. Ferrese and J. Newman, "Mechanical deformation of a lithium-metal anode due to a very stiff separator," *J. Electrochem. Soc.*, vol. 161, no. 9, pp. A1350–A1359, 2014.
- [35] A. Manthiram, X. Yu, and S. Wang, "Lithium battery chemistries enabled by solid-state electrolytes," *Nat. Rev. Mater.*, vol. 2, no. 4, p. 16103, 2017.
- [36] F. Han, A. S. Westover, J. Yue, X. Fan, F. Wang, M. Chi, D. N. Leonard, N. J. Dudney, H. Wang, and C. Wang, "High electronic conductivity as the origin of lithium dendrite formation within solid electrolytes," *Nat. Energy*, vol. 4, no. 3, p. 187, 2019.
- [37] L. Porz, T. Swamy, B. W. Sheldon, D. Rettenwander, T. Frömling, H. L. Thaman, S. Berendts, R. Uecker, W. C. Carter, and Y.-M. Chiang, "Mechanism of lithium metal penetration through inorganic solid electrolytes," *Adv. Energy Mater.*, vol. 7, no. 20, p. 1701003, 2017.
- [38] J. A. Lewis, F. J. Q. Cortes, M. G. Boebinger, J. Tippens, T. S. Marchese, N. Kondekar, X. Liu, M. Chi, and M. T. McDowell, "Interphase morphology between a solid-state electrolyte and lithium controls cell failure," *ACS Energy Lett.*, vol. 4, no. 2, pp. 591–599, 2019.

- [39] J. Wolfenstine, H. Jo, Y.-H. Cho, I. N. David, P. Askeland, E. D. Case, H. Kim, H. Choe, and J. Sakamoto, "A preliminary investigation of fracture toughness of $\text{Li}_7\text{La}_3\text{Zr}_2\text{O}_{12}$ and its comparison to other solid li-ionconductors," *Mater. Lett.*, vol. 96, pp. 117–120, 2013.
- [40] C. Xu, Z. Ahmad, A. Aryanfar, V. Viswanathan, and J. R. Greer, "Enhanced strength and temperature dependence of mechanical properties of Li at small scales and its implications for Li metal anodes," *Proc. Natl. Acad. Sci.*, vol. 114, no. 1, pp. 57–61, 2017.
- [41] R. Liu, J. Duay, and S. B. Lee, "Heterogeneous nanostructured electrode materials for electrochemical energy storage," *Chem. Commun.*, vol. 47, no. 5, pp. 1384–1404, 2011.
- [42] N. Hansen, "Hall–Petch relation and boundary strengthening," *Scr. Mater.*, vol. 51, no. 8, pp. 801–806, 2004.
- [43] J. R. Greer and J. T. M. De Hosson, "Plasticity in small-sized metallic systems: Intrinsic versus extrinsic size effect," *Prog. Mater. Sci.*, vol. 56, no. 6, pp. 654–724, 2011.
- [44] H. Bei, S. Shim, E. P. George, M. K. Miller, E. G. Herbert, and G. M. Pharr, "Compressive strengths of molybdenum alloy micro-pillars prepared using a new technique," *Scr. Mater.*, vol. 57, no. 5, pp. 397–400, 2007.
- [45] B. Yang, C. Motz, M. Rester, and G. Dehm, "Yield stress influenced by the ratio of wire diameter to grain size—a competition between the effects of specimen microstructure and dimension in micro-sized polycrystalline copper wires," *Philos. Mag.*, vol. 92, no. 25-27, pp. 3243–3256, 2012.
- [46] X. W. Gu, C. N. Loynachan, Z. Wu, Y.-W. Zhang, D. J. Srolovitz, and J. R. Greer, "Size-dependent deformation of nanocrystalline Pt nanopillars," *Nano Lett.*, vol. 12, no. 12, pp. 6385–6392, 2012.
- [47] Z. H. Aitken, D. Jang, C. R. Weinberger, and J. R. Greer, "Grain Boundary Sliding in Aluminum Nano-Bi-Crystals Deformed at Room Temperature," *Small*, vol. 10, no. 1, pp. 100–108, 2014.
- [48] A. Kunz, S. Pathak, and J. R. Greer, "Size effects in Al nanopillars: Single crystalline vs. bicrystalline," *Acta Mater.*, vol. 59, no. 11, pp. 4416–4424, 2011.
- [49] M. D. Uchic, D. M. Dimiduk, J. N. Florando, and W. D. Nix, "Sample dimensions influence strength and crystal plasticity," *Science*, vol. 305, no. 5686, pp. 986–989, 2004.
- [50] J. R. Greer, W. C. Oliver, and W. D. Nix, "Size dependence of mechanical properties of gold at the micron scale in the absence of strain gradients," *Acta Mater.*, vol. 53, no. 6, pp. 1821–1830, 2005.

- [51] A. T. Jennings, M. J. Burek, and J. R. Greer, "Microstructure versus size: Mechanical properties of electroplated single crystalline Cu nanopillars," *Phys. Rev. Lett.*, vol. 104, no. 13, p. 135503, 2010.
- [52] J.-Y. Kim, D. Jang, and J. R. Greer, "Tensile and compressive behavior of tungsten, molybdenum, tantalum and niobium at the nanoscale," *Acta Mater.*, vol. 58, no. 7, pp. 2355–2363, 2010.
- [53] S. Min Han, G. Feng, J. Young Jung, H. Joon Jung, J. R. Groves, W. D. Nix, and Y. Cui, "Critical-temperature/Peierls-stress dependent size effects in body centered cubic nanopillars," *Appl. Phys. Lett.*, vol. 102, no. 4, p. 041910, 2013.
- [54] A. S. Schneider, D. Kaufmann, B. G. Clark, C. P. Frick, P. A. Gruber, R. Mönig, O. Kraft, and E. Arzt, "Correlation between critical temperature and strength of small-scale bcc pillars," *Phys. Rev. Lett.*, vol. 103, no. 10, p. 105501, 2009.
- [55] J. R. Greer and W. D. Nix, "Nanoscale gold pillars strengthened through dislocation starvation," *Phys. Rev. B*, vol. 73, no. 24, p. 245410, 2006.
- [56] S. Tariq, K. Ammigan, P. Hurh, R. Schultz, P. Liu, and J. Shang, "Li material testing-fermilab antiproton source lithium collection lens," in *Proceedings of the 2003 Particle Accelerator Conference*, vol. 3, pp. 1452–1454, IEEE, 2003.
- [57] Z. Ahmad and V. Viswanathan, "Stability of electrodeposition at solid-solid interfaces and implications for metal anodes," *Phys. Rev. Lett.*, vol. 119, no. 5, p. 056003, 2017.
- [58] P. Wang, W. Qu, W.-L. Song, H. Chen, R. Chen, and D. Fang, "Electro-Chemo-Mechanical Issues at the Interfaces in Solid-State Lithium Metal Batteries," *Adv. Funct. Mater.*, p. 1900950, 2019.
- [59] F. P. McGrogan, T. Swamy, S. R. Bishop, E. Eggleton, L. Porz, X. Chen, Y.-M. Chiang, and K. J. Van Vliet, "Compliant Yet Brittle Mechanical Behavior of Li₂S–P₂S₅ Lithium-Ion-Conducting Solid Electrolyte," *Adv. Energy Mater.*, vol. 7, no. 12, p. 1602011, 2017.
- [60] M. J. Wang, R. Choudhury, and J. Sakamoto, "Characterizing the Li-Solid-Electrolyte Interface Dynamics as a Function of Stack Pressure and Current Density," *Joule*, 2019.
- [61] Y. Ren, Y. Shen, Y. Lin, and C.-W. Nan, "Direct observation of lithium dendrites inside garnet-type lithium-ion solid electrolyte," *Electrochem. Commun.*, vol. 57, pp. 27–30, 2015.
- [62] E. J. Cheng, A. Sharafi, and J. Sakamoto, "Intergranular Li metal propagation through polycrystalline Li₆.₂₅Al_{0.25}La₃Zr₂O₁₂ ceramic electrolyte," *Electrochimica Acta*, vol. 223, pp. 85–91, 2017.

- [63] J. Tippens, J. Miers, A. Afshar, J. Lewis, F. J. Q. Cortes, H. Qiao, T. S. Marchese, C. V. Di Leo, C. Saldana, and M. T. McDowell, “Visualizing Chemo-Mechanical Degradation of a Solid-State Battery Electrolyte,” *ACS Energy Lett.*, 2019.
- [64] E. G. Herbert, S. A. Hackney, V. Thole, N. J. Dudney, and P. S. Phani, “Nanoindentation of high-purity vapor deposited lithium films: A mechanistic rationalization of diffusion-mediated flow,” *J. Mater. Res.*, vol. 33, no. 10, pp. 1347–1360, 2018.
- [65] E. G. Herbert, S. A. Hackney, V. Thole, N. J. Dudney, and P. S. Phani, “Nanoindentation of high-purity vapor deposited lithium films: A mechanistic rationalization of the transition from diffusion to dislocation-mediated flow,” *J. Mater. Res.*, vol. 33, no. 10, pp. 1361–1368, 2018.
- [66] A. Masias, N. Felten, R. Garcia-Mendez, J. Wolfenstine, and J. Sakamoto, “Elastic, plastic, and creep mechanical properties of lithium metal,” *J. Mater. Sci.*, vol. 54, no. 3, pp. 2585–2600, 2019.
- [67] Y. Wang and Y.-T. Cheng, “A nanoindentation study of the viscoplastic behavior of pure lithium,” *Scr. Mater.*, vol. 130, pp. 191–195, 2017.
- [68] S. Narayan and L. Anand, “A large deformation elastic–viscoplastic model for lithium,” *Extreme Mech. Lett.*, vol. 24, pp. 21–29, 2018.
- [69] W. S. LePage, Y. Chen, E. Kazyak, K.-H. Chen, A. J. Sanchez, A. Poli, E. M. Arruda, M. D. Thouless, and N. P. Dasgupta, “Lithium Mechanics: Roles of Strain Rate and Temperature and Implications for Lithium Metal Batteries,” *J. Electrochem. Soc.*, vol. 166, no. 2, pp. A89–A97, 2019.
- [70] D. Hull and H. M. Rosenberg, “The deformation of lithium, sodium and potassium at low temperatures: Tensile and resistivity experiments,” *Philos. Mag.*, vol. 4, no. 39, pp. 303–315, 1959.
- [71] R. P. Schultz, “Lithium: Measurement of Young’s Modulus and Yield Strength,” tech. rep., Fermi National Accelerator Lab., Batavia, IL (US), 2002.
- [72] M. Motoyama, M. Ejiri, and Y. Iriyama, “Modeling the nucleation and growth of Li at metal current collector/LiPON interfaces,” *J. Electrochem. Soc.*, vol. 162, no. 13, pp. A7067–A7071, 2015.
- [73] E. G. Herbert, S. A. Hackney, N. J. Dudney, and P. S. Phani, “Nanoindentation of high-purity vapor deposited lithium films: The elastic modulus,” *J. Mater. Res.*, vol. 33, no. 10, pp. 1335–1346, 2018.
- [74] P. Zhang, S. X. Li, and Z. F. Zhang, “General relationship between strength and hardness,” *Mater. Sci. Eng. A*, vol. 529, pp. 62–73, 2011.

- [75] J. B. Bates, N. J. Dudney, G. R. Gruzalski, R. A. Zuhr, A. Choudhury, C. F. Luck, and J. D. Robertson, "Fabrication and characterization of amorphous lithium electrolyte thin films and rechargeable thin-film batteries," *J. Power Sources*, vol. 43, no. 1-3, pp. 103–110, 1993.
- [76] N. J. Dudney, "Solid-state thin-film rechargeable batteries," *Mater. Sci. Eng. B*, vol. 116, no. 3, pp. 245–249, 2005.
- [77] J. B. Bates, N. J. Dudney, B. Neudecker, A. Ueda, and C. D. Evans, "Thin-film lithium and lithium-ion batteries," *Solid State Ion.*, vol. 135, no. 1-4, pp. 33–45, 2000.
- [78] J. Li, C. Ma, M. Chi, C. Liang, and N. J. Dudney, "Solid electrolyte: The key for high-voltage lithium batteries," *Adv. Energy Mater.*, vol. 5, no. 4, p. 1401408, 2015.
- [79] B. J. Neudecker, N. J. Dudney, and J. B. Bates, "'Lithium-free' thin-film battery with in situ plated Li anode," *J. Electrochem. Soc.*, vol. 147, no. 2, pp. 517–523, 2000.
- [80] "Front Edge Technology, Inc - Home Page." <http://frontedgetechnology.com/>.
- [81] V. Krasnov, K.-W. Nieh, and S.-J. Ting, "Method of manufacturing a thin film battery," July 2005.
- [82] V. Krasnov, K.-W. Nieh, and J. Li, "Thin film battery and manufacturing method," Jan. 2011.
- [83] X. Qian, N. Gu, Z. Cheng, X. Yang, E. Wang, and S. Dong, "Methods to study the ionic conductivity of polymeric electrolytes using ac impedance spectroscopy," *J. Solid State Electrochem.*, vol. 6, no. 1, pp. 8–15, 2001.
- [84] C. Wang and J. Hong, "Ionic/electronic conducting characteristics of Lifepo4 cathode materials the determining factors for high rate performance," *Electrochem. Solid-State Lett.*, vol. 10, no. 3, pp. A65–A69, 2007.
- [85] "Chemical Analysis, Life Sciences, and Diagnostics | Agilent." <https://www.agilent.com/>.
- [86] D. Kiener, C. Motz, M. Rester, M. Jenko, and G. Dehm, "FIB damage of Cu and possible consequences for miniaturized mechanical tests," *Mater. Sci. Eng. A*, vol. 459, no. 1-2, pp. 262–272, 2007.
- [87] C. Multiphysics, V. 5.2 a. *Www. Comsol. Com. COMSOL AB, Stockholm. Sweden*, 2018.
- [88] Y. Hamon, A. Douard, F. Sabary, C. Marcel, P. Vinatier, B. Pecquenard, and A. Levasseur, "Influence of sputtering conditions on ionic conductivity of LiPON thin films," *Solid State Ion.*, vol. 177, no. 3-4, pp. 257–261, 2006.

- [89] J. Schwenzel, V. Thangadurai, and W. Weppner, "Investigation of thin film all-solid-state lithium ion battery materials," *Ionics*, vol. 9, no. 5-6, pp. 348–356, 2003.
- [90] E. Dologlou, "Self-diffusion in solid lithium," *Glass Phys. Chem.*, vol. 36, no. 5, pp. 570–574, 2010.
- [91] J. Qian, W. A. Henderson, W. Xu, P. Bhattacharya, M. Engelhard, O. Borodin, and J.-G. Zhang, "High rate and stable cycling of lithium metal anode," *Nat. Commun.*, vol. 6, p. 6362, 2015.
- [92] Y. Li, Y. Li, A. Pei, K. Yan, Y. Sun, C.-L. Wu, L.-M. Joubert, R. Chin, A. L. Koh, and Y. Yu, "Atomic structure of sensitive battery materials and interfaces revealed by cryo-electron microscopy," *Science*, vol. 358, no. 6362, pp. 506–510, 2017.
- [93] F. Wang, J. Graetz, M. S. Moreno, C. Ma, L. Wu, V. Volkov, and Y. Zhu, "Chemical distribution and bonding of lithium in intercalated graphite: Identification with optimized electron energy loss spectroscopy," *Acs Nano*, vol. 5, no. 2, pp. 1190–1197, 2011.
- [94] D.-R. Lru and D. B. Williams, "The electron-energy-loss spectrum of lithium metal," *Philos. Mag. B*, vol. 53, no. 6, pp. L123–L128, 1986.
- [95] B. L. Mehdi, J. Qian, E. Nasybulin, C. Park, D. A. Welch, R. Faller, H. Mehta, W. A. Henderson, W. Xu, and C. M. Wang, "Observation and quantification of nanoscale processes in lithium batteries by operando electrochemical (S) TEM," *Nano Lett.*, vol. 15, no. 3, pp. 2168–2173, 2015.
- [96] X. Wang, M. Zhang, J. Alvarado, S. Wang, M. Sina, B. Lu, J. Bouwer, W. Xu, J. Xiao, and J.-G. Zhang, "New insights on the structure of electrochemically deposited lithium metal and its solid electrolyte interphases via cryogenic TEM," *Nano Lett.*, vol. 17, no. 12, pp. 7606–7612, 2017.
- [97] Z. Wang, D. Santhanagopalan, W. Zhang, F. Wang, H. L. Xin, K. He, J. Li, N. Dudney, and Y. S. Meng, "In situ STEM-EELS observation of nanoscale interfacial phenomena in all-solid-state batteries," *Nano Lett.*, vol. 16, no. 6, pp. 3760–3767, 2016.
- [98] M. Hammad Fawey, V. S. K. Chakravadhanula, M. A. Reddy, C. Rongeat, T. Scherer, H. Hahn, M. Fichtner, and C. Kübel, "In situ TEM studies of micron-sized all-solid-state fluoride ion batteries: Preparation, prospects, and challenges," *Microsc. Res. Tech.*, vol. 79, no. 7, pp. 615–624, 2016.
- [99] "TEM Sample Holder Supports & Solutions: E-Chips | Protochips." <https://www.protochips.com/products/e-chips/>.

- [100] M. J. Zachman, E. Asenath-Smith, L. A. Estroff, and L. F. Kourkoutis, “Site-specific preparation of intact solid–liquid interfaces by label-free in situ localization and cryo-focused ion beam lift-out,” *Microsc. Microanal.*, vol. 22, no. 6, pp. 1338–1349, 2016.
- [101] M. M. Beg and M. Nielsen, “Temperature dependence of lattice dynamics of lithium 7,” *Phys. Rev. B*, vol. 14, no. 10, p. 4266, 1976.
- [102] L. Vitos, A. V. Ruban, H. L. Skriver, and J. Kollar, “The surface energy of metals,” *Surf. Sci.*, vol. 411, no. 1-2, pp. 186–202, 1998.
- [103] S.-W. Lee, S. M. Han, and W. D. Nix, “Uniaxial compression of fcc Au nanopillars on an MgO substrate: The effects of prestraining and annealing,” *Acta Mater.*, vol. 57, no. 15, pp. 4404–4415, 2009.
- [104] G. Lee, J.-Y. Kim, M. J. Burek, J. R. Greer, and T. Y. Tsui, “Plastic deformation of indium nanostructures,” *Mater. Sci. Eng. A*, vol. 528, no. 19-20, pp. 6112–6120, 2011.
- [105] M. J. Burek, A. S. Budiman, Z. Jahed, N. Tamura, M. Kunz, S. Jin, S. M. J. Han, G. Lee, C. Zamecnik, and T. Y. Tsui, “Fabrication, microstructure, and mechanical properties of tin nanostructures,” *Mater. Sci. Eng. A*, vol. 528, no. 18, pp. 5822–5832, 2011.
- [106] L.-W. Ji, S.-J. Young, T.-H. Fang, and C.-H. Liu, “Buckling characterization of vertical ZnO nanowires using nanoindentation,” *Appl. Phys. Lett.*, vol. 90, no. 3, p. 033109, 2007.
- [107] N. Friedman, A. T. Jennings, G. Tsekenis, J.-Y. Kim, M. Tao, J. T. Uhl, J. R. Greer, and K. A. Dahmen, “Statistics of dislocation slip avalanches in nanosized single crystals show tuned critical behavior predicted by a simple mean field model,” *Phys. Rev. Lett.*, vol. 109, no. 9, p. 095507, 2012.
- [108] X. Ni, H. Zhang, D. B. Liarte, L. W. McFaul, K. A. Dahmen, J. P. Sethna, and J. R. Greer, “Yield precursor dislocation avalanches in small crystals: The irreversibility transition,” *Phys. Rev. Lett.*, vol. 123, no. 3, p. 035501, 2019.
- [109] I. N. Sneddon, “The relation between load and penetration in the axisymmetric Boussinesq problem for a punch of arbitrary profile,” *Int. J. Eng. Sci.*, vol. 3, no. 1, pp. 47–57, 1965.
- [110] E. G. Herbert, W. E. Tenhaeff, N. J. Dudney, and G. M. Pharr, “Mechanical characterization of LiPON films using nanoindentation,” *Thin Solid Films*, vol. 520, no. 1, pp. 413–418, 2011.
- [111] T. Slotwinski and J. Trivisonno, “Temperature dependence of the elastic constants of single crystal lithium,” *J. Phys. Chem. Solids*, vol. 30, no. 5, pp. 1276–1278, 1969.

- [112] P. S. Phani, K. E. Johanns, G. Duscher, A. Gali, E. P. George, and G. M. Pharr, "Scanning transmission electron microscope observations of defects in as-grown and pre-strained Mo alloy fibers," *Acta Mater.*, vol. 59, no. 5, pp. 2172–2179, 2011.
- [113] K. E. Johanns, A. Sedlmayr, P. S. Phani, R. Mönig, O. Kraft, E. P. George, and G. M. Pharr, "In-situ tensile testing of single-crystal molybdenum-alloy fibers with various dislocation densities in a scanning electron microscope," *J. Mater. Res.*, vol. 27, no. 3, pp. 508–520, 2012.
- [114] H. Bei, S. Shim, G. M. Pharr, and E. P. George, "Effects of pre-strain on the compressive stress–strain response of Mo-alloy single-crystal micropillars," *Acta Mater.*, vol. 56, no. 17, pp. 4762–4770, 2008.
- [115] C. R. Krenn, D. Roundy, J. W. Morris Jr, and M. L. Cohen, "Ideal strengths of bcc metals," *Mater. Sci. Eng. A*, vol. 319, pp. 111–114, 2001.
- [116] M. J. Burek and J. R. Greer, "Fabrication and microstructure control of nanoscale mechanical testing specimens via electron beam lithography and electroplating," *Nano Lett.*, vol. 10, no. 1, pp. 69–76, 2009.
- [117] Q. Xiao, L. Huang, and Y. Shi, "Suppression of shear banding in amorphous ZrCuAl nanopillars by irradiation," *J. Appl. Phys.*, vol. 113, no. 8, p. 083514, 2013.
- [118] D. J. Magagnosc, G. Kumar, J. Schroers, P. Felfer, J. M. Cairney, and D. S. Gianola, "Effect of ion irradiation on tensile ductility, strength and fictive temperature in metallic glass nanowires," *Acta Mater.*, vol. 74, pp. 165–182, 2014.
- [119] D. Z. Chen, X. W. Gu, Q. An, W. A. Goddard III, and J. R. Greer, "Ductility and work hardening in nano-sized metallic glasses," *Appl. Phys. Lett.*, vol. 106, no. 6, p. 061903, 2015.
- [120] J. Saint, M. Morcrette, D. Larcher, and J. M. Tarascon, "Exploring the Li–Ga room temperature phase diagram and the electrochemical performances of the Li_xGa_y alloys vs. Li," *Solid State Ion.*, vol. 176, no. 1-2, pp. 189–197, 2005.
- [121] A. T. Jennings, C. Gross, F. Greer, Z. H. Aitken, S.-W. Lee, C. R. Weinberger, and J. R. Greer, "Higher compressive strengths and the Bauschinger effect in conformally passivated copper nanopillars," *Acta Mater.*, vol. 60, no. 8, pp. 3444–3455, 2012.
- [122] T. Zhu, J. Li, A. Samanta, A. Leach, and K. Gall, "Temperature and strain-rate dependence of surface dislocation nucleation," *Phys. Rev. Lett.*, vol. 100, no. 2, p. 025502, 2008.

- [123] A. T. Jennings, J. Li, and J. R. Greer, “Emergence of strain-rate sensitivity in Cu nanopillars: Transition from dislocation multiplication to dislocation nucleation,” *Acta Mater.*, vol. 59, no. 14, pp. 5627–5637, 2011.
- [124] W. Cai and V. V. Bulatov, “Mobility laws in dislocation dynamics simulations,” *Mater. Sci. Eng. A*, vol. 387, pp. 277–281, 2004.
- [125] A. Ishizaka and T. Doi, “Systematic change in surface structures on Si (111) clean surfaces with temperature,” *Philos. Mag. Lett.*, vol. 65, no. 2, pp. 95–100, 1992.
- [126] G. Richter, K. Hillerich, D. S. Gianola, R. Monig, O. Kraft, and C. A. Volkert, “Ultrahigh strength single crystalline nanowhiskers grown by physical vapor deposition,” *Nano Lett.*, vol. 9, no. 8, pp. 3048–3052, 2009.
- [127] A. Gangulee, “The structure of electroplated and vapor-deposited copper films,” *J. Appl. Phys.*, vol. 43, no. 3, pp. 867–873, 1972.
- [128] M. Hommel and O. Kraft, “Deformation behavior of thin copper films on deformable substrates,” *Acta Mater.*, vol. 49, no. 19, pp. 3935–3947, 2001.
- [129] S. Ferrari, M. Loveridge, S. D. Beattie, M. Jahn, R. J. Dashwood, and R. Bhagat, “Latest advances in the manufacturing of 3D rechargeable lithium microbatteries,” *J. Power Sources*, vol. 286, pp. 25–46, 2015.
- [130] M. Roberts, P. Johns, J. Owen, D. Brandell, K. Edstrom, G. El Enany, C. Guery, D. Golodnitsky, M. Lacey, and C. Lecoeur, “3D lithium ion batteries—from fundamentals to fabrication,” *J. Mater. Chem.*, vol. 21, no. 27, pp. 9876–9890, 2011.
- [131] T. S. Arthur, D. J. Bates, N. Cirigliano, D. C. Johnson, P. Malati, J. M. Mosby, E. Perre, M. T. Rawls, A. L. Prieto, and B. Dunn, “Three-dimensional electrodes and battery architectures,” *Mrs Bull.*, vol. 36, no. 7, pp. 523–531, 2011.
- [132] J. F. Oudenhoven, L. Baggetto, and P. H. Notten, “All-solid-state lithium-ion microbatteries: A review of various three-dimensional concepts,” *Adv. Energy Mater.*, vol. 1, no. 1, pp. 10–33, 2011.
- [133] T. Wierzbicki and E. Sahraei, “Homogenized mechanical properties for the jellyroll of cylindrical Lithium-ion cells,” *J. Power Sources*, vol. 241, pp. 467–476, 2013.
- [134] N. Cirigliano, G. Sun, D. Membreno, P. Malati, C. J. Kim, and B. Dunn, “3D Architected Anodes for Lithium-Ion Microbatteries with Large Areal Capacity,” *Energy Technol.*, vol. 2, no. 4, pp. 362–369, 2014.
- [135] S. R. Gowda, A. Leela Mohana Reddy, X. Zhan, H. R. Jafry, and P. M. Ajayan, “3D nanoporous nanowire current collectors for thin film microbatteries,” *Nano Lett.*, vol. 12, no. 3, pp. 1198–1202, 2012.

- [136] F. Chamran, Y. Yeh, H.-S. Min, B. Dunn, and C.-J. Kim, "Fabrication of high-aspect-ratio electrode arrays for three-dimensional microbatteries," *J. Microelectromechanical Syst.*, vol. 16, no. 4, pp. 844–852, 2007.
- [137] C. R. Sides, N. Li, C. J. Patrissi, B. Scrosati, and C. R. Martin, "Nanoscale materials for lithium-ion batteries," *Mrs Bull.*, vol. 27, no. 8, pp. 604–607, 2002.
- [138] M. Nishizawa, K. Mukai, S. Kuwabata, C. R. Martin, and H. Yoneyama, "Template Synthesis of Polypyrrole-Coated Spinel LiMn_2O_4 Nanotubules and Their Properties as Cathode Active Materials for Lithium Batteries," *J. Electrochem. Soc.*, vol. 144, no. 6, pp. 1923–1927, 1997.
- [139] M. M. Shaijumon, E. Perre, B. Daffos, P.-L. Taberna, J.-M. Tarascon, and P. Simon, "Nanoarchitected 3D cathodes for Li-Ion microbatteries," *Adv. Mater.*, vol. 22, no. 44, pp. 4978–4981, 2010.
- [140] E. Perre, P. L. Taberna, D. Mazouzi, P. Poizot, T. Gustafsson, K. Edström, and P. Simon, "Electrodeposited Cu_2Sb as anode material for 3-dimensional Li-ion microbatteries," *J. Mater. Res.*, vol. 25, no. 8, pp. 1485–1491, 2010.
- [141] C. K. Chan, H. Peng, G. Liu, K. McIlwrath, X. F. Zhang, R. A. Huggins, and Y. Cui, "High-performance lithium battery anodes using silicon nanowires," *Nat. Nanotechnol.*, vol. 3, no. 1, p. 31, 2008.
- [142] J. Zhu, J. Jiang, Y. Feng, G. Meng, H. Ding, and X. Huang, "Three-Dimensional Ni/SnO_x/C Hybrid Nanostructured Arrays for Lithium-Ion Microbattery Anodes with Enhanced Areal Capacity," *ACS Appl. Mater. Interfaces*, vol. 5, no. 7, pp. 2634–2640, 2013.
- [143] A. Izumi, M. Sanada, K. Furuichi, K. Teraki, T. Matsuda, K. Hiramatsu, H. Munakata, and K. Kanamura, "Development of high capacity lithium-ion battery applying three-dimensionally patterned electrode," *Electrochimica Acta*, vol. 79, pp. 218–222, 2012.
- [144] J. Li, M. C. Leu, R. Panat, and J. Park, "A hybrid three-dimensionally structured electrode for lithium-ion batteries via 3D printing," *Mater. Des.*, vol. 119, pp. 417–424, 2017.
- [145] K. Yoshima, H. Munakata, and K. Kanamura, "Fabrication of micro lithium-ion battery with 3D anode and 3D cathode by using polymer wall," *J. Power Sources*, vol. 208, pp. 404–408, 2012.
- [146] J. H. Pikul, H. G. Zhang, J. Cho, P. V. Braun, and W. P. King, "High-power lithium ion microbatteries from interdigitated three-dimensional bicontinuous nanoporous electrodes," *Nat. Commun.*, vol. 4, p. 1732, 2013.

- [147] K. Dokko, J.-i. Sugaya, H. Nakano, T. Yasukawa, T. Matsue, and K. Kanamura, "Sol-gel fabrication of lithium-ion microarray battery," *Electrochem. Commun.*, vol. 9, no. 5, pp. 857–862, 2007.
- [148] K. Sun, T.-S. Wei, B. Y. Ahn, J. Y. Seo, S. J. Dillon, and J. A. Lewis, "3D printing of interdigitated Li-Ion microbattery architectures," *Adv. Mater.*, vol. 25, no. 33, pp. 4539–4543, 2013.
- [149] J. G. Werner, G. G. Rodríguez-Calero, H. D. Abruña, and U. Wiesner, "Block copolymer derived 3-D interpenetrating multifunctional gyroidal nanohybrids for electrical energy storage," *Energy Environ. Sci.*, vol. 11, no. 5, pp. 1261–1270, 2018.
- [150] C. Liu, E. I. Gillette, X. Chen, A. J. Pearse, A. C. Kozen, M. A. Schroeder, K. E. Gregorczyk, S. B. Lee, and G. W. Rubloff, "An all-in-one nanopore battery array," *Nat. Nanotechnol.*, vol. 9, no. 12, p. 1031, 2014.
- [151] S. Chabi, C. Peng, D. Hu, and Y. Zhu, "Ideal three-dimensional electrode structures for electrochemical energy storage," *Adv. Mater.*, vol. 26, no. 15, pp. 2440–2445, 2014.
- [152] Y. Xu, M. Zhou, L. Wen, C. Wang, H. Zhao, Y. Mi, L. Liang, Q. Fu, M. Wu, and Y. Lei, "Highly ordered three-dimensional Ni-TiO₂ nanoarrays as sodium ion battery anodes," *Chem. Mater.*, vol. 27, no. 12, pp. 4274–4280, 2015.
- [153] H. N. Wadley, N. A. Fleck, and A. G. Evans, "Fabrication and structural performance of periodic cellular metal sandwich structures," *Compos. Sci. Technol.*, vol. 63, no. 16, pp. 2331–2343, 2003.
- [154] H. Zhang, H. Ning, J. Busbee, Z. Shen, C. Kiggins, Y. Hua, J. Eaves, J. Davis, T. Shi, and Y.-T. Shao, "Electroplating lithium transition metal oxides," *Sci. Adv.*, vol. 3, no. 5, p. e1602427, 2017.
- [155] P. Johns, M. Roberts, and J. Owen, "Conformal electrodeposition of manganese dioxide onto reticulated vitreous carbon for 3D microbattery applications," *J. Mater. Chem.*, vol. 21, no. 27, pp. 10153–10159, 2011.
- [156] G. F. Yang, J. S. Song, H. Y. Kim, and S. K. Joo, "Metal foam as positive electrode current collector for LiFePO₄-based Li-ion battery," *Jpn. J. Appl. Phys.*, vol. 52, no. 10S, p. 10MB13, 2013.
- [157] K. T. Lee, J. C. Lytle, N. S. Ergang, S. M. Oh, and A. Stein, "Synthesis and rate performance of monolithic macroporous carbon electrodes for lithium-ion secondary batteries," *Adv. Funct. Mater.*, vol. 15, no. 4, pp. 547–556, 2005.
- [158] M. S. Saleh, J. Li, J. Park, and R. Panat, "3D printed hierarchically-porous microlattice electrode materials for exceptionally high specific capacity and areal capacity lithium ion batteries," *Addit. Manuf.*, vol. 23, pp. 70–78, 2018.

- [159] T.-S. Wei, B. Y. Ahn, J. Grotto, and J. A. Lewis, "3D printing of customized li-ion batteries with thick electrodes," *Adv. Mater.*, vol. 30, no. 16, p. 1703027, 2018.
- [160] C. W. Foster, M. P. Down, Y. Zhang, X. Ji, S. J. Rowley-Neale, G. C. Smith, P. J. Kelly, and C. E. Banks, "3D printed graphene based energy storage devices," *Sci. Rep.*, vol. 7, p. 42233, 2017.
- [161] K. Fu, Y. Wang, C. Yan, Y. Yao, Y. Chen, J. Dai, S. Lacey, Y. Wang, J. Wan, and T. Li, "Graphene oxide-based electrode inks for 3D-printed lithium-ion batteries," *Adv. Mater.*, vol. 28, no. 13, pp. 2587–2594, 2016.
- [162] J. Hu, Y. Jiang, S. Cui, Y. Duan, T. Liu, H. Guo, L. Lin, Y. Lin, J. Zheng, and K. Amine, "3D-printed cathodes of LiMn_{1-x}FexPO₄ nanocrystals achieve both ultrahigh rate and high capacity for advanced lithium-ion battery," *Adv. Energy Mater.*, vol. 6, no. 18, p. 1600856, 2016.
- [163] C. Reyes, R. Somogyi, S. Niu, M. A. Cruz, F. Yang, M. J. Catenacci, C. P. Rhodes, and B. J. Wiley, "Three-dimensional printing of a complete lithium ion battery with fused filament fabrication," *ACS Appl. Energy Mater.*, vol. 1, no. 10, pp. 5268–5279, 2018.
- [164] Z. Chen, Z. Li, J. Li, C. Liu, C. Liu, Y. Li, P. Wang, H. Yi, C. Lao, and F. Yuelong, "3D printing of ceramics: A review," *J. Eur. Ceram. Soc.*, 2018.
- [165] A. Zocca, C. M. Gomes, A. Staude, E. Bernardo, J. Günster, and P. Colombo, "SiOC ceramics with ordered porosity by 3D-printing of a preceramic polymer," *J. Mater. Res.*, vol. 28, no. 17, pp. 2243–2252, 2013.
- [166] D. W. Yee, M. L. Lifson, B. W. Edwards, and J. R. Greer, "Additive Manufacturing of 3D-Architected Multifunctional Metal Oxides," *Adv. Mater.*, p. 1901345, 2019.
- [167] A. C. Kozen, A. J. Pearse, C.-F. Lin, M. Noked, and G. W. Rubloff, "Atomic layer deposition of the solid electrolyte LiPON," *Chem. Mater.*, vol. 27, no. 15, pp. 5324–5331, 2015.
- [168] M. Nisula, Y. Shindo, H. Koga, and M. Karppinen, "Atomic layer deposition of lithium phosphorus oxynitride," *Chem. Mater.*, vol. 27, no. 20, pp. 6987–6993, 2015.
- [169] C. P. Rhodes, J. W. Long, M. S. Doescher, J. J. Fontanella, and D. R. Rolison, "Nanoscale polymer electrolytes: Ultrathin electrodeposited poly (phenylene oxide) with solid-state ionic conductivity," *J. Phys. Chem. B*, vol. 108, no. 35, pp. 13079–13087, 2004.
- [170] S. R. Gowda, A. L. M. Reddy, M. M. Shaijumon, X. Zhan, L. Ci, and P. M. Ajayan, "Conformal coating of thin polymer electrolyte layer on nanostructured electrode materials for three-dimensional battery applications," *Nano Lett.*, vol. 11, no. 1, pp. 101–106, 2010.

- [171] M. Jo, Y.-S. Hong, J. Choo, and J. Cho, "Effect of LiCoO₂ cathode nanoparticle size on high rate performance for Li-ion batteries," *J. Electrochem. Soc.*, vol. 156, no. 6, pp. A430–A434, 2009.
- [172] A. Varma, A. S. Mukasyan, A. S. Rogachev, and K. V. Manukyan, "Solution combustion synthesis of nanoscale materials," *Chem. Rev.*, vol. 116, no. 23, pp. 14493–14586, 2016.
- [173] F. Saidi, Y. Bernabé, and T. Reuschle, "The mechanical behaviour of synthetic, poorly consolidated granular rock under uniaxial compression," *Tectonophysics*, vol. 370, no. 1-4, pp. 105–120, 2003.
- [174] C. M. Portela, J. R. Greer, and D. M. Kochmann, "Impact of node geometry on the effective stiffness of non-slender three-dimensional truss lattice architectures," *Extreme Mech. Lett.*, vol. 22, pp. 138–148, 2018.
- [175] B. Lawn, *Fracture of Brittle Solids*. Cambridge university press, 1993.
- [176] J. Cho, C.-S. Kim, and S.-I. Yoo, "Improvement of structural stability of LiCoO₂ cathode during electrochemical cycling by sol-gel coating of SnO₂," *Electrochem. Solid-State Lett.*, vol. 3, no. 8, pp. 362–365, 2000.
- [177] J. Akimoto, Y. Gotoh, and Y. Oosawa, "Synthesis and structure refinement of LiCoO₂ Single crystals," *Solid State Chem.*, vol. 141, pp. 298–302, 1998.
- [178] M. S. Whittingham, "Lithium batteries and cathode materials," *Chem. Rev.*, vol. 104, no. 10, pp. 4271–4302, 2004.
- [179] S. Burgess, X. Li, and J. Holland, "High spatial resolution energy dispersive X-ray spectrometry in the SEM and the detection of light elements including lithium," *Microsc. Anal.*, vol. 6, pp. S8–S13, 2013.
- [180] S. A. Speakman, "Basics of X-ray powder diffraction," *Mass.-USA 2011a Disponível Em Httpprism Mit EduxrayBasics 20of 20X-Ray 20Powder 20Diffraction Pdf*, 2011.
- [181] J. N. Reimers and J. R. Dahn, "Electrochemical and in situ X-ray diffraction studies of lithium intercalation in Li_xCoO₂," *J. Electrochem. Soc.*, vol. 139, no. 8, pp. 2091–2097, 1992.
- [182] H.-C. Shin and S.-I. Pyun, "Investigation of lithium transport through lithium cobalt dioxide thin film sputter-deposited by analysis of cyclic voltammogram," *Electrochimica Acta*, vol. 46, no. 16, pp. 2477–2485, 2001.
- [183] J. Xie, N. Imanishi, A. Hirano, M. Matsumura, Y. Takeda, and O. Yamamoto, "Kinetics investigation of a preferential (104) plane oriented LiCoO₂ thin film prepared by RF magnetron sputtering," *Solid State Ion.*, vol. 178, no. 19-20, pp. 1218–1224, 2007.

- [184] G. G. Amatucci, J. M. Tarascon, and L. C. Klein, "CoO₂, the end member of the Li x CoO₂ solid solution," *J. Electrochem. Soc.*, vol. 143, no. 3, pp. 1114–1123, 1996.
- [185] M. F. Lagadec, R. Zahn, and V. Wood, "Designing polyolefin separators to minimize the impact of local compressive stresses on lithium ion battery performance," *J. Electrochem. Soc.*, vol. 165, no. 9, pp. A1829–A1836, 2018.
- [186] S. Rodrigues, N. Munichandraiah, and A. K. Shukla, "Novel solution-combustion synthesis of LiCoO₂ and its characterization as cathode material for lithium-ion cells," *J. Power Sources*, vol. 102, no. 1-2, pp. 322–325, 2001.
- [187] P. Kalyani, N. Kalaiselvi, and N. Muniyandi, "A new solution combustion route to synthesize LiCoO₂ and LiMn₂O₄," *J. Power Sources*, vol. 111, no. 2, pp. 232–238, 2002.
- [188] W. Lai, C. K. Erdonmez, T. F. Marinis, C. K. Bjune, N. J. Dudney, F. Xu, R. Wartena, and Y.-M. Chiang, "Ultrahigh-Energy-Density Microbatteries Enabled by New Electrode Architecture and Micropackaging Design," *Adv. Mater.*, vol. 22, no. 20, pp. E139–E144, 2010.
- [189] M. Dubarry, B. Y. Liaw, M.-S. Chen, S.-S. Chyan, K.-C. Han, W.-T. Sie, and S.-H. Wu, "Identifying battery aging mechanisms in large format Li ion cells," *J. Power Sources*, vol. 196, no. 7, pp. 3420–3425, 2011.
- [190] L.-L. Lu, Y.-Y. Lu, Z.-J. Xiao, T.-W. Zhang, F. Zhou, T. Ma, Y. Ni, H.-B. Yao, S.-H. Yu, and Y. Cui, "Wood-Inspired High-Performance Ultrathick Bulk Battery Electrodes," *Adv. Mater.*, vol. 30, no. 20, p. 1706745, 2018.
- [191] I. Hwang, C. W. Lee, J. C. Kim, and S. Yoon, "Particle size effect of Ni-rich cathode materials on lithium ion battery performance," *Mater. Res. Bull.*, vol. 47, no. 1, pp. 73–78, 2012.
- [192] N. M. Trease, I. D. Seymour, M. D. Radin, H. Liu, H. Liu, S. Hy, N. Chernova, P. Parikh, A. Devaraj, and K. M. Wiaderek, "Identifying the Distribution of Al³⁺ in LiNi_{0.8}Co_{0.15}Al_{0.05}O₂," *Chem. Mater.*, vol. 28, no. 22, pp. 8170–8180, 2016.